8-2010

Isotropic and Anisotropic Metallic and Bimetallic Nanoparticles and Their Potential Applications in Biology

Minghong Liu
Western Michigan University

Recommended Citation

Liu, Minghong, "Isotropic and Anisotropic Metallic and Bimetallic Nanoparticles and Their Potential Applications in Biology" (2010). *Dissertations*. 606.
https://scholarworks.wmich.edu/dissertations/606

ISOTROPIC AND ANISOTROPIC METALLIC AND BIMETALLIC NANOPARTICLES AND THEIR POTENTIAL APPLICATIONS IN BIOLOGY

by

Minghong Liu

A Dissertation
Submitted to the
Faculty of The Graduate College
in partial fulfillment of the
requirements for the
Degree of Doctor of Philosophy
Department of Chemistry
Advisor: Sherine O. Obare, Ph.D.

Western Michigan University
Kalamazoo, Michigan
August 2010

ISOTROPIC AND ANISOTROPIC METALLIC AND BIMETALLIC NANOPARTICLES AND THEIR POTENTIAL APPLICATIONS IN BIOLOGY

Minghong Liu, Ph.D.

Western Michigan University, 2010

The development of synthetic procedures that produce nanoscale materials with controlled morphology is a significant area of investigation in nanotechnology. We have developed new synthetic procedures for fabrication of isotropic and/or anisotropic nanomaterials composed of palladium, ruthenium, nickel and alloys of palladium-ruthenium. The nanomaterials were fully characterized and were found to display unique size dependent properties. The electrochemical properties of isotropic palladium, ruthenium and palladium-ruthenium nanoparticles were investigated and the results showed that the particles were capable of charge storage and charge transfer on demand. Anisotropic palladium, ruthenium and palladium ruthenium nanoparticles were also fabricated and fully characterized. The nanoparticles display unique magnetic properties. We further investigated the surface modification of inherent magnetic nanoparticles. The particles were found to have a strong affinity toward biological cells but lacked toxicity toward the cells. The work is effective toward developing new methods for using nanoparticles for cell targeting.

ACKNOWLEDGMENTS

This dissertation would not have been possible without the supervision, encouragement and support from Dr. Sherine Obare. Her mentorship was leading me to a well experienced and independent chemist. She never let a chance slip away when it is time to encourage her students to proudly present herself or himself in conference or to win a fellowship.

I am heartily grateful to my parents and my sister, who give me moral support and self-giving cares. I also would like to thank Dr. Yirong Mo, who helped me in my earlier years in USA and advised me to follow my interest. In addition, I thank to Department of Chemistry in Western Michigan University, who offered great Ph.D. program.

Minghong Liu

TABLE OF CONTENTS

CHAPTER

Table of Contents—continued

CHAPTER

Table of Contents—continued

CHAPTER

Table of Contents—continued

CHAPTER

Table of Contents—continued

CHAPTER

LIST OF TABLES

LIST OF SCHEMES

LIST OF FIGURES

List of Figures—continued

List of Figures—continued

List of Figures—continued

List of Figures—continued

CHAPTER I

INTRODUCTION

1. Nanotechnology

Nanotechnology is a rapidly growing scientific and engineering field and is expected to impact various aspects of everyday living. The rapid growth can be attributed to the unique chemical and physical properties that arise when the dimensions of materials are reduced to the nanoscale. Significant efforts have been devoted toward developing synthetic strategies that produce nanoscale materials with uniformity in size and in shape. Such efforts lead to a better understanding of the unique size and shape dependant chemical and physical properties possessed by nanomaterials. As a result, the properties can be exploited for specific technological applications including sensor design, energy conversion, catalysis, medical diagnostics, electronics, and circuit miniaturization.

A significant amount of work in nanoscale science and technology has focused primarily on gold, silver and platinum nanoparticles, mainly due to their stability and relative ease of preparation. Other metals however, are much more difficult to prepare due to their lack of stability and difficulties in handling. However, there are several transition metals that have desirable properties on the nanoscale. Thus there is a major need for developing new and straightforward procedures to prepare these particles in high yield and with controlled morphology.

1.1 Optical properties

The collective oscillation of electrons in the conduction band[1] of metal nanoparticles gives right to unique optical properties. In the case of gold (Au), silver (Ag) and copper (Cu), these properties are manifested as surface Plasmon resonance and arises due to the absorption of quantized photons of energy (Figure 1.1). The absorption highly depends on the morphology and composition of the nanoparticles. For spherical nanoparticles the SPR absorbance results in single peak around 500 – 600 nm for Au, 380 – 450 nm for Ag, and 530 – 590 for Cu. The specific location depends on the particle size and the uniformity of the particles. Figure 1.2 shows the unusual optical properties of Au nanoparticles.

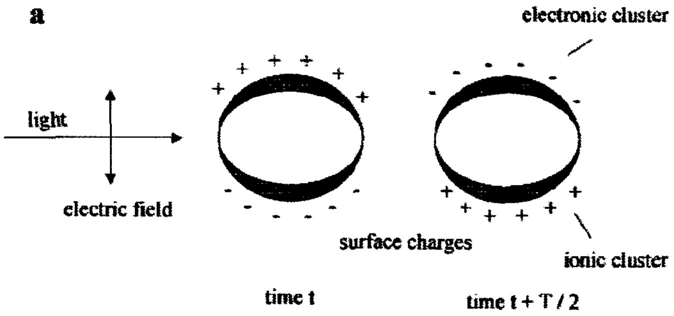

Figure 1.1 The light that strikes particles generates a electric field that could induce a polarization of conduction band electrons in the surface of nanoparticles. A net charge difference affects the electron distribution of neighboring particles. In this way a dipolar oscillation of the electrons is created with period *T*. This is known as surface plasmon absorption.[2]

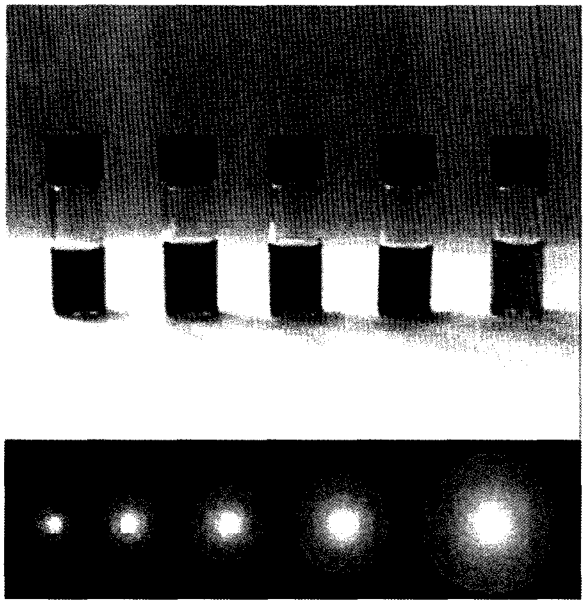

Figure 1.2 Gold colloidal contains different size of gold nanoparticles display different colors. (http://www.webexhibits.org/causesofcolor/9.html)

Additionally, controlling the shape and structure of nanoparticles results in modifications of the SPR absorbance peak. For example metallic nanorods of Au and Ag have been found to display two SPR peaks corresponding to a light being absorbed in the transverse direction and light being absorbed in the longitudinal direction, resulting in the transverse SPR and longitudinal SPR, respectively. The location/wavelength of the SPR peaks depend on the dimensions of the nanorods. (Figure 1.3).

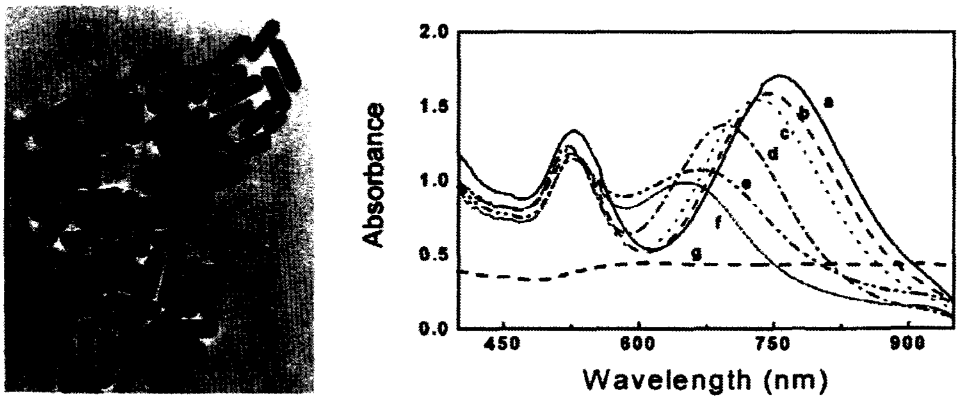

Figure 1.3 (a) TEM images of gold nanorods and (b) absorption spectra of nanorod with different aspect ratio[3]. The first peak corresponds to transverse surface plasmon absorption and second peak represents longitudinal surface plasmon absorption.

Anisotropic Pd nanoparticles appear to display well-defined absorbance peaks that have been described to be due to SPR. Xia[4] reported that the SPR peaks for triangular and hexagonal nanoplate Pd particles suspended in aqueous solution were located at 520 and 530 nm, respectively. He proposed that the peaks were due to the dielectric function of Pd and the thin thickness of the plates. Furthermore, Xia also showed that hollow Pd nanocubes displayed controllable increase in absorbance from blue (410 nm) to the near infrared (1200 nm) with decrease in particle size (Figure 1.4).

1.2 Charge transfer properties

Nanoscale materials are in demand for charge transfer applications for example in conversion of solar energy to chemical energy. Metallic nanoparticles have the potential to greatly improve charge transfer processes on the nanoscale. The major advantages include 1) a large surface to volume ratio could provide larger electrochemically active surfaces leading to larger areas for interaction with molecules, 2) effectively enhancing or accelerating electron transfer between an electrode and the electrolyte, 3) conjugation to redox-active molecule for overall improved performance, and 4) ability to generate transfer of multiple electrons. Nanoscale materials are therefore in high demand for charge transfer applications for example in conversion of solar energy to chemical energy. Grätzel[5] demonstrated that Pt nanoparticles were effective in the photoreduction of water to hydrogen in the presence of nanocrystalline titanium dioxide. Kamat[6] designed an organic dye-inorganic nanoparticle composite to improve the incident photocurrent efficiency of 54% in an effort to enhance solar cell performance.

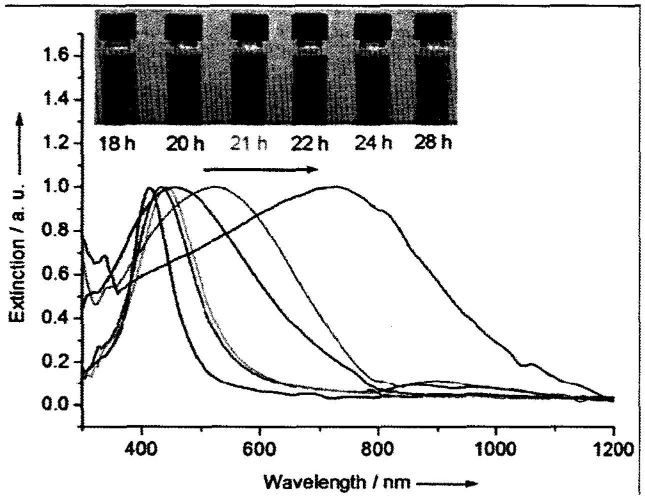

Figure 1.4 UV – Vis spectra of Pd Nanocubes. Longer corrosive etching time produced thinner wall of hollow Pd nanocubes which has 48 nm edge length. The surface plasmon resonance peaks red-shift with thinner wall.[4]

The processes involved in charge transfer on either the molecular scale or the bulk scale are fairly well understood[7, 8]. In bulk metals, the energy band is continuous and electrons travel freely inside the metal (Scheme 1.1). On the nanoscale, there arises a discontinuity of energy levels as a result of delocalization of electrons when the particle size approaches its mean free path. This split in energy bands gives discrete energy levels that facilitate quantized charge transfer. The current-voltage characteristic for an ideal quantized metal particle shows a Coulomb staircase as demonstrated in Figure 1.5. The required energy for single electron transfer fulfill the equation

$$\Delta V = e / C \tag{1}$$

where C is the capacitance of the particle.

2. Palladium and ruthenium nanoparticles

Palladium and ruthenium are well known metals with significant industrial importance. Both metals are crucial in catalyzing organic reactions, such as carbon-carbon coupling reactions (including Suzuki coupling, Stille reaction, Heck reaction)[9-11], hydrogenation[12], dehydrogenation[13, 14], etc. These metals are important in the synthesis of pharmaceutical and agricultural products[15, 16]. Palladium is widely used in catalytic converters to convert harmful gases such as carbon monoxide, hydrocarbons, and nitrogen oxide to less harmful substances. Pd has shown strong ability to absorb hydrogen, which gives Pd fundamental importance for modern industrial processes, such as in fuel cells, hydrogen sensors and for hydrogen storage[17-20].

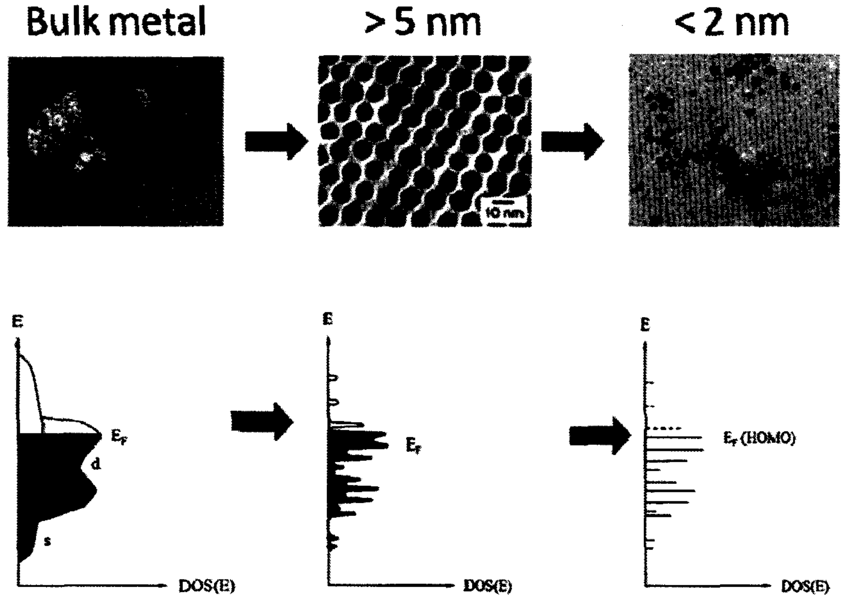

Scheme 1.1 Continuous electronic energy levels for bulk metal transitions to distinct energy levels for nanoparticles. Energy gap between the highest occupied and lowest unoccupied orbital opens up when the metal nanoparticle size was reduced to less than 2 nm. Reversely, when the metal atoms come close together, the discrete localized atomic orbitals delocalize, causing cohesion of the atoms, and the discrete atomic levels disperse in energy, giving rise to energy bands.

Ruthenium metal is typically used as a catalyst to improve the performance of materials toward wear and corrosion resistance[21]. Alloys of Ru have been effective in the electrocatalysis of direct methanol fuel cells[22-25]. Due to the importance of both palladium and ruthenium there is a large interest in establishing synthetic procedures for well-defined nanoparticles. The ability to obtain well-defined Pd and Ru nanoparticles provides the opportunity to understand their chemical and physical properties.

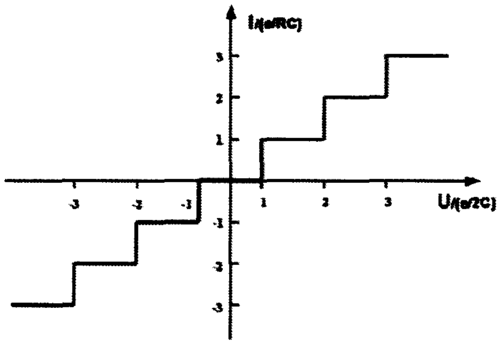

Figure 1.5 *I-U* plot of ideal single electron transfer[1]. The step function is the Coulomb blockade.

Bönnemann[7] showed that a metal salt, a stabilizer and a reducing agent were required to form metallic particles according to the equation:

$$MX_n(NR_4)_m + (n\text{-}m)\ \mathrm{Red} \rightarrow M_{NP} + (n\text{-}m)(\mathrm{Red}^+X^-) + m(NR_4{}^+X^-) \quad (2)$$

where M represents a metal (from group 8 - 10), X is Cl or Br, R is an alkyl group, Red is an effective reducing agent.

The reduction of the metal salt initiates the nucleation and growth processes of the nanoparticles[26]. By careful control of the choice of metal salt, reducing agent and stabilizer, this method has been manipulated to obtain palladium particles with nanoscale dimensions with controlled size and shape. The stabilizer prevents the particles from growing uncontrollably and maintaining uniformity. It can also serve as a template for shape-control of the nanoparticles[27-30]. In some cases the stabilizer can play the role of both reducing agent and stabilizer. Below, we discuss some of the most significant advances toward the synthesis of Pd nanoparticles using wet chemical preparation methods.

3. Synthesis of colloidal dispersions of monometallic and bimetallic nanoparticles

"Bottom up" and "top down" synthetic approaches are the two main strategies that have been pursued for nanomaterial fabrication. The "top down" involves taking a bulk material and reducing its size through physical processes to the nanoscale. The "bottom-up" approach involves using atoms and molecules as precursors and organizing them through chemical processes into nanostructures. A wide variety of synthetic strategies, including chemical reduction, photolysis, electronic plating, pyrolysis, vapor deposition, etc., have been used to fabricate isotropic and anisotropic metallic nanoparticles.

3.1 Nanoparticle growth

Chemical synthesis processes of nanoparticles allow control of particle size and particle uniformity. The process consists of four main steps: nucleation, growth, Ostwald ripening, stabilization. A good understanding of the mechanism is important for improving the quality (such as size, shape) of nanoparticles.

Nucleation. The formation of nanoparticles starts from nucleation, in which the solid phase precipitates from solution by chemical reduction, thermal decomposition, or other means to form nuclei. These nuclei attract other precipitates and the nucleation process stops when the size of nuclei reaches a critical size. Because the overall free energy is associated with not only the surface area but also the volume, before the critical size is reached, bigger nuclei will further increase their free energy (Figure1.6). This process determines the amount of nuclei.

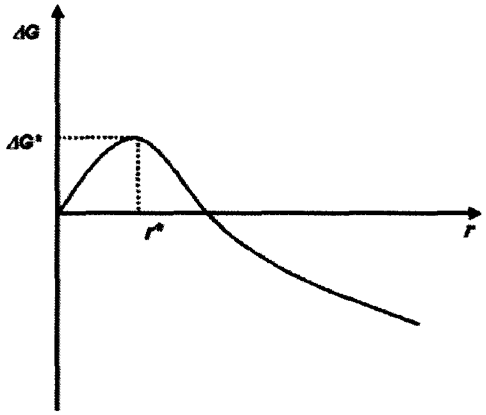

Figure 1.6 Plot of the overall free energy as a function of particle size[1].

Particle growth. After nuclei are formed in solution, they grow to larger particles by addition of more precipitates to the surface. Particle uniformity is typically controlled during this step.

Ostwald ripening. When the precursors are depleted, the bigger particles continue to grow by obtaining molecules or atoms from smaller particles, in order to reduce the overall surface energy. Uniformity of the particle size can be controlled during the particle growth stage. Once the reaction goes into Ostwald ripening, it is hard to get monodisperse particles.

Stabilization and passivation. In addition to the growth process that takes place by nuclei obtaining precipitates from solution, the nanoparticles tend to aggregate with other particles, because they are not thermodynamically stable. To prevent the aggregation and terminate further growth to get stable nanoparticles, surface protecting reagents must be used[31], or the particles could be placed in an inorganic matrix or polymer to prevent the collision between particles[26].

Surface protecting reagents normally have functional groups that bind to the particles with high affinity. The interaction of the ligand and solvent are so strong that they allow the particles to remain suspended as colloids. For example, thiols having long carbon train and bulky trioctylphosphine (TOPO) provide steric hindrance for access of other materials[32].

After the nanoparticles reach the desired size, growth is discontinued. The resulting particles should be stable for a long time to allow characterization and their use in various applications. In some case it may be necessary to precipitate out the nanoparticles for further characterization or chemical reactions using other solvents or by centrifugation.

Surface ligand replacement. Ligands or stabilizers at the nanoparticle surface strongly influence the solubility, electronic conductivity, melting point, stability and reactivity of the particles. In this regard it is often necessary to exchange the surface ligand. Ligand exchange can be achieved by exposing the nanoparticles to excess competing ligands.

3.2 Chemical synthesis methods for monometallic and bimetallic nanostructures

A variety of methods has been employed for making Ru and Pd nanoparticles, including chemical reduction or decomposition, pyrolysis, chemical vapor deposition, physical vapor deposition, electrochemical deposition, etc.

Chemical reduction. Metal nanoparticle synthesis by chemical reduction is a process in which a metal precursor (usually the metal salt or the metal complex) in solution is reduced to the zero-valent state by a chemical reducing agent. Typical reducing agents for metal nanoparticle synthesis have included alcohols[33-38], molecular hydrogen (H_2)[39-46], sodium citrate[47, 48], hydrazine (N_2H_4)[49-53], and sodium borohydride ($NaBH_4$)[33, 54-66]. The selection of the reducing agent is important toward obtaining the desired particles. Strong reducing agents could highly influence the nucleation rate, as well as the growth rate of nanoparticles, making size control a difficult task[67]. Figure 1.7 shows the schematic chemical reduction procedure for synthesis of Au nanoparticles. The Au precursor, $HAuCl_4$ was reduced by $NaBH_4$ and alkylthiols were used as stabilizers. The common stabilizer used to cap the colloidal metallic nanoparticles include thiols[68-72], polymers[33, 34, 36, 37, 39-42, 73], dendrimers[57, 74-80], surfactants[81-85].

The temperature, reaction time, reactant concentration, the ratio of precursor to the stabilizers all conttribute to the size of the nanoparticles. In general, the nanoparticle size increases with increasing reaction time as more molecules or atoms are added to nanoparticles surface. Higher temperatures increase the reaction rate of solute in the solvent, producing more materials for nanoparticles, in turn, increasing the rate of materials being added to the nanoparticle surface. Tailoring the ratio of the concentration of precursors and that of the stabilizers provides control of the particle size.

Synthesis of bimetallic nanoparticles. An effective method for preparing bimetallic nanoparticle is by chemical reduction. Three major procedures have been reported: (a) coreduction, where corresponding metal ions in solution are simultaneously reduced by strong reducing agents in the presence of stabilizing ligands; (b) successive reduction, where the structures of the alloys can be controlled especially for core-shell structures, attributed to the difference in the reduction potential of the two metals; and (c) thermal decomposition, where both metals are part of a coordination complex and at high temperature the chelating ligands undergo decomposition. Nanoparticles fabricated by above methods may exist in various structures, such as core-shell structure, alloy structure, and cluster-in-cluster structure, as illustrated in Figure 1.8.

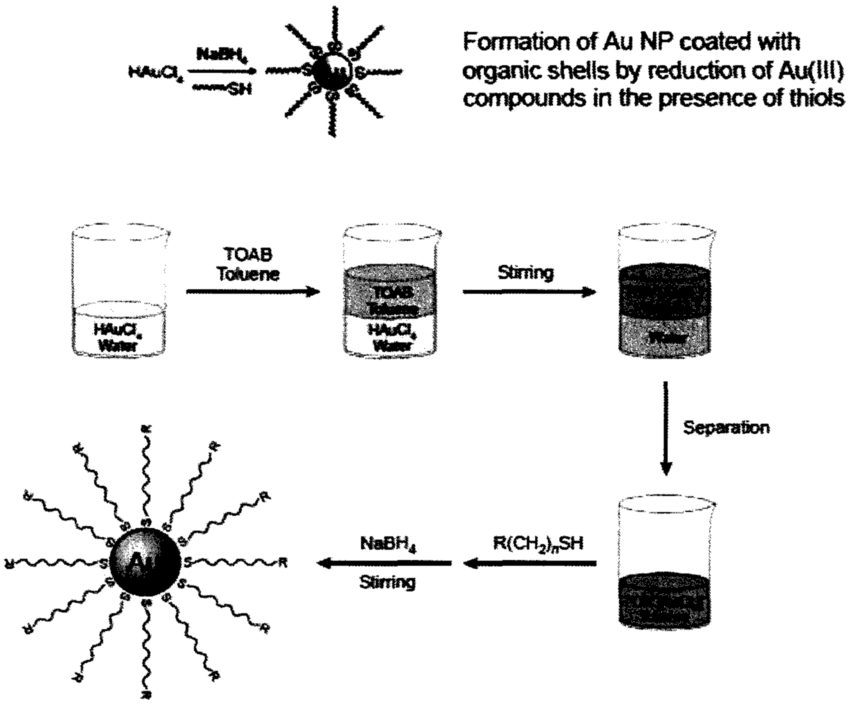

Figure 1.7 Chemical reduction synthesis method for producing Au nanoparticles. Phase transfer agent tetraoctylammonium bromide (TOAB) was used to transfer gold salt to organic layer and mixed with stabilizing ligand alkylthiol before gold salt was reduced by sodium borohydride.[86, 87]

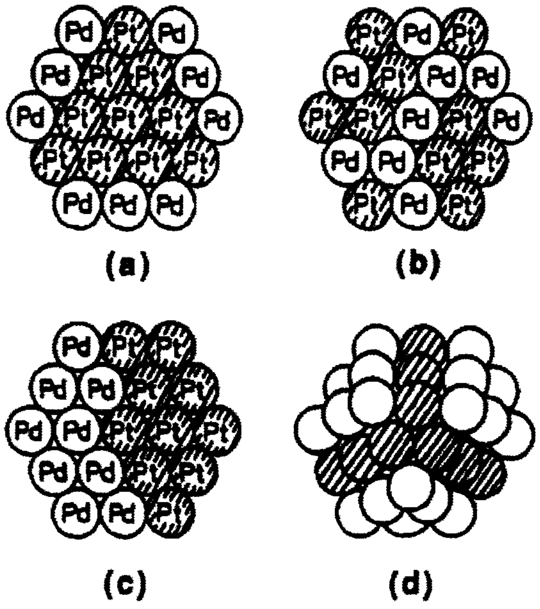

Figure 1.8 Schematic representation of three bimetallic cluster structure models in the case of Pd-Pt nanoparticles. (a, d) Pt core-Pd shell model, (b) random model, (c) separated model. (d) is the three-dimensional picture of the core-shell model[88].

3.3 Characterization techniques

Elaborate synthetic approaches have been developed that enable significant control over the size and shape of nanostructures. In order to understand the properties of the materials formed based on the preparation method, several characterization techniques have been used in this dissertation. These include electron microscopy, electron diffraction, photoelectron spectroscopy, X-ray diffraction, ultraviolet-visible (UV-Vis) spectroscopy and electrochemistry.

Electron microscopy is a powerful technique for the characterization of metallic nanostructures, and is capable of providing information of morphology, topography and composition of the material under investigation. The electron microscopy we used includes transmission electron microscopy (for Pd, Ru and Pd-Ru alloy nanoparticles) and scanning electron microscopy (for Ni, Pd, Ru and Pd-Ru alloy nanowires).

Transmission electron microscope (TEM) and High Resolution TEM (HRTEM). In TEM, a tungsten filament emits an electron beam (at a voltage of 100 keV) as its source of radiation. The electron beam is transmitted through the sample and the output transmittance provides the image. TEM allow the direct visualization of particles and so has been very important tool for determining particle formation, shape and size distribution.

Advancements in electron microscopy have led to the development of high-resolution transmission electron microscopy (HRTEM), which allows the analysis of nanoparticles with resolution up to 0.8Å. This is made possible by using a high-voltage (200 ~ 300 keV) power supply for the electron beam. HRTEM also allows structural features which are only a few angstroms in size to be imaged, so that the crystal structure can also be investigated.

Scanning Electron Microscopy (SEM). The operating principles of SEM are very similar to that of TEM, such as a high-voltage (a few hundred eV to 100 keV) electron beam is used to excite the sample. The electron beam is scanned across the sample in a rastering fashion. The process creates low-energy secondary electrons which emit from the surface to form an image. The main difference between the images produced by TEM and SEM is that TEM provides a two-dimensional image, while SEM gives a three-dimensional representation of the object being observed. The resolution of SEM is also about an order of magnitude poorer than that of TEM.

Powder X-ray Diffraction (XRD). XRD is efficient in providing information regarding the crystallographic structure of a sample. The technique uses X-ray radiation that passes through a sample, such that the scattered beams form a diffraction pattern based on the sample. The XRD spectra could determine the orientation and crystallinity of crystal or grain (namely, the crystal structure), purity of the sample, the atomic arrangement and spacing between layers or rows of atoms. The particle size (d) can be calculated from the width of the characteristic peaks by using the Scherrer formula:

$$d = 0.9\lambda / (\beta \times \cos\theta) \tag{3}$$

where λ is the wavelength of the X-rays, β is the full width at half maximum of diffraction peak, and θ is the angle corresponding to the peak[89].

Selective Area Electron Diffraction (SAED). SAED is a diffraction technique that is usually coupled with HRTEM to identify crystal structures and examine crystal defects. The technique is similar to XRD, but unique in that areas as small as several hundred square nanometers in size can be examined. Today, SAED is recognized as being a routine and important method for characterizing metallic nanostructures.

X-ray Photoelectron Spectroscopy (XPS). XPS is a quantitative spectroscopic technique that measures the elemental composition, empirical formula, chemical state and electronic state of the elements that exist within a material. It does surface chemical analysis based on the photoelectric effect, which describe the phenomenon of the ejection of electrons when photons with sufficient energy impinge upon a surface. XPS spectra are obtained by irradiating a material with a beam of aluminum or magnesium X-rays while simultaneously measuring the kinetic energy and number of electrons that escape from the top 1 to 10 nm of the material being analyzed. Due to the characteristic binding energy and electronic structure of each element, the peaks in the resultant spectrum provide information on the chemical state and composition of the surface atoms. XPS requires ultra-high vacuum conditions.

Energy-Dispersive X-Ray (EDX) Analysis. Similar to XPS, EDX is a technique that allows the chemical composition of a material to be determined. Here, X-ray beams are used to excite a surface, while the emission spectrum provides information on the elemental composition within the sample being analyzed, as each element provides a characteristic emission upon excitation. EDX has been coupled with electron microscopy to provide a powerful analytical tool for the chemical characterization of nanomaterials. In addition, EDX can provide quantitative data on the composition of each element contained in a sample.

Electrochemistry. Electrochemical techniques have been useful when characterizing metallic nanoparticles, where information on both the metallic component and the stabilizing ligand can be obtained. Cyclic voltammetry (CV) has been used to study the behavior of ligands at the surface. The quantum confinement in metallic nanoparticles has been found to influence the electron-transfer abilities of ligand at the surface. A similar technique, differential pulse voltammetry (DPV) has also been used as a characterization technique for metallic nanoparticles. The difference between CV and DPV is that, in CV, the current is measured as a function of increasing or decreasing applied potential, whereas in DPV the current at the working electrode is recorded while the pulse potential between the working and reference electrodes is swept linearly in time. The pulse potential provides higher resolution on the current collected.

Scanning Tunneling Microscopy and Spectroscopy (STM/STS). STM/STS allows the electronic measurement of individual nanostructures by probing the local density of electronic states and the band gap of particles at the atomic scale. The experiment uses a STM tip fixed on top of the selected nanoparticle, but the feedback loop is turned off. In this case, the current-voltage (*I-V*) curves provide information on the single-electron tunneling (SET) process that occurs in a double barrier tunneling junction. Single-electron transfer phenomena due to quantum confinement effect on metallic nanoparticles can be observed as coulomb staircases and coulomb blockade where the current is zero before the voltage become sufficient to overcome the band gap (Figure 1.5)[90].

Infrared (IR) spectroscopy. IR is important in investigating the surface ligand binding to nanostructures, since the ligands are mostly organic molecules. It provides information of the degree of order and relative orientation of surface-bound ligands[69, [91-94], and also plays an important role in confirming the completion of a ligand exchange reaction[90]. The chemical shifts before and after the binding help determining the binding functional group and the binding pattern[95].

UV-Visible absorbance spectroscopy. Most precursors exhibit color in solution and change color when they are decomposed or reduced. UV-Vis spectroscopy has been used to monitor this transition to confirm the completion of reduction[96]. Noble metal nanoparticles, especially Au and Ag nanoparticles, have well-defined absorbance peaks in UV-vis spectroscopy due to surface plasmon resonance. The measurements are used to provide information on the size and quality of nanoparticles, because the shape and absorbance of the peaks are related to the uniformity, shape and size of nanoparticles[4, 97].

Nuclear magnetic Resonance (NMR) spectroscopy. NMR has been used primarily to characterize the nature of binding of ligands at the particles surface. Most common ligands, such as thiol, phosphine, sulfide, phenol, and carbine can be investigated by ^{1}H, ^{13}C and ^{31}P NMR to confirm the binding affinity[98].

4. Applications of metallic nanoparticles

Metallic nanostructures possess unique, beneficial chemical, physical and mechanical properties that can be exploited for a variety of applications. These applications include, but are not limited to, catalysis, computer chips, energy conversion, high energy density batteries, environmental remediation, data storage, sensing, imaging, medical diagnosis, and medical treatment. It is evident that nanomaterials outperform their conventional counterpart and new applications based on their superior properties have been investigated. Below is a brief description on the applications of palladium and ruthenium nanoparticles.

4.1 Catalysis

The high surface to volume ratio offered by nanoscale particles makes them excellent candidates for catalytic reactions. The catalytic efficiency has been found to depend on the particle size as well as the shape[39, 40]. It was found that activation energy, preexponential factor (A) and entropy of activation of the same reaction changed when the size of nanoparticles was varied[40]. The edges and corners of anisotropic nanostructures show high catalytic activities relative to other surfaces and thus may favor the reaction rate.

Homogeneous catalysis. Colloidal metallic nanoparticles are often used as homogeneous catalysts. The stabilizer on the particle surface is typically used to prevent particle aggregation, however, these ligands can sometimes block active sites on the catalyst surface[33]. Metallic nanoparticles colloid have been tested in many types of chemical reactions, such as Suzuki cross-coupling reaction[33, 35-37, 55, 57, 99, 100], Heck cross-coupling reaction[99, 101-108], hydrogenation[62, 109-118], electron-transfer reactions[40-43, 55, 119-122]. For cross coupling reactions (C-C bond formation reactions), palladium nanoparticles are most often used.

Heterogeneous catalysis. The recovery of homogeneous catalysts is often tedious and thus methods for immobilizing colloidal nanoparticles onto solid supports are desirable[96]. The immobilization decreases the possibility of aggregation and increase the quality and number of catalytic cycles. Figure 1.9, shows that smaller nanoparticle sizes favor the reusability of catalyst, and immobilized nanoparticles maintain high conversation efficiency for many cycles.

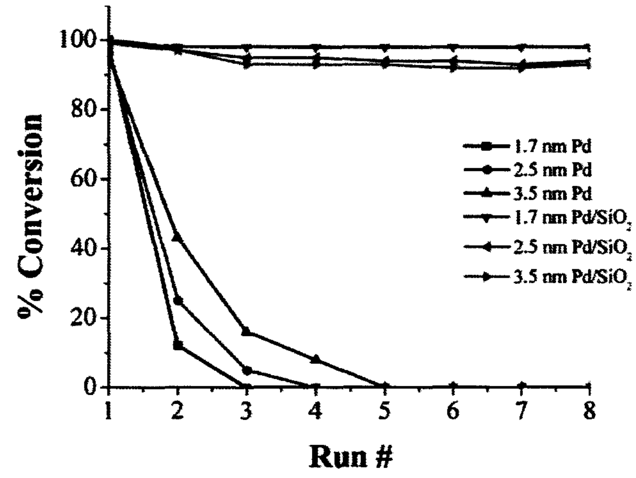

Figure 1.9 Plot of percent conversion as function of number of catalytic cycles for the hydrogenation reaction of styrene to 1- ethylbenzene. Three sizes of Pd nanoparticles were used as homogeneous catalyst and heterogeneous catalyst (immobilized in SiO_2).

Bimetallic alloy nanoparticle catalysts. Metal alloys that consist of two or more metals are of great fundamental and practical interest. They often exhibit superior properties relative to those of their single metal counterparts. For example, Ti-Ni is used as a shape-memory material whereas Ni alone or Ti alone does not possess such properties. In catalysis, alloys could greatly enhance chemical transformations relative to their individual metal counterparts. Alloys are typically used in the automotive industry as catalytic converters. For example, Pt-Rh alloys are used as catalytic converters whereby Pt serves to oxidize hydrocarbons and carbon monoxide, while Rh serves to catalyze the reduction of NO_x (Carbonitride)[123]. The bimetallic alloy made from Pd and Ru was believed to possess enhanced catalytic properties including selectivity and specificity. Promising results have been demonstrated in the manufacture of pharmaceuticals and agricultural herbicides, degradation of harmful environmental pollutants, and as sensors for detection of various analytes[124-127].

4.2 Biological applications

Nanoscale materials have found various biological applications. The unique optical properties possessed by metallic gold and silver nanoparticles and quantum dots have led to their use in biosensing, and in clinical diagnostics[128-131]. Other applications have included microbial fuel cells[132] and MRI (magnetic resonance imaging)[133, 134].

Nanobiotechnology aims to overcome the limitation of conventional medical methods by taking advantage of the properties and the dimensions of nanomaterials. There has been a surge in interest for using nanomaterials for cancer detection and cancer treatment. It is expected that nanomaterials can be effectively designed to allow specific cell targeting and thus avoid all the common side effects that accompany traditional treatment methods.

5. Summary

The unique properties that arise when materials are made to the nanoscale have opened up a myriad of opportunities of fundamental and technological importance. However, the field of nanotechnology remains currently limited by the lack of straightforward synthetic procedures to provide desired nanoscale materials in high yield and with controlled morphology. Having access to such materials will allow a thorough investigation and understanding of material properties on the nanoscale. An improved understanding of the chemical and physical properties of nanoscale materials will allow the use of the materials in advanced scientific and technological applications. This dissertation focuses on the synthesis, and characterization of size and shape-controlled Pd, Ru and Pd-Ru alloy nanoparticles and nanowires, as well as an investigation of the applications of functionalized magnetic nickel nanowires. The results will provide insight to understanding the well-defined metallic nanostructures.

6. References

1. Burda, C.; Chen, X. B.; Narayanan, R.; El-Sayed, M. A., Chemistry and properties of nanocrystals of different shapes. *Chemical Reviews* **2005,** 105, (4), 1025-1102.

2. Link, S.; El-Sayed, M. A., Shape and size dependence of radiative, non-radiative and photothermal properties of gold nanocrystals. *International Reviews in Physical Chemistry* **2000,** 19, (3), 409-453.

3. Mohamed, M. B.; Ismail, K. Z.; Link, S.; El-Sayed, M. A., Thermal reshaping of gold nanorods in micelles. *Journal of Physical Chemistry B* **1998,** 102, (47), 9370-9374.

4. Xiong, Y. J.; Wiley, B.; Chen, J. Y.; Li, Z. Y.; Yin, Y. D.; Xia, Y. N., Corrosion-based synthesis of single-crystal Pd nanoboxes and nanocages and their surface plasmon properties. *Angewandte Chemie-International Edition* **2005,** 44, (48), 7913-7917.

5. Kiwi, J.; Gratzel, M., Protection, size factors, and reaction dynamics of colloidal redox catalysts mediating light-induced hydrogen evolution from water. *Journal of the American Chemical Society* **1979,** 101, (24), 7214-7217.

6. Hasobe, T.; Imahori, H.; Kamat, P. V.; Ahn, T. K.; Kim, S. K.; Kim, D.; Fujimoto, A.; Hirakawa, T.; Fukuzumi, S., Photovoltaic cells using composite nanoclusters of porphyrins and fullerenes with gold nanoparticles. *Journal of the American Chemical Society* **2005,** 127, (4), 1216-1228.

7. Barbara, P. F.; Meyer, T. J.; Ratner, M. A., Contemporary issues in electron transfer research. *Journal of Physical Chemistry* **1996,** 100, (31), 13148-13168.

8. Bixon, M.; Jortner, J., Electron transfer - From isolated molecules to biomolecules. In *Electron Transfer-from Isolated Molecules to Biomolecules, Pt 1*, John Wiley & Sons Inc: New York, 1999; Vol. 106, pp 35-202.

9. Bellina, F.; Carpita, A.; Rossi, R., Palladium catalysts for the Suzuki cross-coupling reaction: An overview of recent advances. *Synthesis-Stuttgart* **2004,** (15), 2419-2440.

10. Farina, V., High-turnover palladium catalysts in cross-coupling and Heck chemistry: A critical overview. *Advanced Synthesis & Catalysis* **2004,** 346, (13-15), 1553-1582.

11. Herrmann, W. A.; Bohm, V. P. W.; Reisinger, C. P., Application of palladacycles in Heck type reactions. *Journal of Organometallic Chemistry* **1999,** 576, (1-2), 23-41.

12. Stanislaus, A.; Cooper, B. H., Aromatic hydrogenation catalysis - a review. *Catalysis Reviews-Science and Engineering* **1994,** 36, (1), 75-123.

13. Besson, M.; Gallezot, P., Selective oxidation of alcohols and aldehydes on metal catalysts. *Catalysis Today* **2000,** 57, (1-2), 127-141.

14. Dittmeyer, R.; Hollein, V.; Daub, K., Membrane reactors for hydrogenation and dehydrogenation processes based on supported palladium. *Journal of Molecular Catalysis A-Chemical* **2001,** 173, (1-2), 135-184.

15. Tsuji, J., *Palladium Reagents and Catalysts*. John Wiley & Sons, Ltd: Chichester, 1995.

16. Malleron, J. L.; Fiaud, J. C.; Legros, J. Y., *Handbook of Palldaium-Catalyzed Organic Reactions*. Academic Press: London, 2000.

17. Sykes, E. C. H.; Fernandez-Torres, L. C.; Nanayakkara, S. U.; Mantooth, B. A.; Nevin, R. M.; Weiss, P. S., Observation and manipulation of subsurface hydride in Pd{111} and its effect on surface chemical, physical, and electronic properties. *Proceedings of the National Academy of Sciences of the United States of America* **2005,** 102, (50), 17907-17911.

18. Cheng, F. L.; Dai, X. C.; Wang, H.; Jiang, S. P.; Zhang, M.; Xu, C. W., Synergistic effect of Pd-Au bimetallic surfaces in Au-covered Pd nanowires studied for ethanol oxidation. *Electrochimica Acta* **2010,** 55, (7), 2295-2298.

19. Xu, M. L.; Zhang, Z. F.; Yang, X. W., Electrocatalytic Oxidation of Methanol on Pd Nanowire Electrode in Alkaline Media. *Rare Metal Materials and Engineering* **2010,** 39, (1), 129-133.

20. Favier, F.; Walter, E. C.; Zach, M. P.; Benter, T.; Penner, R. M., Hydrogen sensors and switches from electrodeposited palladium mesowire arrays. *Science* **2001,** 293, (5538), 2227-2231.

21. Rao, C. R. K.; Trivedi, D. C., Chemical and electrochemical depositions of platinum group metals and their applications. *Coordination Chemistry Reviews* **2005,** 249, (5-6), 613-631.

22. Dinh, H. N.; Ren, X. M.; Garzon, F. H.; Zelenay, P.; Gottesfeld, S., Electrocatalysis in direct methanol fuel cells: in-situ probing of PtRu anode catalyst surfaces. *Journal of Electroanalytical Chemistry* **2000,** 491, (1-2), 222-233.

23. Nashner, M. S.; Frenkel, A. I.; Somerville, D.; Hills, C. W.; Shapley, J. R.; Nuzzo, R. G., Core shell inversion during nucleation and growth of bimetallic Pt/Ru nanoparticles. *Journal of the American Chemical Society* **1998,** 120, (32), 8093-8101.

24. Choi, J. H.; Park, K. W.; Kwon, B. K.; Sung, Y. E., Methanol oxidation on Pt/Ru, Pt/Ni, and Pt/Ru/Ni anode electrocatalysts at different temperatures for DMFCs. *Journal of the Electrochemical Society* **2003,** 150, (7), A973-A978.

25. Lee, S. A.; Park, K. W.; Choi, J. H.; Kwon, B. K.; Sung, Y. E., Nanoparticle synthesis and electrocatalytic activity of Pt alloys for direct methanol fuel cells. *Journal of the Electrochemical Society* **2002,** 149, (10), A1299-A1304.

26. Jiang, Y., *Forced Hydrolysis and Chemical Co-Precipitation*. Kluwer Academic: New York, 2003; p 59.

27. Gole, A.; Murphy, C. J., Seed-mediated synthesis of gold nanorods: Role of the size and nature of the seed. *Chemistry of Materials* **2004,** 16, (19), 3633-3640.

28. Hu, J. T.; Odom, T. W.; Lieber, C. M., Chemistry and physics in one dimension: Synthesis and properties of nanowires and nanotubes. *Accounts of Chemical Research* **1999,** 32, (5), 435-445.

29. Ren, Z. F.; Huang, Z. P.; Wang, D. Z.; Wen, J. G.; Xu, J. W.; Wang, J. H.; Calvet, L. E.; Chen, J.; Klemic, J. F.; Reed, M. A., Growth of a single freestanding multiwall carbon nanotube on each nanonickel dot. *Applied Physics Letters* **1999,** 75, (8), 1086-1088.

30. Huang, Z. P.; Wu, J. W.; Ren, Z. F.; Wang, J. H.; Siegal, M. P.; Provencio, P. N., Growth of highly oriented carbon nanotubes by plasma-enhanced hot filament chemical vapor deposition. *Applied Physics Letters* **1998,** 73, (26), 3845-3847.

31. Murray, C. B.; Kagan, C. R.; Bawendi, M. G., Synthesis and characterization of monodisperse nanocrystals and close-packed nanocrystal assemblies. *Annual Review of Materials Science* **2000,** 30, 545-610.

32. Peng, Z. A.; Peng, X. G., Formation of high-quality CdTe, CdSe, and CdS nanocrystals using CdO as precursor. *Journal of the American Chemical Society* **2001,** 123, (1), 183-184.

33. Li, Y.; El-Sayed, M. A., The effect of stabilizers on the catalytic activity and stability of Pd colloidal nanoparticles in the Suzuki reactions in aqueous solution. *Journal of Physical Chemistry B* **2001,** 105, (37), 8938-8943.

34. Teranishi, T.; Miyake, M., Size control of palladium nanoparticles and their crystal structures. *Chemistry of Materials* **1998,** 10, (2), 594-600.

35. Li, Y.; Boone, E.; El-Sayed, M. A., Size effects of PVP-Pd nanoparticles on the catalytic Suzuki reactions in aqueous solution. *Langmuir* **2002,** 18, (12), 4921-4925.

36. Li, Y.; Hong, X. M.; Collard, D. M.; El-Sayed, M. A., Suzuki cross-coupling reactions catalyzed by palladium nanoparticles in aqueous solution. *Organic Letters* **2000,** 2, (15), 2385-2388.

37. Narayanan, R.; El-Sayed, M. A., Effect of catalysis on the stability of metallic nanoparticles: Suzuki reaction catalyzed by PVP-palladium nanoparticles. *Journal of the American Chemical Society* **2003,** 125, (27), 8340-8347.

38. Teranishi, T.; Hosoe, M.; Miyake, M., Formation of monodispersed ultrafine platinum particles and their electrophoretic deposition on electrodes. *Advanced Materials* **1997,** 9, (1), 65-&.

39. Ahmadi, T. S.; Wang, Z. L.; Green, T. C.; Henglein, A.; ElSayed, M. A., Shape-controlled synthesis of colloidal platinum nanoparticles. *Science* **1996,** 272, (5270), 1924-1926.

40. Narayanan, R.; El-Sayed, M. A., Shape-dependent catalytic activity of platinum nanoparticles in colloidal solution. *Nano Letters* **2004,** 4, (7), 1343-1348.

41. Narayanan, R.; El-Sayed, M. A., Effect of nanocatalysis in colloidal solution on the tetrahedral and cubic nanoparticle SHAPE: Electron-transfer reaction catalyzed by platinum nanoparticles. *Journal of Physical Chemistry B* **2004,** 108, (18), 5726-5733.

42. Narayanan, R.; El-Sayed, M. A., Changing catalytic activity during colloidal platinum nanocatalysis due to shape changes: Electron-transfer reaction. *Journal of the American Chemical Society* **2004,** 126, (23), 7194-7195.

43. Li, Y.; Petroski, J.; El-Sayed, M. A., Activation energy of the reaction between hexacyanoferrate(III) and thiosulfate ions catalyzed by platinum nanoparticles. *Journal of Physical Chemistry B* **2000,** 104, (47), 10956-10959.

44. Fu, X. Y.; Wang, Y. A.; Wu, N. Z.; Gui, L. L.; Tang, Y. Q., Shape-selective preparation and properties of oxalate-stabilized Pt colloid. *Langmuir* **2002,** 18, (12), 4619-4624.

45. Ohde, H.; Wai, C. M.; Kim, H.; Kim, J.; Ohde, M., Hydrogenation of olefins in supercritical CO_2 catalyzed by palladium nanoparticles in a water-in-CO_2 microemulsion. *Journal of the American Chemical Society* **2002,** 124, (17), 4540-4541.

46. Aiken, J. D.; Finke, R. G., Polyoxoanion- and tetrabutylammonium-stabilized, near-monodisperse, 40 +/- 6 angstrom Rh(0)similar to(1500) to Rh(0)similar to(3700) nanoclusters: Synthesis, characterization, and hydrogenation catalysis. *Chemistry of Materials* **1999,** 11, (4), 1035-1047.

47. Harriman, A.; Thomas, J. M.; Millward, G. R., Catalytic and structural - properties of iridium-iridium dioxide colloids. *New Journal of Chemistry* **1987,** 11, (11-12), 757-762.

48. Furlong, D. N.; Launikonis, A.; Sasse, W. H. F.; Sanders, J. V., Colloidal platinum sols - preparation, characterization and stability towards salt. *Journal of the Chemical Society-Faraday Transactions I* **1984,** 80, 571-&.

49. Wu, S. H.; Chen, D. H., Synthesis and stabilization of Ni nanoparticles in a pure aqueous CTAB solution. *Chemistry Letters* **2004,** 33, (4), 406-407.

50. Demir, M. M.; Gulgun, M. A.; Menceloglu, Y. Z.; Erman, B.; Abramchuk, S. S.; Makhaeva, E. E.; Khokhlov, A. R.; Matveeva, V. G.; Sulman, M. G., Palladium nanoparticles by electrospinning from poly(acrylonitrile-co-acrylic acid)-$PdCl_2$ solutions. Relations between preparation conditions, particle size, and catalytic activity. *Macromolecules* **2004,** 37, (5), 1787-1792.

51. Solla-Gullon, J.; Rodes, A.; Montiel, V.; Aldaz, A.; Clavilier, J., Electrochemical characterisation of platinum-palladium nanoparticles prepared in a water-in-oil microemulsion. *Journal of Electroanalytical Chemistry* **2003,** 554, 273-284.

52. Solla-Gullon, J.; Montiel, V.; Aldaz, A.; Clavilier, J., Synthesis and electrochemical decontamination of platinum-palladium nanoparticles prepared by water-in-oil microemulsion. *Journal of the Electrochemical Society* **2003,** 150, (2), E104-E109.

53. Zhang, X.; Chan, K. Y., Water-in-oil microemulsion synthesis of platinum-ruthenium nanoparticles, their characterization and electrocatalytic properties. *Chemistry of Materials* **2003,** 15, (2), 451-459.

54. Creighton, J. A.; Blatchford, C. G.; Albrecht, M. G., Plasma resonance enhancement of raman-scattering by pyridine adsorbed on silver or gold sol particles of size comparable to the excitation wavelength. *Journal of the Chemical Society-Faraday Transactions Ii* **1979,** 75, 790-798.

55. Narayanan, R.; El-Sayed, M. A., Effect of colloidal catalysis on the nanoparticle size distribution: Dendrimer-Pd vs PVP-Pd nanoparticles catalyzing the Suzuki coupling reaction. *Journal of Physical Chemistry B* **2004,** 108, (25), 8572-8580.

56. Tamura, M.; Fujihara, H., Chiral bisphosphine BINAP-stabilized gold and palladium nanoparticles with small size and their palladium nanoparticle-catalyzed asymmetric reaction. *Journal of the American Chemical Society* **2003,** 125, (51), 15742-15743.

57. Pittelkow, M.; Moth-Poulsen, K.; Boas, U.; Christensen, J. B., Poly(amidoamine)-dendrimer-stabilized Pd(0) nanoparticles as a catalyst for the Suzuki reaction. *Langmuir* **2003,** 19, (18), 7682-7684.

58. Tabuani, D.; Monticelli, O.; Chincarini, A.; Bianchini, C.; Vizza, F.; Moneti, S.; Russo, S., Palladium nanoparticles supported on hyperbranched aramids: Synthesis, characterization, and some applications in the hydrogenation of unsaturated substrates. *Macromolecules* **2003,** 36, (12), 4294-4301.

59. Mayer, A. B. R.; Mark, J. E.; Morris, R. E., Palladium and platinum nanocatalysts protected by amphiphilic block copolymers. *Polymer Journal* **1998,** 30, (3), 197-205.

60. Mayer, A. B. R.; Mark, J. E., Colloidal gold nanoparticles protected by cationic polyelectrolytes. *Journal of Macromolecular Science-Pure and Applied Chemistry* **1997,** A34, (11), 2151-2164.

61. Mayer, A. B. R.; Johnson, R. W.; Hausner, S. H.; Mark, J. E., Colloidal silver nanoparticles protected by water-soluble nonionic polymers and "soft"

polyacids. *Journal of Macromolecular Science-Pure and Applied Chemistry* **1999,** A36, (10), 1427-1441.

62. Zhao, M. Q.; Crooks, R. M., Homogeneous hydrogenation catalysis with monodisperse, dendrimer-encapsulated Pd and Pt nanoparticles. *Angewandte Chemie-International Edition* **1999,** 38, (3), 364-366.

63. Zhao, M. Q.; Crooks, R. M., Dendrimer-encapsulated Pt nanoparticles: Synthesis, characterization, and applications to catalysis. *Advanced Materials* **1999,** 11, (3), 217-+.

64. Crooks, R. M.; Zhao, M. Q.; Sun, L.; Chechik, V.; Yeung, L. K., Dendrimer-encapsulated metal nanoparticles: Synthesis, characterization, and applications to catalysis. *Accounts of Chemical Research* **2001,** 34, (3), 181-190.

65. Zhao, M. Q.; Sun, L.; Crooks, R. M., Preparation of Cu nanoclusters within dendrimer templates. *Journal of the American Chemical Society* **1998,** 120, (19), 4877-4878.

66. Garcia, M. E.; Baker, L. A.; Crooks, R. M., Preparation and characterization of dendrimer-gold colloid nanocomposites. *Analytical Chemistry* **1999,** 71, (1), 256-258.

67. Yan, X. P.; Liu, H. F.; Liew, K. Y., Size control of polymer-stabilized ruthenium nanoparticles by polyol reduction. *Journal of Materials Chemistry* **2001,** 11, (12), 3387-3391.

68. Yee, C. K.; Jordan, R.; Ulman, A.; White, H.; King, A.; Rafailovich, M.; Sokolov, J., Novel one-phase synthesis of thiol-fuctionalized gold, palladium, and iridium nanoparticles using superhydride. *Langmuir* **1999,** 15, (10), 3486-3491.

69. Zamborini, F. P.; Gross, S. M.; Murray, R. W., Synthesis, characterization, reactivity, and electrochemistry of palladium monolayer protected clusters. *Langmuir* **2001,** 17, (2), 481-488.

70. Zelakiewicz, B. S.; Lica, G. C.; Deacon, M. L.; Tong, Y. Y., C-13 NMR and infrared evidence of a dioctyl-disulfide structure on octanethiol-protected palladium nanoparticle surfaces. *Journal of the American Chemical Society* **2004,** 126, (32), 10053-10058.

71. Chen, S. W.; Huang, K.; Stearns, J. A., Alkanethiolate-protected palladium nanoparticles. *Chemistry of Materials* **2000,** 12, (2), 540-547.

72. Kim, S. W.; Kim, M.; Lee, W. Y.; Hyeon, T., Fabrication of hollow palladium spheres and their successful application to the recyclable heterogeneous catalyst for Suzuki coupling reactions. *Journal of the American Chemical Society* **2002,** 124, (26), 7642-7643.

73. Shiraishi, Y.; Ikenaga, D.; Toshima, N., Preparation and catalysis of inverted core/shell structured Pd/Au bimetallic nanoparticles. *Australian Journal of Chemistry* **2003,** 56, (10), 1025-1029.

74. Esumi, K.; Isono, R.; Yoshimura, T., Preparation of PAMAM- and PPI-metal (silver, platinum, and palladium) nanocomposites and their catalytic activities for reduction of 4-nitrophenol. *Langmuir* **2004,** 20, (1), 237-243.

75. Hayakawa, K.; Yoshimura, T.; Esumi, K., Preparation of gold-dendrimer nanocomposites by laser irradiation and their catalytic reduction of 4-nitrophenol. *Langmuir* **2003,** 19, (13), 5517-5521.

76. Garcia-Martinez, J. C.; Scott, R. W. J.; Crooks, R. M., Extraction of monodisperse palladium nanoparticies from dendrimer templates. *Journal of the American Chemical Society* **2003,** 125, (37), 11190-11191.

77. Scott, R. W. J.; Datye, A. K.; Crooks, R. M., Bimetallic palladium-platinum dendrimer-encapsulated catalysts. *Journal of the American Chemical Society* **2003,** 125, (13), 3708-3709.

78. Scott, R. W. J.; Sivadinarayana, C.; Wilson, O. M.; Yan, Z.; Goodman, D. W.; Crooks, R. M., Titania-supported PdAu bimetallic catalysts prepared from dendrimer-encapsulated nanoparticle precursors. *Journal of the American Chemical Society* **2005,** 127, (5), 1380-1381.

79. Scott, R. W. J.; Wilson, O. M.; Oh, S. K.; Kenik, E. A.; Crooks, R. M., Bimetallic palladium-gold dendrimer-encapsulated catalysts. *Journal of the American Chemical Society* **2004,** 126, (47), 15583-15591.

80. Wilson, O. M.; Scott, R. W. J.; Garcia-Martinez, J. C.; Crooks, R. M., Synthesis, characterization, and structure-selective extraction of 1-3-nm diameter AuAg dendrimer-encapsulated bimetallic nanoparticles. *Journal of the American Chemical Society* **2005,** 127, (3), 1015-1024.

81. Mevellec, V.; Roucoux, A.; Ramirez, E.; Philippot, K.; Chaudret, B., Surfactant-stabilized aqueous iridium(0) colloidal suspension: An efficient reusable catalyst for hydrogenation of arenes in biphasic media. *Advanced Synthesis & Catalysis* **2004,** 346, (1), 72-76.

82. Toshima, N.; Yonezawa, T., Bimetallic nanoparticles - novel materials for chemical and physical applications. *New Journal of Chemistry* **1998,** 22, (11), 1179-1201.

83. Yonezawa, T.; Toshima, N.; Wakai, C.; Nakahara, M.; Nishinaka, M.; Tominaga, T.; Nomura, H., Structure of monoalkyl-monocationic surfactants on the microscopic three-dimensional platinum surface in water. *Colloids and Surfaces a-Physicochemical and Engineering Aspects* **2000,** 169, (1-3), 35-45.

84. Schulz, J.; Roucoux, A.; Patin, H., Stabilized rhodium(0) nanoparticles: A reusable hydrogenation catalyst for arene derivatives in a biphasic water-liquid system. *Chemistry-a European Journal* **2000,** 6, (4), 618-624.

85. Aiken, J. D.; Finke, R. G., A review of modern transition-metal nanoclusters: their synthesis, characterization, and applications in catalysis. *Journal of Molecular Catalysis a-Chemical* **1999,** 145, (1-2), 1-44.

86. Brust, M.; Fink, J.; Bethell, D.; Schiffrin, D. J.; Kiely, C., Synthesis and Reactions of Functionlized Gold Nanoparticles. *Journal of the Chemical Society-Chemical Communications* **1995**, (16), 1655-1656.

87. Brust, M.; Walker, M.; Bethell, D.; Schiffrin, D. J.; Whyman, R., Synthesis of Thiol-derivatized Gold Nanoparticles in 2-phase Liquid-liquid System. *Journal of the Chemical Society-Chemical Communications* **1994**, (7), 801-802.

88. Toshima, N.; Harada, M.; Yonezawa, T.; Kushihashi, K.; Asakura, K., Structural-analysis of polymer-protected Pd/Pt bimetallic clusters as dispersed catalysts by using extended X-ray absorption fine-structure spetroscopy. *Journal of Physical Chemistry* **1991,** 95, (19), 7448-7453.

89. Klug, H.; Alexander, L., *X-Ray Diffraction Procedures*. John Wiley & Sons, Inc.: New York, 1962.

90. Lu, W.; Wang, B.; Wang, K.; Wang, X.; Hou, J. G., Synthesis and Characterization of Crystalline and Amorphous Palladium Nanoparticles. *Langmuir* **2003,** 19, 5887-5891.

91. Mallick, K.; Witcomb, M.; Scurrell, M., Fabrication of a nanostructured gold-polymer composite material. *European Physical Journal E* **2006,** 20, (3), 347-353.

92. Nemamcha, A.; Rehspringer, J. L.; Khatmi, D., Synthesis of palladium nanoparticles by sonochemical reduction of palladium(II) nitrate in aqueous solution. *Journal of Physical Chemistry B* **2006,** 110, (1), 383-387.

93. Narayanan, R.; El-Sayed, M. A., FTIR study of the mode of binding of the reactants on the Pd nanoparticle surface during the catalysis of the Suzuki reaction. *Journal of Physical Chemistry B* **2005,** 109, (10), 4357-4360.

94. Horinouchi, S.; Yamanoi, Y.; Yonezawa, T.; Mouri, T.; Nishihara, H., Hydrogen storage properties of isocyanide-stabilized palladium nanoparticles. *Langmuir* **2006,** 22, (4), 1880-1884.

95. Tabuani, D.; Monticelli, O.; Chincarini, A.; Bianchini, C.; Vizza, F.; Moneti, S.; Russo, S., Palladium Nanoparticles Supported on Hyperbranched Aramids: Synthesis, Characterization, and Some Applications in the Hydrogenation of Unsaturated Substrates. *Macromolecules* **2003,** 36, (4294-4301).

96. Ganesan, M.; Freemantle, R. G.; Obare, S. O., Monodisperse thioether-stabilized palladium nanoparticles: Synthesis, characterization, and reactivity. *Chemistry of Materials* **2007,** 19, (14), 3464-3471.

97. Xiong, Y. J.; McLellan, J. M.; Chen, J. Y.; Yin, Y. D.; Li, Z. Y.; Xia, Y. N., Kinetically controlled synthesis of triangular and hexagonal nanoplates of palladium and their SPR/SERS properties. *Journal of the American Chemical Society* **2005,** 127, (48), 17118-17127.

98. Ghosh, D.; Chen, S. W., Palladium nanoparticles passivated by metal-carbon covalent linkages. *Journal of Materials Chemistry* **2008,** 18, (7), 755-762.

99. Na, Y.; Park, S.; Han, S. B.; Han, H.; Ko, S.; Chang, S., Ruthenium-catalyzed Heck-type olefination and Suzuki coupling reactions: Studies on the nature of catalytic species. *Journal of the American Chemical Society* **2004,** 126, (1), 250-258.

100. Liu, Y. B.; Khemtong, C.; Hu, J., Synthesis and catalytic activity of a poly(N,N-dialkylcarbodiimide)/palladium nanoparticle composite: a case in the Suzuki coupling reaction using microwave and conventional heating. *Chemical Communications* **2004**, (4), 398-399.

101. Rahim, E. H.; Kamounah, F. S.; Frederiksen, J.; Christensen, J. B., Heck reactions catalyzed by PAMAM-dendrimer encapsulated Pd(0) nanoparticles. *Nano Letters* **2001,** 1, (9), 499-501.

102. Moreno-Manas, M.; Pleixats, R.; Villarroya, S., Fluorous phase soluble palladium nanoparticles as recoverable catalysts for Suzuki cross-coupling and Heck reactions. *Organometallics* **2001,** 20, (22), 4524-4528.

103. Gopidas, K. R.; Whitesell, J. K.; Fox, M. A., Synthesis, characterization, and catalytic applications of a palladium-nanoparticle-cored dendrimer. *Nano Letters* **2003,** 3, (12), 1757-1760.

104. Sanji, T.; Ogawa, Y.; Nakatsuka, Y.; Tanaka, M.; Sakurai, H., Metal nanoparticles derived from polysilane shell cross-linked micelle templates. *Chemistry Letters* **2003,** 32, 980-981.

105. Calo, V.; Nacci, A.; Monopoli, A.; Cotugno, P., Heck Reactions with Palladium Nanoparticles in Ionic Liquids: Coupling of Aryl Chlorides with Deactivated Olefins. *Angewandte Chemie-International Edition* **2009,** 48, (33), 6101-6103.

106. Calo, V.; Nacci, A.; Monopoli, A.; Ferola, V., Palladium-catalyzed Heck arylations of allyl alcohols in ionic liquids: Remarkable base effect on the selectivity. *Journal of Organic Chemistry* **2007,** 72, (7), 2596-2601.

107. Calo, V.; Nacci, A.; Monopoli, A.; Fornaro, A.; Sabbatini, L.; Cioffi, N.; Ditaranto, N., Heck reaction catalyzed by nanosized palladium on chitosan in ionic liquids. *Organometallics* **2004,** 23, (22), 5154-5158.

108. Yeung, L. K.; Crooks, R. M., Heck heterocoupling within a dendritic nanoreactor. *Nano Letters* **2001,** 1, (1), 14-17.

109. Ohde, H.; Ohde, M.; Wai, C. M., Swelled plastics in supercritical CO_2 as media for stabilization of metal nanoparticles and for catalytic hydrogenation. *Chemical Communications* **2004,** (8), 930-931.

110. Dupont, J.; Fonseca, G. S.; Umpierre, A. P.; Fichtner, P. F. P.; Teixeira, S. R., Transition-metal nanoparticles in imidazolium ionic liquids: Recycable catalysts for biphasic hydrogenation reactions. *Journal of the American Chemical Society* **2002,** 124, (16), 4228-4229.

111. Fonseca, G. S.; Umpierre, A. P.; Fichtner, P. F. P.; Teixeira, S. R.; Dupont, J., The use of imidazolium ionic liquids for the formation and stabilization of Ir^0 and Rh^0 nanoparticles: Efficient catalysts for the hydrogenation of arenes. *Chemistry-a European Journal* **2003,** 9, (14), 3263-3269.

112. Adlim, M.; Abu Bakar, M.; Liew, K. Y.; Ismail, J., Synthesis of chitosan-stabilized platinum and palladium nanoparticles and their hydrogenation activity. *Journal of Molecular Catalysis a-Chemical* **2004,** 212, (1-2), 141-149.

113. Semagina, N. V.; Bykov, A. V.; Sulman, E. M.; Matveeva, V. G.; Sidorov, S. N.; Dubrovina, L. V.; Valetsky, P. M.; Kiselyova, O. I.; Khokhlov, A. R.; Stein, B.; Bronstein, L. M., Selective dehydrolinalool hydrogenation with poly(ethylene oxide)-block-poly-2-vinylpyridine micelles filled with Pd nanoparticles. *Journal of Molecular Catalysis a-Chemical* **2004,** 208, (1-2), 273-284.

114. Atobe, M.; Okamoto, M.; Fuchigami, T.; Park, J. E., Selective hydrogenation by polymer-encapsulated platinum nanoparticles prepared by an easy single-step sonochemical synthesis. *Ultrasonics Sonochemistry* **2010,** 17, (1), 26-29.

115. Guo, S.; Liew, K. Y.; Li, J., Catalytic Activity of Ruthenium Nanoparticles Supported on Carbon Nanotubes for Hydrogenation of Soybean Oil. *Journal of the American Oil Chemists' Society* **2009,** 86, (12).

116. Schmidt, E.; Kleist, W.; Krumeich, F.; Mallat, T.; Baiker, A., Platinum Nanoparticles: The Crucial Role of Crystal Face and Colloid Stabilizer in the Diastereoselective Hydrogenation of Cinchonidine. *Chemistry-a European Journal* **2010,** 16, (7), 2181-2192.

117. Niu, Y. H.; Yeung, L. K.; Crooks, R. M., Size-selective hydrogenation of olefins by dendrimer-encapsulated palladium nanoparticles. *Journal of the American Chemical Society* **2001,** 123, (28), 6840-6846.

118. Schimpf, S.; Lucas, M.; Mohr, C.; Rodemerck, U.; Bruckner, A.; Radnik, J.; Hofmeister, H.; Claus, P., Supported gold nanoparticles: in-depth catalyst characterization and application in hydrogenation and oxidation reactions. *Catalysis Today* **2002,** 72, (1-2), 63-78.

119. Sharma, R. K.; Sharma, P.; Maitra, A., Size-dependent catalytic behavior of platinum nanoparticles on the hexacyanoferrate(III)/thiosulfate redox reaction. *Journal of Colloid and Interface Science* **2003,** 265, (1), 134-140.

120. Clint, J. H.; Collins, I. R.; Williams, J. A.; Robinson, B. H.; Towey, T. F.; Cajean, P.; Khanlodhi, A., Synthesis and Characterization of Colloidal Metal and Semiconductor Particles Prepared in Microemulsions. *Faraday Discussions* **1993,** 95, 219-233.

121. Freund, P. L.; Spiro, M., Colloidal catalysis - the effect of sol sizee and concentration. *Journal of Physical Chemistry* **1985,** 89, (7), 1074-1077.

122. Freund, P. L.; Spiro, M., Catalysis by colloidal gold of the reaction between ferricyanide and thiosolfate ions. *Journal of the Chemical Society-Faraday Transactions I* **1986,** 82, 2277-2282.

123. Bell, A. T., The impact of nanoscience on heterogeneous catalysis. *Science* **2003,** 299, (5613), 1688-1691.

124. He, F.; Zhao, D. Y., Preparation and characterization of a new class of starch-stabilized bimetallic nanoparticles for degradation of chlorinated hydrocarbons in water. *Environmental Science & Technology* **2005,** 39, (9), 3314-3320.

125. Xu, J.; Bhattacharyya, D., Membrane-based bimetallic nanoparticles for environmental remediation: Synthesis and reactive properties. *Environmental Progress* **2005,** 24, (4), 358-366.

126. Wang, X. Y.; Chen, C.; Liu, H. L.; Ma, J., Preparation and characterization of PAA/PVDF membrane-immobilized Pd/Fe nanoparticles for dechlorination of trichloroacetic acid. *Water Research* **2008,** 42, (18), 4656-4664.

127. Wong, M. S.; Alvarez, P. J. J.; Fang, Y. I.; Akcin, N.; Nutt, M. O.; Miller, J. T.; Heck, K. N., Cleaner water using bimetallic nanoparticle catalysts. *Journal of Chemical Technology and Biotechnology* **2009,** 84, (2), 158-166.

128. You, C. C.; Chompoosor, A.; Rotello, V. M., The biomacromolecule-nanoparticle interface. *Nano Today* **2007,** 2, (3), 34-43.

129. You, C. C.; Verma, A.; Rotello, V. M., Engineering the nanoparticle-biomacromolecule interface. *Soft Matter* **2006,** 2, (3), 190-204.

130. Ghosh, P. S.; Han, G.; Erdogan, B.; Rosado, O.; Krovi, S. A.; Rotello, V. M., Nanoparticles featuring amino acid-functionalized side chains as DNA receptors. *Chemical Biology & Drug Design* **2007,** 70, (1), 13-18.

131. Phillips, R. L.; Miranda, O. R.; You, C. C.; Rotello, V. M.; Bunz, U. H. F., Rapid and efficient identification of bacteria using gold-nanoparticle - Poly(para-phenyleneethynylene) constructs. *Angewandte Chemie-International Edition* **2008,** 47, (14), 2590-2594.

132. Richter, H.; McCarthy, K.; Nevin, K. P.; Johnson, J. P.; Rotello, V. M.; Lovley, D. R., Electricity generation by Geobacter sulfurreducens attached to gold electrodes. *Langmuir* **2008,** 24, (8), 4376-4379.

133. Bajaj, A.; Miranda, O. R.; Kim, I. B.; Phillips, R. L.; Jerry, D. J.; Bunz, U. H. F.; Rotello, V. M., Detection and differentiation of normal, cancerous, and metastatic cells using nanoparticle-polymer sensor arrays. *Proceedings of the National Academy of Sciences of the United States of America* **2009,** 106, (27), 10912-10916.

134. De, M.; Ghosh, P. S.; Rotello, V. M., Applications of Nanoparticles in Biology. *Advanced Materials* **2008,** 20, (22), 4225-4241.

CHAPTER II

SYNTHESIS, CHARACTERIZATION AND ELECTROCHEMICAL PROPERTIES OF PALLADIUM AND RUTHENIUM METALLIC NANOPARTICLES

1. Introduction

There has been intense interest in the development of procedures for the fabrication of transition metal nanoparticles, especially for palladium and ruthenium nanoparticles[1-3]. The interest stems from the ability of these metals to effectively catalyze important organic reactions and industrial processes[4]. The properties of both palladium and ruthenium with nanoscale dimensions are expected to vary significantly from their bulk counterparts. New unique properties emerge on the nanoscale due to quantum confinement and because of the particle dimensions are in the order of the electron mean-free path[5, 6].

A major need in improving catalyst performance is fabricating the particles so that they are uniform in morphology. The key is to rationally select an appropriate precursor, an effective reducing agent and a suitable stabilizing ligand. Examples of stabilizing ligands used for nanoparticle fabrication include polymers, thiol based ligands, dendrimers, phosphine based ligands, DNA, etc[7]. We developed a new methodology that uses thioether as reducing agent and stabilizer. In the reducing process, the metal precursors were reduced by thioether to zero-valent state, while the sulfur of thioether was oxidized to sulfoxide or sulfonic component. In the stabilizing process, the sulfur in thioether form dative bonds with particle surface atoms, while its two long carbon chain tails dangle in the solvent and sterically very well shield the particle surface.

Nanoparticle surfaces are typically passivated by a protective layer or a stabilizer. The role of the stabilizer is to prevent nanoparticles from aggregation and to provide solubility in a solvent. Uniformly isolated particles can easily be analyzed using electrochemistry. Murray and coworkers proposed that monolayer-protected metallic nanoparticles displayed molecule-like double layer capacitive charging (electron transfer)[8-10]. As mentioned in Chapter I, the continuous electronic energy level that is represented in bulk metals transitions to molecule-like distinct energy levels represented in nanoparticles with diameters below 5 nm. The most extensive electron transfer studies on metal nanoparticles have been carried out on Au nanoparticles with diameters < 2 nm. Within this size range, Au nanoparticles were found to behave like capacitors and exhibited successive single electron transfers due to their distinct electron energy levels[8, 11-14]. Quantized double layer charging is one of the most interesting properties of small metallic nanoparticles and has been applied in catalysis and in nanoscale electronic circuitry[15]. These unique characteristics have not been extensively investigated for metals other than Au due to the difficulty in obtaining uniform metal nanoparticles with diameters below 5 nm.

It has been shown, at least in the case of Au nanoparticles, when they are brought close to the surface of a charged semiconductor, there tends to be equilibration of the Fermi level between the semiconductor and the Au nanoparticle[16-19]. The contact of noble metals to semiconductor surface is beneficial for minimizing the charge recombination and thereafter the efficiency of the photocatalytic reduction or oxidation. The metallic nanoparticles act as electron sinks for photo-induced charge carriers in semiconductors, improving the charge separation, photocurrent and catalytic properties. Whether this property translates well to other transition precious metal nanoparticles, such as palladium and ruthenium, remains to be investigated. Different compositions of metal nanoparticles has been shown to have an effect on the charge rectification in semiconductor nanostructures[20]. The ability to understand such phenomena in various transition metal nanoparticles could lead to better ways of modulating charge transfer for improved chemical reactions.

In this chapter, a synthesis procedure to obtain uniform and size controllable Pd and Ru nanoparticles are discussed. Electrochemical characterization of the nanoparticles was carried out, which aid in developing an understanding of electronic properties of the nanoparticles.

2. Experimental details

Materials. *n*-dodecyl sulfide (93%), toluene, acetone, methanol and other solvents were purchased from VWR. Ruthenium acetylacetonate Ru[$(CH_3CO)_2CH_3$] and palladium acetate [$Pd_3(OAc)_6$] were purchased from Strem Chemicals. Acetic acid and nitric acid were obtained from Fisher Scientific. Titanium (IV) isopropoxide (Ti(*i*-OPr)$_4$) (Aldrich), iron (III) proptoporphyrin chloride (Frontier Scientific), and polyethylene glycol (M_n 10,000, Sigma Aldrich) were used as received. A general purpose acid digestion bomb was purchased from Parr Instrument Company. A custom-designed quartz cuvette with a 1 cm path length was used as the optical spectrometry cell. All glassware and Teflon coated stir bars were cleaned with aqua regia, thoroughly washed with deionized water and acetone, and dried in an oven before use.

2.1 Synthesis of Pd and Ru metallic nanoparticles

Synthesis of palladium nanoparticles. Palladium acetate [$Pd_3(OAc)_6$] (0.02 g, 0.03 mmol) and *n*-dodecyl sulfide (0.165 g, 0.45 mmol) [mole ratio of Pd^{2+}:dodecyl sulfide is 1:15] were dissolved in 10 mL toluene resulting in a bright yellow solution. The solution was degassed and filled with nitrogen before reflux at 95°C for the desired time frame. A dark brown colloidal solution of Pd nanoparticles was produced. The solution was cooled and stored in a deaerated environment.

Synthesis of ruthenium nanoparticles. Ruthenium acetylacetonate (0.02 g, 0.05 mmol) and *n*-dodecyl sulfide (0.19 g, 0.5 mmol) [mole ratio of Ru^{3+}:dodecyl sulfide is 1:10] were dissolved in 10 mL diphenyl ether to form a bright red solution. The solution was deareated for 10 minutes, then purged with nitrogen gas. The solution was stirred and heated from room temperature to ~240°C for designated periods of time during which the solution gradually changed color from bright red to black. After the prescribed period of time had expired, the colloidal solution was allowed to cool under nitrogen for 24 hours with continued stirring.

2.2 Characterization of Pd and Ru metallic nanoparticles

The particles were then precipitated using an equivolume quantity of dry methanol, followed by centrifugation at 15K rpm for 2 minutes. The resulting black pellet was washed with methanol and redispersed in a solution of dichloromethane to give a black colloid.

Transmission electron microscope (TEM). 1 μL of the nanoparticle solution was placed on a carbon-coated copper grid covered with formvar. The sample was allowed to dry in a vacuum desiccator before being placed in the instrument for imaging. A JEOL electron microscope, Model JEM-1230 was used to obtain TEM images. A JEOL 3011 high-resolution transmission electron microscope (HRTEM) was used for high resolution images and selected area electron diffraction (SAED) measurements.

Powder X-ray diffraction (XRD). XRD patterns were collected on a Scintag XDS Model 2000 diffractometer. Samples were prepared by precipitating the as-prepared nanoparticles with dry methanol followed by centrifugation at 15K rpm for 10 minutes. The pellet was washed with acetone twice, centrifuged and the resulting product was dried under vacuum at 50°C for 72 h. The dry nanoparticle sample was mixed with 325 mesh Si powder and placed on a Si wafer sample holder.

2.3 Electrochemical characterization of monometallic nanoparticles

Electrochemical results were obtained using a BASi Epsilon potentiostat. 0.1 M electrolyte tetra-*n*-butylammonium hexaflourophosphate (Bu_4NPF_6) was added to 1:1 (v/v) CH_2Cl_2/sample solution. The cell was purged with N_2 gas for at least 20 minutes. Differential pulse voltammetry (DPV) measurements were carried out using Pt wires (0.4 mm in diameter) as working and counter electrodes and Ag wire (0.5 mm in diameter) as a quasi-reference electrode (Figure 2.1). Prior to use, the working electrode was polished with 0.05 μm Al_2O_3 slurries and rinsed thoroughly with copious amounts of acetone. This was followed by drying using a steam of N_2 gas or compressed air.

The scan rate was set at 20 mV/sec, the pulse amplitude was 50 mV, the sample width was 17 msec, the pulse width was 50 msec, and the pulse period was 200 msec. The potential scanning range was from -1500 mV to 1500 mV. A background scan was conducted in 1:1 (v/v) CH_2Cl_2/diphenyl ether (or toluene).

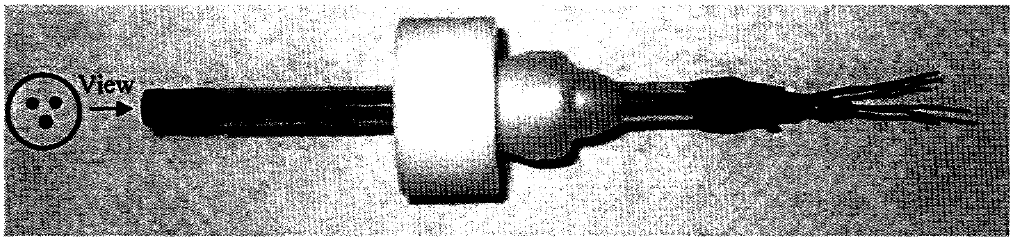

Figure 2.1 Home-made three electrode systems. Two Pt wires (0.4 mm in diameter) and one Ag wire (0.5 mm in diameter) are confined in polymer resin. Three electrodes are separated but very close to each other in a triangle arrangement.

2.4 Charging and discharging of the metallic nanoparticles

Preparation of TiO_2 nanoparticle thin films. Transparent nanocrystalline TiO_2 thin films coated on glass slides were prepared from colloidal TiO_2, which was made by hydrolysis of Ti(*i*-OPr)$_4$ by a sol-gel method[21, 22]. An aqueous solution consisting of 120 mL of milliQ water and 0.84 mL of 70% nitric acid was prepared in a 250 mL round-bottom flask. A 20 mL aliquot of Ti(*i*-OPr)$_4$ was added dropwise to the aqueous solution over 2 hours while the solution was vigorously stirred. A thick white solution formed during the process. The mixture was then heated to reflux with continued stirring for 5 h at 80 ~ 90°C. The solution became nearly transparent during this time. Heating was continued at 90°C until the volume of the solution decreased to 40 mL.

About 18 mL of the resulting semi-transparent solution was added to the acid bomb and sintered at 200°C for 8 h. About 0.3 g of polyethylene glycol was added to the resulting mixture stirred for an additional 6-8 h. This final mixture was then applied to glass slides to make a transparent thin film.

Irradiation of TiO_2. The TiO_2 slides were placed diagonally in a customized quartz cuvette which was filled with methanol to cover the TiO_2 film in the glass slide. The cuvette was sealed with a rubber septum and then purged with N_2 gas for at least 20 min before photolysis. Under the air-free environment, the TiO_2 slide was irradiated with a 1000 W xenon lamp. A 320 nm UV cut-off filter (Newport, FSQ-WQ320) was used. The absorbance spectra of the TiO_2 slides in methanol were acquired using a Cary 50 spectrophotometer before and after successive 5 min photolysis.

Charge transfer from TiO_2 to Pd or Ru nanoparticles: After the irradiation of TiO_2, the cuvette holding the TiO_2 thin film in methanol was removed from the lamp and then the as prepared Pd or Ru nanoparticles were injected into the cuvette in 1 μL aliquots (15 μM) using an air-tight syringe. UV-visible absorbance spectra were recorded 10 minutes after each aliquot was added. Hemin was used as the redox indicator to evaluate whether any charges stored in the metal nanoparticles could be discharged.

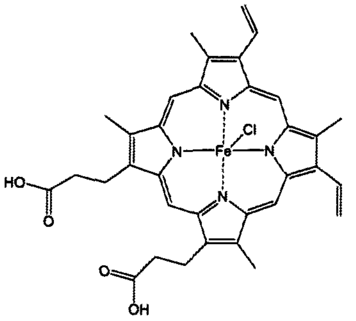

Iron (III) protoporphyrin chloride (Hemin)

3. Results and discussion

3.1 Synthesis and characterization of Pd nanoparticles

The size of a nanoparticle along with its surface atoms is characteristics that often determine the particle's chemical and physical properties. Obtaining metal nanoparticles that are uniform and with diameters below 5 nm is a challenging synthetic task. When adopting wet-chemical methods, reaction conditions (such as temperature, time, ratio of reactant and stabilizer, etc.) have to be precisely controlled in order to obtain monodisperse nanoparticles.

We have successfully synthesized monodispersed Pd nanoparticles with controlled size using thioethers as stabilizers. NMR spectroscopy confirmed that the thioethers bind to the metal surface via a dative bond[23] [24]. These thioether ligands passivate the particle surface, prevent particle aggregation, and allow the particles to exist as colloids in organic solvents. The mechanism of nanoparticle growth by the chemical reduction method can be described in four stages: nucleation, particle growth, Oswald ripening, and surface passivation. Before the metal precursors are completely consumed or passivated by surface stabilizing ligand, particle growth continues in order to reduce the overall surface energy. Our group has discovered that higher temperature (higher reaction rate) or longer reaction time produce bigger nanoparticles until the metal precursors are completed consumed[24]. Therefore, the nanoparticle size s can be tuned by controlling the temperature and the reaction time. Figure 2.2 shows the particles that synthesized at 95°C at designated reaction time. Using *n*-dodecyl sulfide as stabilizer, 60 min reaction generated 1.7 nm nanoparticles, 70 min reaction generated 1.9 nm nanoparticles, 80 min for 2.1 nm, and 90 min for 2.5 nm. From the size distribution histogram, the nanoparticles were uniform in size.

The HRTEM image shown in Figure 2.3a shows the twinning feature which is typical for most metal nanoparticles. The selected area electron diffraction pattern shown in Figure 2.3b of a single Pd crystal exhibits 3 diffused rings which are assigned to the (111), (220) and (311) reflections that are characteristic of a face-centered cubic (*fcc*) structure[25]. The powder x-ray diffraction (Figure 2.3c) results of the Pd nanoparticles exhibited (111), (200), (220) and (311) diffraction peaks at 40°, 47°, 68° and 82° respectively, and also indicated the existence of the *fcc* structure of Pd nanoparticles[26-28]. The average particle size calculated based on the line broadening of (111) by using the Scherrer formula was about 3.0 nm, which is close to the value of the particle measured by TEM images (3.5 nm).

3.2 Electrochemistry of Pd nanoparticles

Electrochemical techniques such as cyclic voltammetry or differential pulse voltammetry are useful in understanding the properties of quantized metal nanoparticles. In previous reports, DPV of alkanethiol-stabilized Pd nanoparticles with diameters less than 3 nm displayed quantized double-layer (QDL) charge transfer, and thus behaved in a similar manner to capacitors[29, 30]. However, the peaks they observed were not well-defined, because the success of these measurements relies on the presence of uniform and small Pd nanoparticles for accurate QDL measurement. The DPV of octyl sulfide stabilized Pd nanoparticles is shown in Figure 2.4, the presence of distinct peaks indicates that the particles are quite monodisperse in size, and each peak relates to successive oxidation and reduction. The multiple reversible waves in the potential ranging from -1500 mV to 1500 mV indicate the reversible single-electron transfer process.

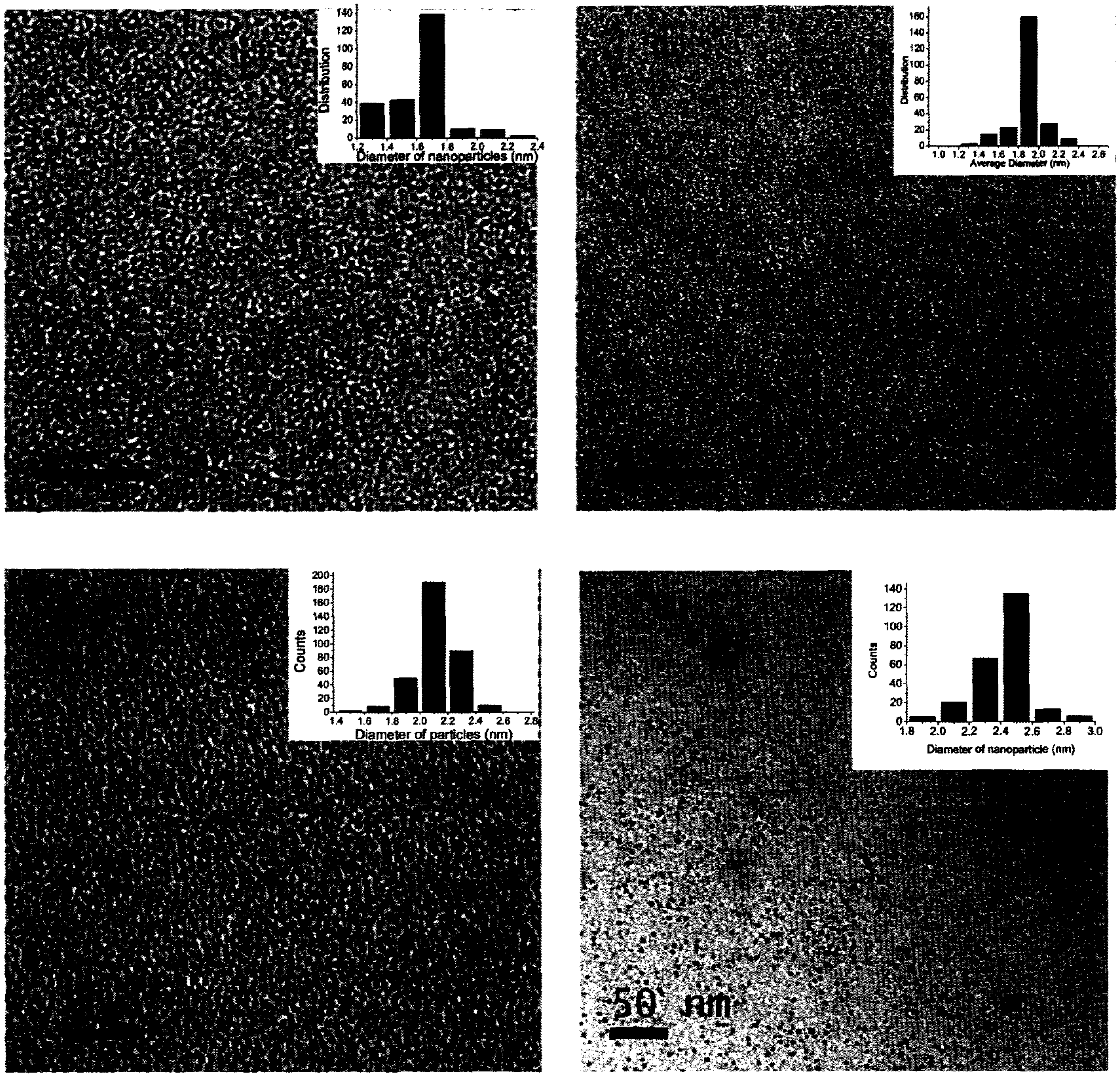

Figure 2.2 TEM images of Pd nanoparticles stablized by *n*-dodecyl sulfide with diameter of (a) 1.7 nm , (b) 1.9 nm, (c) 2.1 nm, and (d) 2.5 nm. The inset in each image present the size distribution histogram. The synthesis was carried out at 95°C for (a) 60 min, (b) 70 min, (c) 80 min, and (d) 90 min.

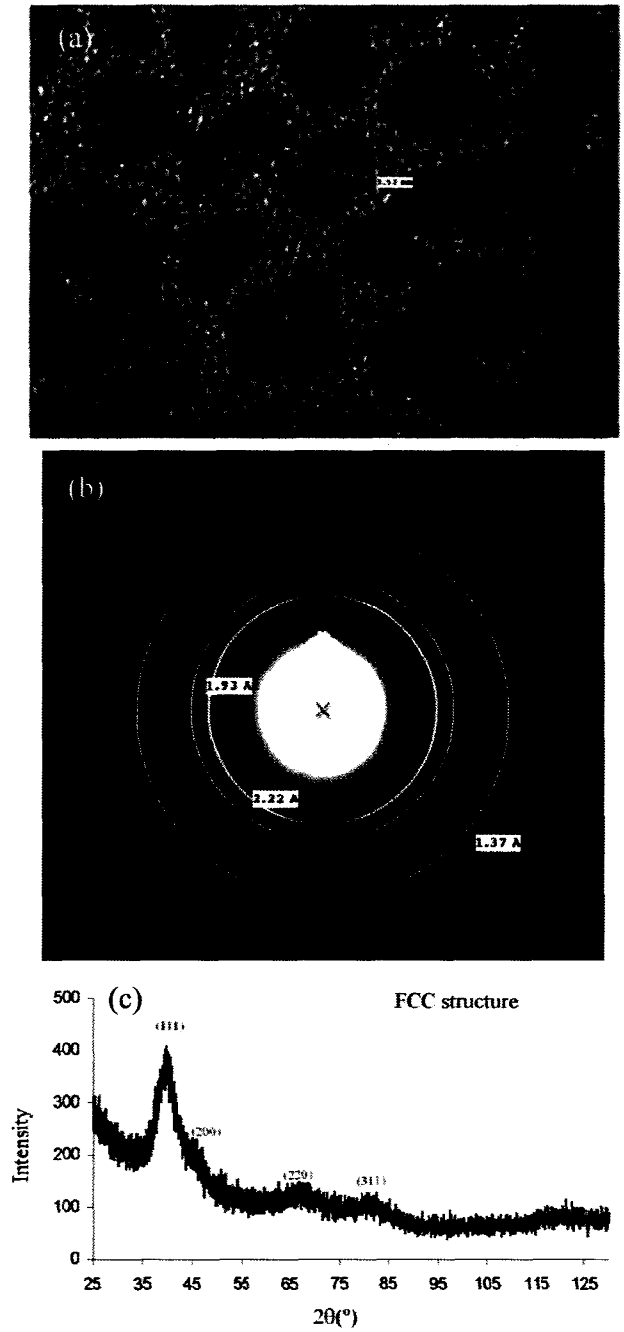

Figure 2.3 HRTEM image (a), SAED (b) and XRD (c) of *n*-dodecyl sulfide stabilized Pd nanoparticles with size of 3.5 ± 0.1 nm.

The data allow the average size of Pd particle to be calculated by the equation, which is defined as "Concentric Sphere Capacitance Model"[11],

$$\Delta V = \frac{e}{C_{MPC}} = \frac{ed}{4\pi\varepsilon\varepsilon_0 r(r+d)}$$

where ΔV is the spacing between the peaks (the energy needed for single electron transfer), e is the electronic charge (1.6×10^{-19} coulombs), d is the thickness of the monolayer medium, ε is the dielectric constant of the monolayer medium around the metal core, ε_0 is the permittivity of free space [8.85×10^{-12} F m^{-1} (or C^2 N^{-1} m^2)] and r is the radius of the metal core. It should be noted that this simplified approach is based only on the electrostatic interaction but the identity of the core metal is not taken into account. Chen reported that quantized capacitance charging is insensitive to the core metal when the particle size is larger than 5 nm, because the main energetic barrier of electron transfer in large sized particles was due to electrostatic interactions. However, the discrete energetic states in metallic particles that arise with sizes below 5 nm could be dependent on the type of metal. [30].

In Figure 2.4, the first current peak in the negative potential scan corresponds to the pseudo-formal potential of the $Pd^{0/1-}$ redox couple, the second peak to the $Pd^{1-/2-}$ couple, etc. The average peak spacing in negative potential region is 484 ± 10 mV. The gap between first oxidation and first reduction peak is 1600 mV, which is actually the HOMO-LUMO gap. The equal spacing between the peaks indicates the quantized double-layer electron charging and discharging. Using the concentric sphere capacitance model, the calculated size (1.5 nm according to the DPV spectrum in Figure 2.4) is slightly smaller than TEM measurement (2.1 nm according to the

TEM image). Several reasons were proposed to explain this discrepancy. First, an interaction of the Pd nanoparticles with the TEM grid may have altered the structure of the Pd nanoparticles[31]. Second, Pd does not provide a good contrast, which makes it difficult to resolve particles of less than 2 nm[32]. Third, the parameters in the equation are arbitrary in varying environmental conditions[29]. It was widely accepted that ε for the organic shell (especially for alkanethiolate $HS(CH_2)_nCH_3$ with $n = 3 - 23$) has a value of 3. Because of the similar structure of thioether with alkanethiolates, we also used this number for the ε value. There have been a number of arguments regarding the reliability of nanoparticle size determination by TEM *versus* electrochemistry. For example, Zamborini's group[29] and Chen's group[30] assumed the TEM histograms to be correct, and the calculation to be questionable since the ε is size-dependent. Crooks' group[32] proposed that the TEM data was less reliable than electrochemistry results, because of the poor resolution of very small particles in TEM images and the large size distribution of their particles.

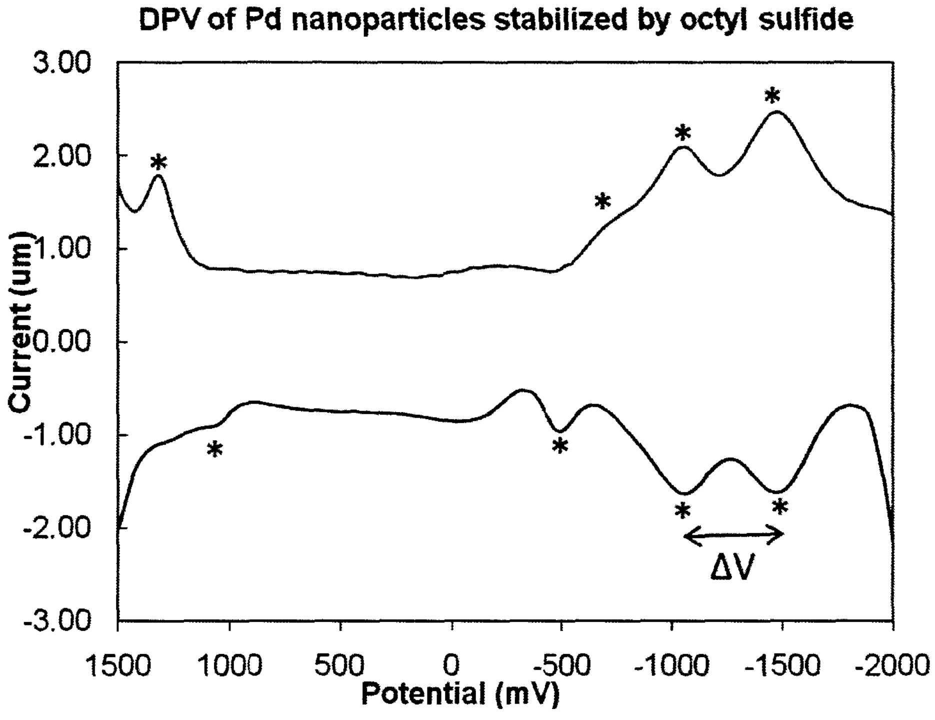

Figure 2.4 DPV spectrum (WE: Pt wire, CE: Pt wire, RE: Ag wire) of octyl sulfide stabilized Pd nanoparticles with 2.1 nm in diameter

Figure 2.5 displays the DPV spectra of 1.7 nm, 1.9 nm and 2.1 nm Pd nanoparticles. Table 2.1 lists the particle size obtained by TEM measurement and the corresponding measurement obtained using the concentric sphere model. The ΔV value increases when the size decreases, indicating the more parted energetic levels due to the stronger quantum confinement. The HOMO-LUMO gap also increases with decreasing size, except that the gap for 1.9 nm nanoparticles is smaller than that for 2.1 nanoparticles. This may be due to the undefined oxidation peak for 1.9 nm nanoparticles in the DPV spectrum. The calculated diameters are smaller than the TEM measurement. In this particular case, it appears that the quantized double layer capacitance charge transfer is sensitive to the core materials.

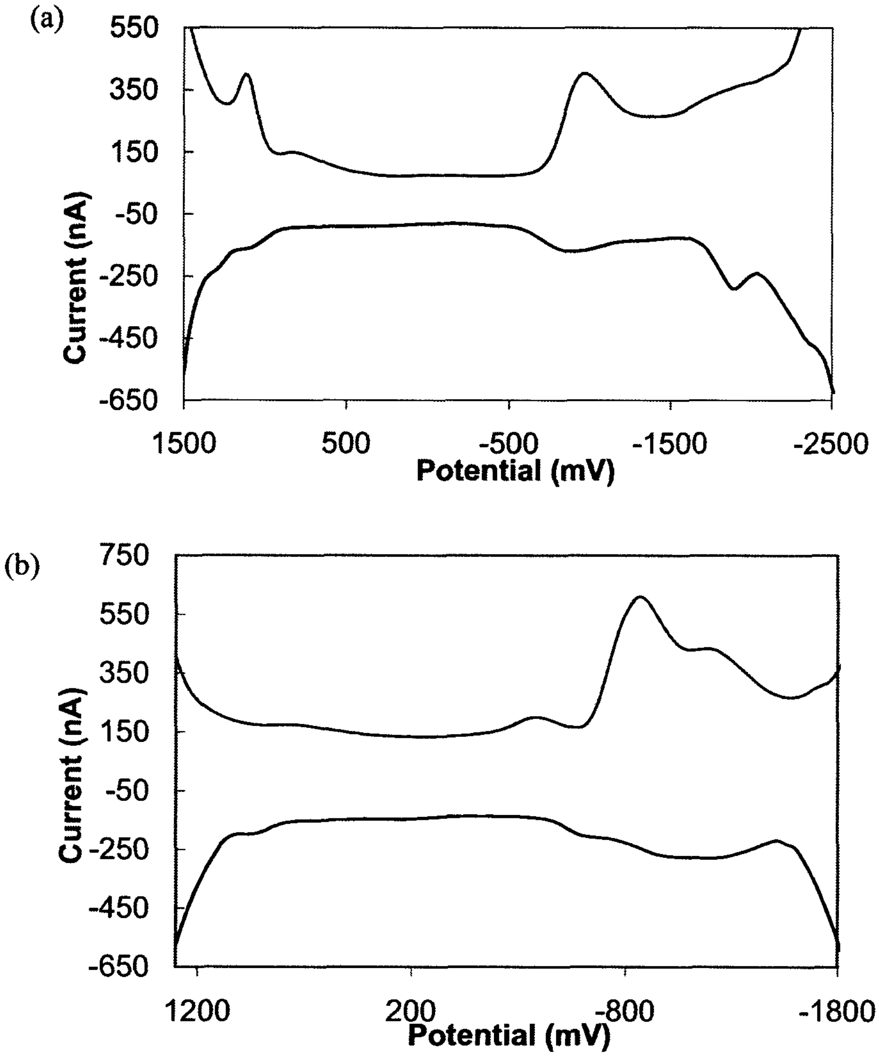

(c)

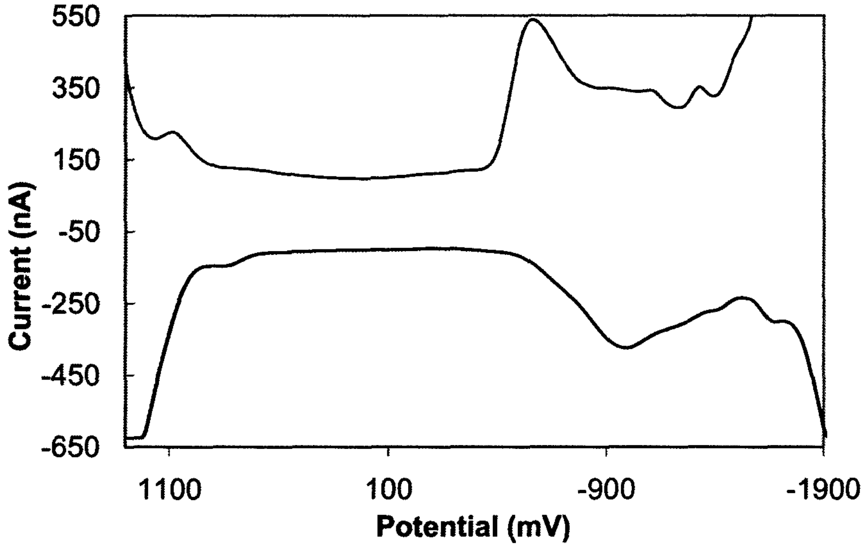

Figure 2.5 DPV spectra of *n*-dodecyl sulfide stablized Pd nanoparticles synthesized at 95°C for (a) 60 minutes, (b) 70 minutes, and (c) 80 minutes.

Table 2.1 Charge transfer of size-controlled Pd nanoparticles

Reaction Time	60 min	70 min	80 min
Diameter (nm) - TEM measurement	1.7	1.9	2.1
ΔV (mV)	485	440	320
HOMO-LUMO gap (mV)	2060	1344	1586
Diameter (nm) – Calculated	1.5	1.6	2.0

3.3 Synthesis and characterization of Ru nanoparticles

Ruthenium acetylacetonate was used as the precursor for synthesis of Ru nanoparticles. Phenyl ether was used as the solvent due to its high boiling point. The reaction took place at 240°C to allow the decomposition of the ligands on the precursor. After the reaction had progressed for 40 minutes the initial red color of the solution had turned to a dark brown indicating the formation of Ru nanoparticles. Figure 2.6 displays TEM images of the Ru nanoparticles with different sizes obtained by controlling the reaction time. These Ru nanoparticles were colloidal and were found to be stable in a nitrogen atmosphere.

HRTEM (Figure 2.7) confirmed the crystallinity of the nanoparticles and the inter-lattice spacing *d* value obtained, 2.11 Å, is consistent with ruthenium metal[26, 33, 34]. Powder XRD diffraction (Figure 2.8) was carried out on the nanoparticles with an average diameter of 1.7 nm. The pattern showed a broad peak due to the small size of the particles. The Bragg angle at $2\theta = 43.3°$ corresponds to the Ru (101) diffraction[26]. Calculation of the crystal size using the Scherrer formula is also in agreement with the mean particle diameter obtained by TEM measurements.

3.4 Electrochemistry of Ru nanoparticles

A typical voltammogram for 1.7 nm Ru nanoparticles is shown in Figure 2.9. Multiple distinct peaks were acquired in the -1300 mV to 1300 mV potential range. There are four pairs of well-defined voltammetric peaks with formal potentials listed in Table 2.2. The average potential spacing (ΔV) between adjacent quantized charging peaks is about 420 mV, hence the capacitance (C) of the 1.7 nm Ru nanoparticles was evaluated ($C = e/\Delta V$ with e being the electronic charge) to be about 0.41 aF. According to the concentric sphere capacitance model, the nanoparticles can be estimated as approximately 1.7 nm by assuming $\varepsilon = 3$ and d is equal to 1.34 nm for fully extended *n*-dodecyl sulfide measured in the Gaussian theoretical calculation program.

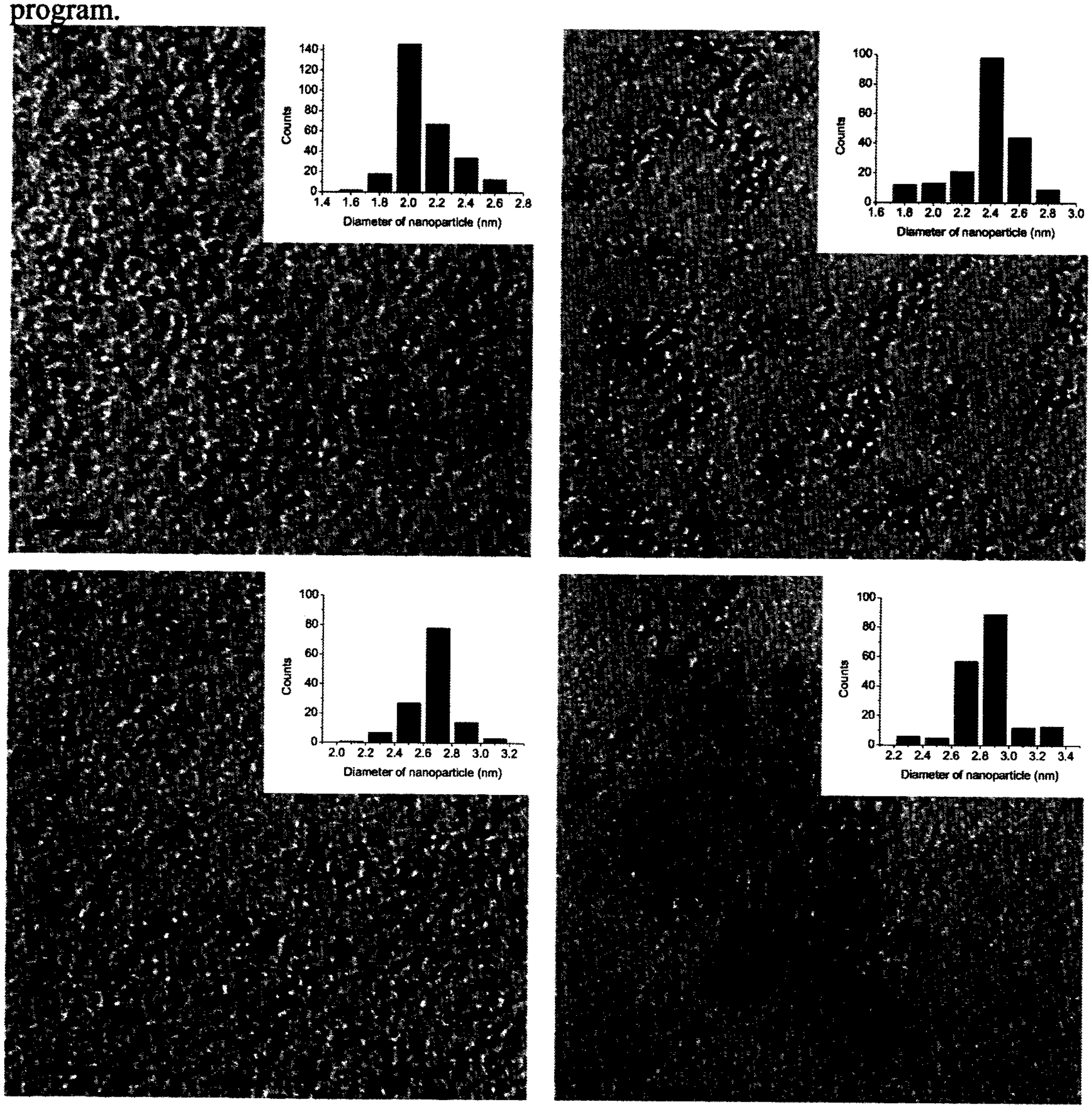

Figure 2.6 TEM images of *n*-dodecyl sulfide stabilized Ru nanoparticles with diameter of (a) 2.0 nm, (b) 2.4 nm, (c) 2.7 nm, (d) 2.9 nm. They were

made in reaction times of (a) 60 mn, (b) 75 min, (c) 90 min, (d) 120 min at 240°C.

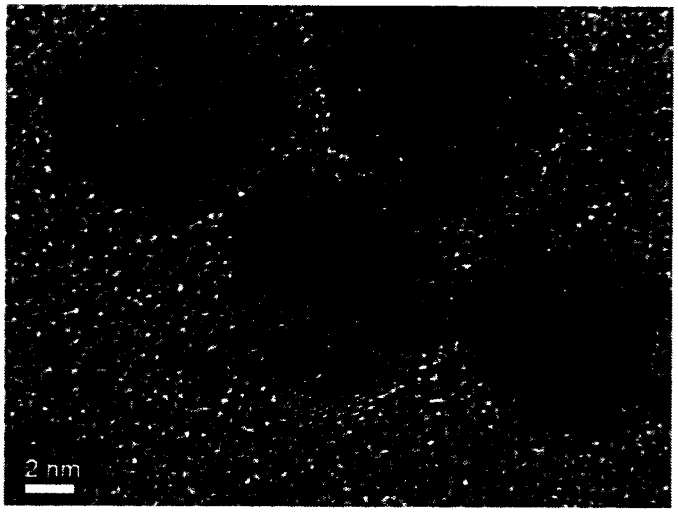

Figure 2.7 High resolution transmission electron micrograph of 6.2 ± 0.4 nm ruthenium nanoparticles.

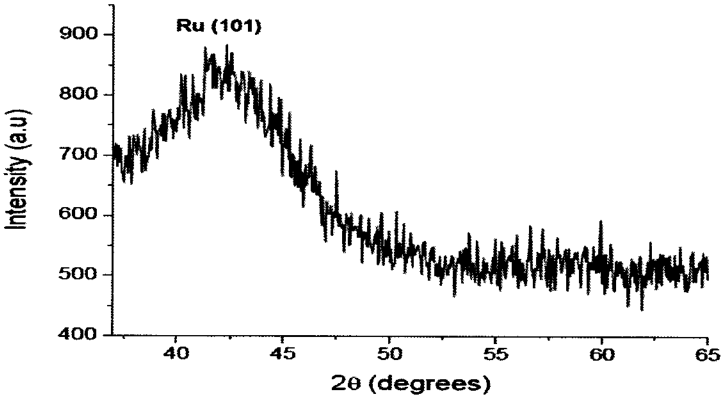

Figure 2.8 Powder XRD pattern of ruthenium nanoparticles with an average diameter of 1.7 nm

Quantized charging studies on Ru nanoparticles are rarely reported, most probably because of the difficulty in making nanometer-sized stable and monodispersed particles. Chen' group synthesized carbene-protected Ru nanoparticles and studied their electrochemical properties[35]. They observed quantized charging characteristics for the core diameter of 2.12 ± 0.72 nm. However, the electrochemical properties of various sizes of Ru nanoparticles have not been reported. Therefore, we synthesized three different sizes of Ru nanoparticles by varying the reaction time (60 minutes, 90 minutes, and 120 minutes) at 240°C (Figure 2.6). Figure 2.10 displays the DPV spectra for the varying sizes (only anodic peaks are shown). It can be observed that the shapes of the spectra are similar to the only difference being in the peak spacing which represents size dependant energy levels. The HOMO-LUMO gap and ΔV increase when the size of the particles decrease (Table 2.3). However, there is an exception in that the 2.7 nm (TEM measurement) particles show slightly higher ΔV than 2.4 nm particles. This may be due to the size distribution being slightly broader relative to the other Ru nanoparticles investigated. The calculated values of size were off the TEM measurements (Table 2.3). This suggested that for Ru nanoparticles in this particular size range, concentric sphere capacitance equation is sensitive to the core material.

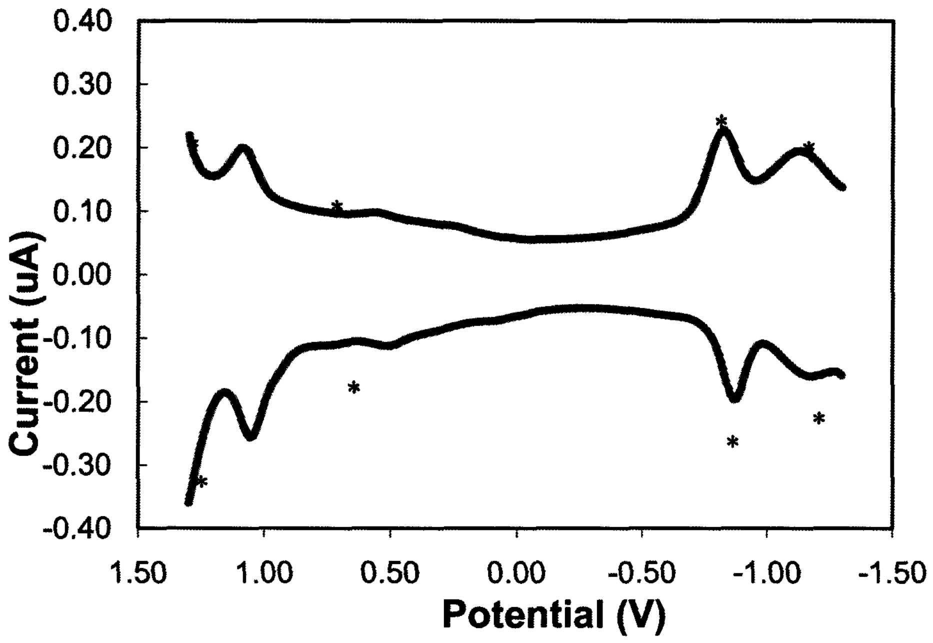

Figure 2.9 DPV spectrum of *n*-dodecyl sulfide stablized Ru nanoparticles with diameter of 1.7 nm. HOMO-LUMO gap = 1390 mV. The average ΔV = 420mV.

Table 2.2 Peak Potentials of of *n*-dodecyl sulfide stablized Ru nanoparticles with size of 1.7 nm

Peak No.	E_a [a](V)	E_c [a](V)	E^o (V)	Redox Couple
1	+1.12	+1.03	+1.08	$Ru^{+2/+1}$
2	+0.59	+0.48	+0.54	$Ru^{+1/0}$
3	-0.80	-0.89	-0.85	$Ru^{0/-1}$
4	-1.11	-1.19	-1.15	$Ru^{-1/-2}$

[a] Subscripts (a and c) denote anodic and cathodic peaks, respectively. All potentials are referenced to the Ag quasi-reference, and data are collected from the DPV measurements in Figure 2.5.

(a)

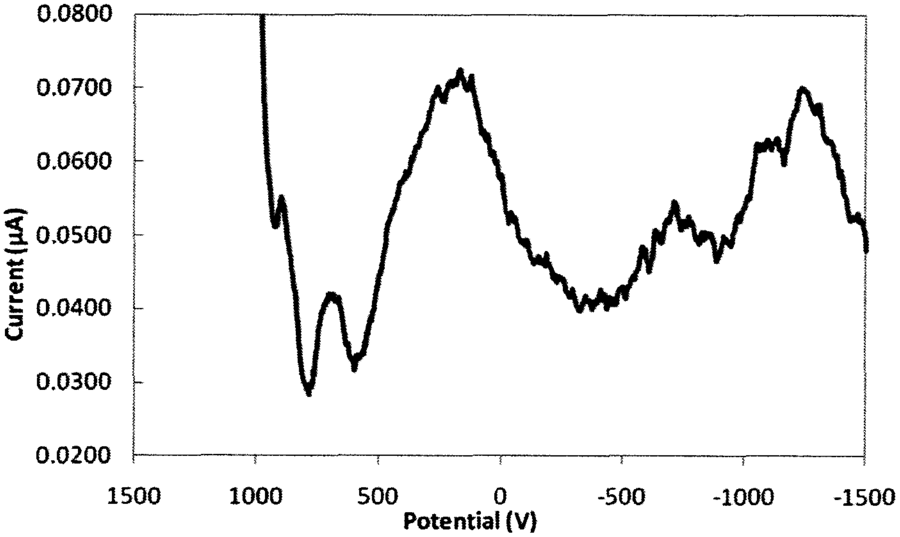
0.0800
0.0700
0.0600
0.0500
0.0400
0.0300
0.0200
Current (μA)
1500
1000
500
0
-500
-1000
-1500
Potential (V)

(b)

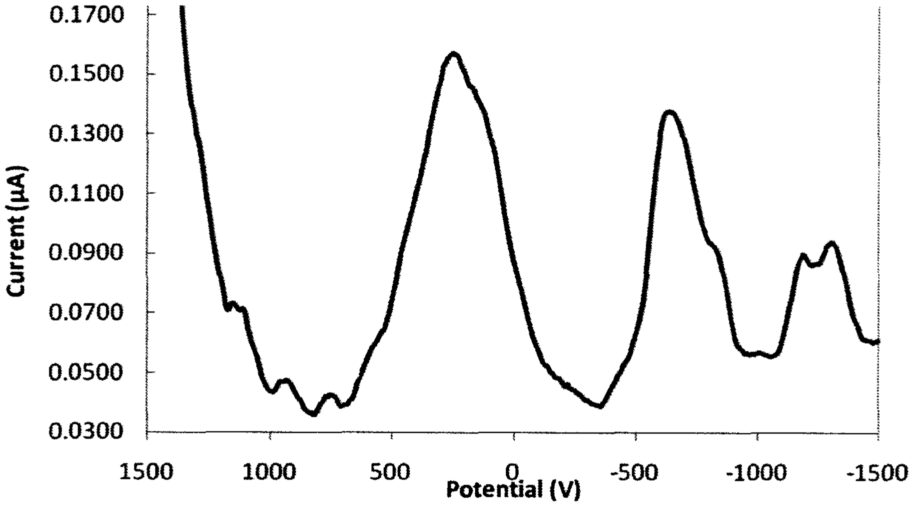
0.1700
0.1500
0.1300
0.1100
0.0900
0.0700
0.0500
0.0300
Current (μA)
1500
1000
500
0
-500
-1000
-1500
Potential (V)

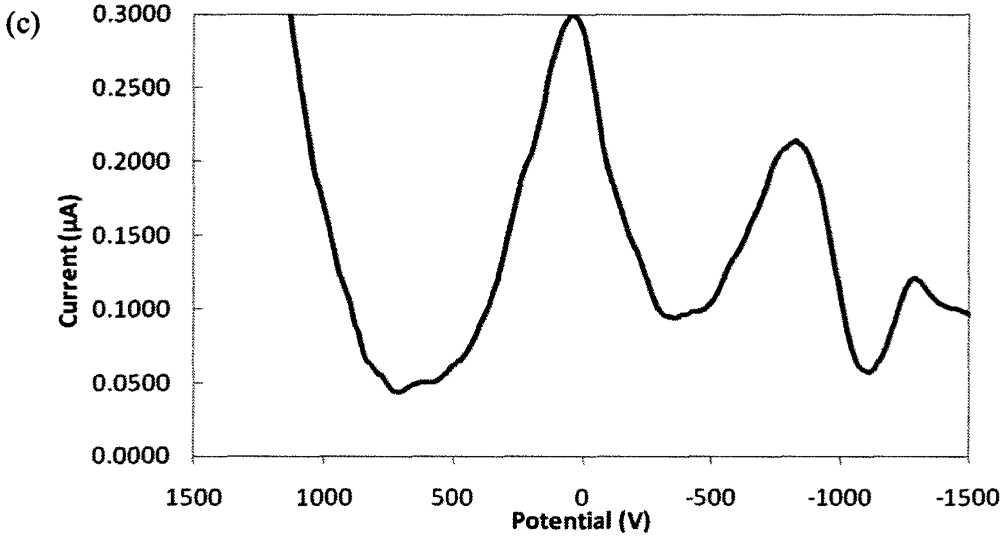

Figure 2.10 DPV spectra of *n*-dodecyl sulfide stablized Ru nanoparticles synthesized at 240°C for (a) 60 minutes, (b) 90 minutes, and (c) 120 minutes.

Table 2.3 Charge transfer of size-controlled Ru nanoparticles

Reaction Time	60 min	90 min	120 min
Diameter (nm) - TEM measurement	2.4	2.7	2.9
ΔV (mV)	528	560	460
HOMO-LUMO gap (mV)	921	870	850
Diameter (nm) – Calculated	1.4	1.4	1.6

3.5 Charging and discharging of Pd and Ru nanoparticles

Irradiation of TiO_2 nanoparticles. TiO_2 is a semiconductor with a band gap of 3.2 eV. In order to separate the electrons from the holes, high energy photons equal to or greater than 3.2 eV are required. In order to avoid electron-hole recombination and to allow electrons to accumulate in the conduction band, a hole scavenger is required. Methanol is a suitable hole scavenger as it reacts readily with the TiO_2 holes and is oxidized to formaldehyde.

Figure 2.11 shows the SEM images of TiO_2 nanoparticles synthesized by the sol-gel method. Electron accumulation in the TiO_2 conduction band is accompanied by blue coloration and an increase in the absorbance intensity in the 400 nm ~ 1000 nm wavelength. Therefore, the blue coloration can be useful in quantitatively measuring the concentration of excited electrons. The absorption spectra of TiO_2 in Figure 2.12 were recorded before and after 30 minutes of irradiation using a xenon lamp. The broad absorption in the range of 400 nm to 900 nm arises when the electrons were stored or trapped in the conduction band of the TiO_2 nanoparticles.

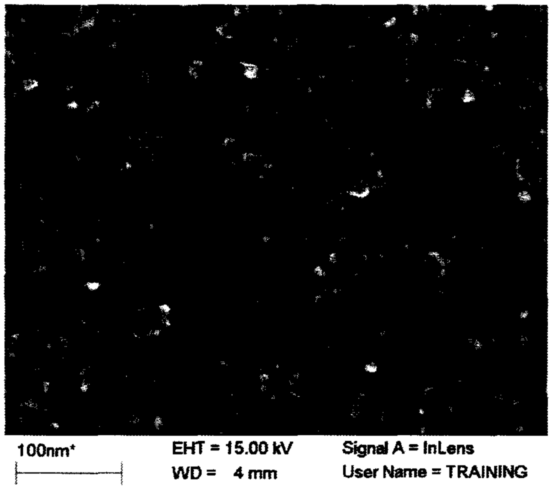

Figure 2.11 The SEM image of TiO_2 nanoparticles in the thin film.

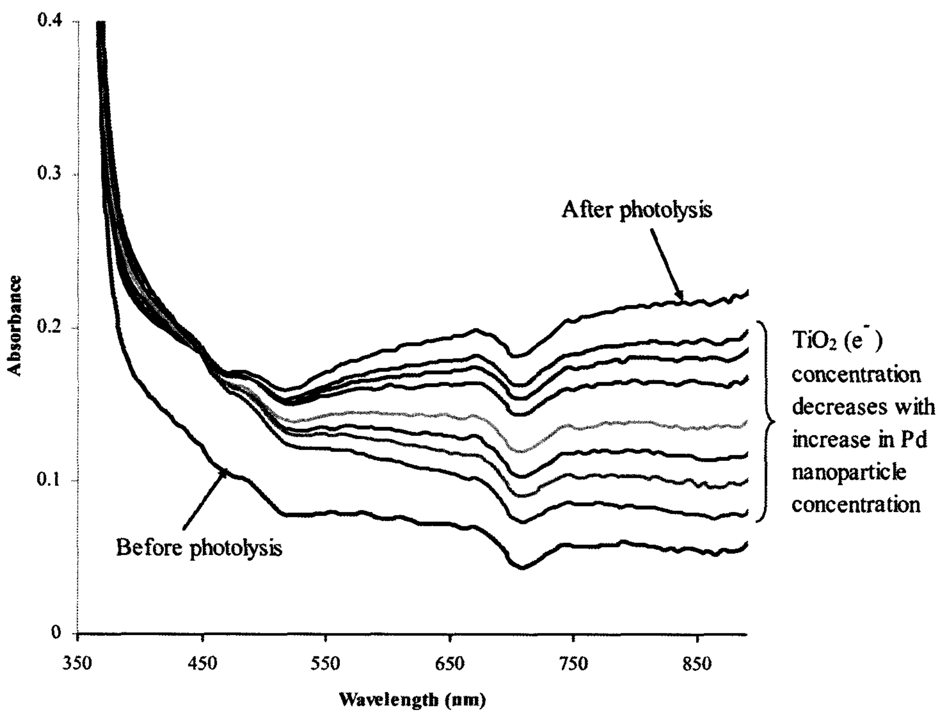

Figure 2.12 Absorption spectra of TiO_2 thin film. The black line was taken before photolysis. The red line was taken after photolysis of TiO_2 nanoparticles. The lines between them were taken when one aliquot Pd nanoparticle solution was added to the system every 10 minutes (from top to bottom: [Pd] = 15, 30, 45, 60, 75, 90 and 105 μM)

3.5.1 Charging and discharging of Pd nanoparticles

Electrons flow to Pd nanoparticles from photoexcited semiconductor. When the metallic nanoparticles were introduced to the solution and contacted with TiO_2 nanoparticles, the electrons transferred from conduction band to metallic nanoparticles, attributed to the lower formal potential of TiO_2 conduction band. The charging process take places during the interaction between TiO_2's electron saturated conduction band and Pd nanoparticles. Since there were no other electron acceptors in the system it could be assumed that the electrons were stored in the Pd nanoparticles.

Discharging of Pd nanoparticles. Iron (III) porphyrin is a well-known redox system with significant potential for several environmental remediation processes. The use of iron porphyrin for catalysis has been adopted in the remediation of toxic organic compounds[36]. We have demonstrated that conduction band electrons can transfer to the Pd nanoparticles. We sought to investigate whether the stored electrons in Pd could discharge and in doing so, could they reduce hemin (Fe^{III}) to heme (Fe^{II}). Hemin exhibits a Soret peak at 405 nm while heme exhibits a Soret band at 420 nm. These characteristics allow easy determination of the oxidation state of the iron compound. When an aliquot of hemin was just injected (time = 0) to a solution of charged Pd nanoparticles, the UV-Vis spectrum exhibited a peak at 405nm which indicates the presence of Fe^{III} (Figure 2.13). During the 30 min equilibrium the absorbance intensity of Fe^{III} decreased and a new peak at 420 nm appeared which indicates reduction to Fe^{II}. We proposed that charged Pd nanoparticles were responsible for the reduction of Fe^{III} to Fe^{II} as illustrated in Scheme 2.1.

3.5.2 Charging and discharging of Ru nanoparticles

Similar to Pd nanoparticles, the Ru nanoparticles could obtain electrons accumulated in the conduction band of TiO_2 nanoparticles (Figure 2.14). However, we found that Fe^{III} porphyrin could not be reduced to Fe^{II} when added to the charged Ru nanoparticles even after 2 days (Figure 2.15). It is reasonable to propose that Ru nanoparticle has poor capability in storing the electron but could quickly shuttle the electrons to the electrolyte (scheme 2.2).

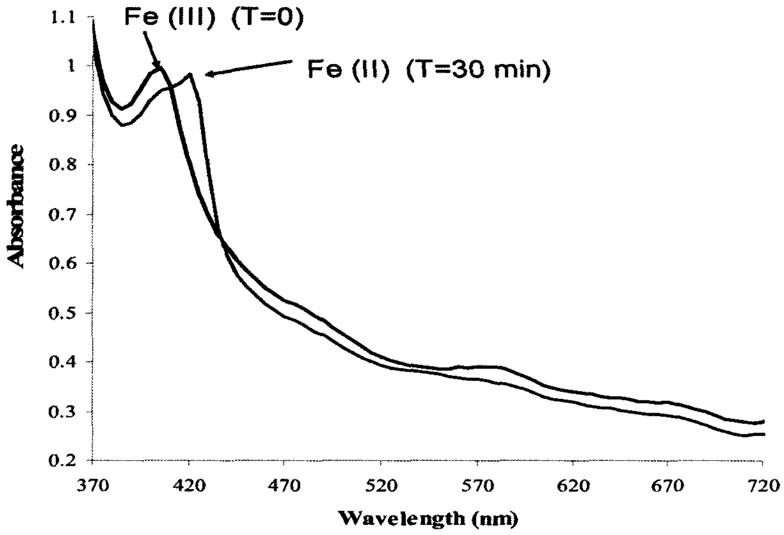

Figure 2.13 Absorption spectra recorded after the deaerated Fe(III) porphyrin (Hemin) methanol was just added to the irradiated TiO_2-Pd nanoparticles system (T=0) and equilibrium for 30 minutes (T=30 min).

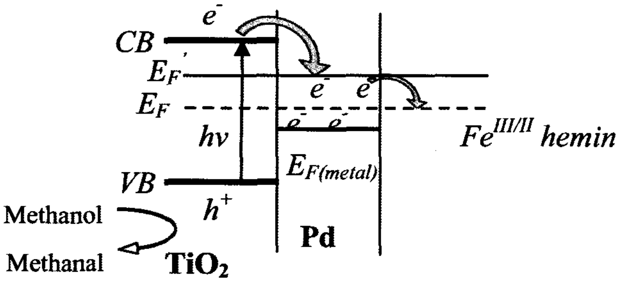

Scheme 2.1 Interfacial energy profile for semiconductor, metallic nanoparticles and hemin interface. E_F refers to the Fermi level of TiO_2 after attaining

equilibrium with hemin. E_F' refers to the Fermi level of TiO_2 after gaining equilibrium with metal nanoparticles and hemin.

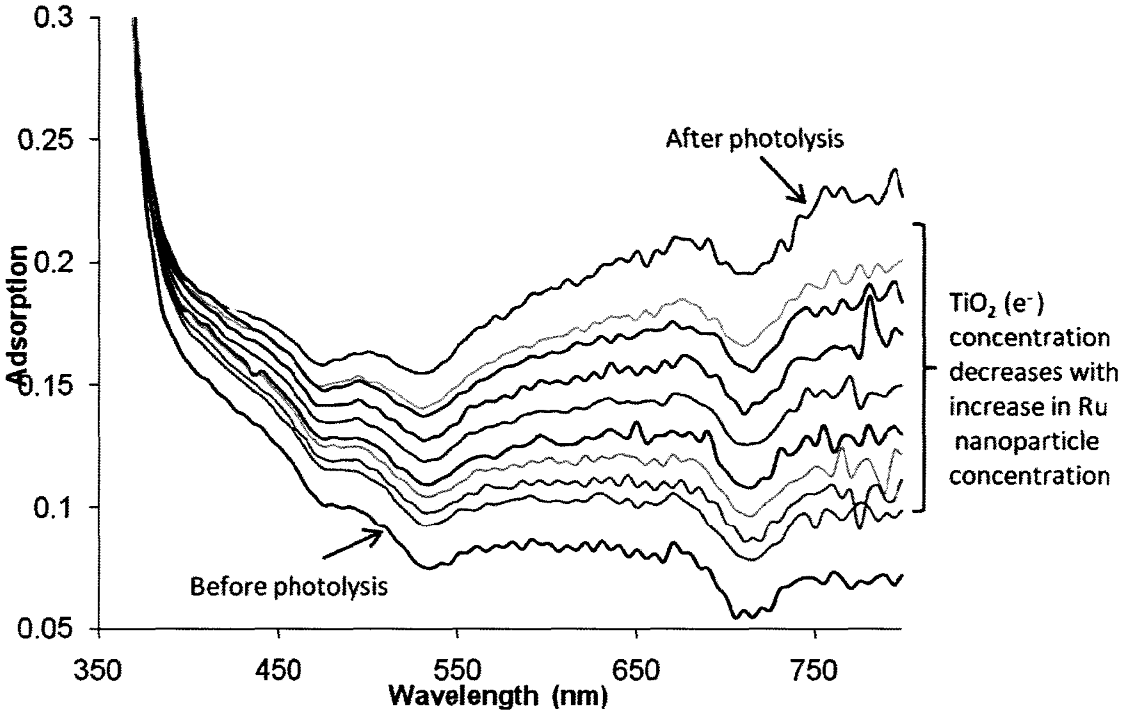

Figure 2.14 Absorption spectra of nanocrystalline TiO_2 films in deaerated methanol. The spectra were taken before illumination, after illumination, and after addition of aliquots of Ru nanoparticles.

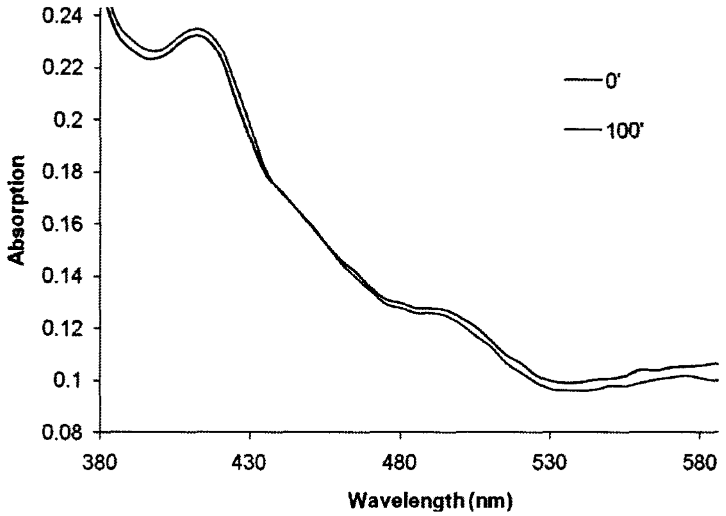

Figure 2.15 Absorption spectra recorded following the addition of Iron(III) porphyrin to the irradiated TiO_2/Ru suspension. The blue line was taken when porphyrin was just added. The red line was taken after 100 minutes equilibration.

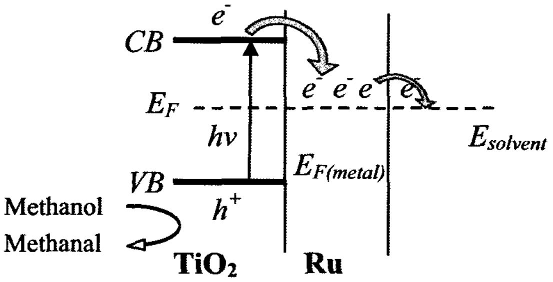

Scheme 2.2 Interfacial energy profile for semiconductor and Ru nanoparticles interface. The rapid electron transfer from Ru to solvent occurs. The Fermi levels of semiconductor and metal remain close to the redox couple in the solution.

4. Conclusion

The production of well-defined, monodisperse small metallic nanoparticles (<3 nm) was achieved by using thioether as reducing agent and stabilizing ligand in a one-step procedure. Because of the uniformity of the nanoparticles we were able to study their electrochemical properties. The capability of double layer charging and discharging within the nanoparticles enables the charge storage and release in a controlled manner.

5. References

1. Bonnemann, H.; Brijoux, W.; Brinkmann, R.; Dinjus, E.; Fretzen, R.; Joussen, T.; Korall, B. In *Highly Dispersed Metal-clusters and Colloids for the Preparation of Active Liquid-phase Hydrogenation Catalysts*, 1992; Elsevier Science Bv: 1992; pp 323-333.

2. Nemamcha, A.; Rehspringer, J. L.; Khatmi, D., Synthesis of palladium nanoparticles by sonochemical reduction of palladium(II) nitrate in aqueous solution. *Journal of Physical Chemistry B* **2006,** 110, (1), 383-387.

3. Okitsu, K.; Mizukoshi, Y.; Bandow, H.; Yamamoto, T. A.; Nagata, Y.; Maeda, Y., Synthesis of palladium nanoparticles with interstitial carbon by sonochemical reduction of tetrachloropalladate(II) in aqueous solution. *Journal of Physical Chemistry B* **1997,** 101, (28), 5470-5472.

4. Platinum Group Metals - the Power to Improve Lives. http://www.ipa-news.com/pgm/index.htm

5. Goddard, W. A.; Brenner, D.; Lyshevski, S. E.; Iafrate, G. J., *Handbook of Nanoscience, Engineering, and Technology, Second Edition* CRC Press 2007.

6. Gogotsi, Y., *Nanomaterials Handbook* CRC Press: 2006.

7. Freemantle, R. G.; Liu, M.; Guo, W.; Obare, S. O., *Approaches to Synthesis and Characterization of Spherical & Anisotropic Palladium Nanomaterials.* Wiley-VCH: 2009.

8. Chen, S. W.; Ingram, R. S.; Hostetler, M. J.; Pietron, J. J.; Murray, R. W.; Schaaff, T. G.; Khoury, J. T.; Alvarez, M. M.; Whetten, R. L., Gold nanoelectrodes of varied size: Transition to molecule-like charging. *Science* **1998,** 280, (5372), 2098-2101.

9. Chen, S. W.; Murray, R. W.; Feldberg, S. W., Quantized capacitance charging of monolayer-protected Au clusters. *Journal of Physical Chemistry B* **1998,** 102, (49), 9898-9907.

10. Hicks, J. F.; Templeton, A. C.; Chen, S. W.; Sheran, K. M.; Jasti, R.; Murray, R. W.; Debord, J.; Schaaf, T. G.; Whetten, R. L., The monolayer thickness

dependence of quantized double-layer capacitances of monolayer-protected gold clusters. *Analytical Chemistry* **1999,** 71, (17), 3703-3711.

11. Green, S. J.; Stokes, J. J.; Hostetler, M. J.; Pietron, J.; Murray, R. W., Three-dimensional monolayers: Nanometer-sized electrodes of alkanethiolate-stabilized gold cluster molecules. *Journal of Physical Chemistry B* **1997,** 101, (14), 2663-2668.

12. Ingram, R. S.; Hostetler, M. J.; Murray, R. W., Poly-hetero-omega-functionalized alkanethiolate-stabilized gold cluster compounds. *Journal of the American Chemical Society* **1997,** 119, (39), 9175-9178.

13. Ingram, R. S.; Hostetler, M. J.; Murray, R. W.; Schaaff, T. G.; Khoury, J. T.; Whetten, R. L.; Bigioni, T. P.; Guthrie, D. K.; First, P. N., 28 kDa alkanethiolate-protected Au clusters give analogous solution electrochemistry and STM Coulomb staircases. *Journal of the American Chemical Society* **1997,** 119, (39), 9279-9280.

14. Ingram, R. S.; Murray, R. W., Electroactive three-dimensional monolayers: Anthraquinone omega-functionalized alkanethiolate-stabilized gold clusters. *Langmuir* **1998,** 14, (15), 4115-4121.

15. Brousseau, L. C.; Zhao, Q.; Shultz, D. A.; Feldheim, D. L., pH-gated single-electron tunneling in chemically modified gold nanoclusters. *Journal of the American Chemical Society* **1998,** 120, (30), 7645-7646.

16. Jakob, M.; Levanon, H.; Kamat, P. V., Charge distribution between UV-irradiated TiO_2 and gold nanoparticles: Determination of shift in the Fermi level. *Nano Letters* **2003,** 3, (3), 353-358.

17. Wood, A.; Giersig, M.; Mulvaney, P., Fermi level equilibration in quantum dot-metal nanojunctions. *Journal of Physical Chemistry B* **2001,** 105, (37), 8810-8815.

18. Kim, J.; Lee, D., Size-controlled interparticle charge transfer between TiO2 and quantized capacitors. *Journal of the American Chemical Society* **2007,** 129, (25), 7706.

19. Valden, M.; Lai, X.; Goodman, D. W., Onset of catalytic activity of gold clusters on titania with the appearance of nonmetallic properties. *Science* **1998,** 281, (5383), 1647-1650.

20. Subramanian, V.; Wolf, E.; Kamat, P. V., Semiconductor-metal composite nanostructures. To what extent do metal nanoparticles improve the photocatalytic activity of TiO2 films? *Journal of Physical Chemistry B* **2001,** 105, (46), 11439-11446.

21. Heimer, T. A.; Darcangelis, S. T.; Farzad, F.; Stipkala, J. M.; Meyer, G. J., An acetylacetonate-based semiconductor-sensitizer linkage. *Inorganic Chemistry* **1996,** 35, (18), 5319-5324.

22. Obare, S. O.; Ito, T.; Meyer, G. J., Controlling reduction potentials of semiconductor-supported molecular catalysts for environment remediation of organohalide pollutants. *Environmental Science & Technology* **2005,** 39, (16), 6266-6272.

23. Love, J. C.; Estroff, L. A.; Kriebel, J. K.; Nuzzo, R. G.; Whitesides, G. M., Self-assembled monolayers of thiolates on metals as a form of nanotechnology. *Chemical Reviews* **2005,** 105, (4), 1103-1169.

24. Ganesan, M.; Freemantle, R. G.; Obare, S. O., Monodisperse thioether-stabilized palladium nanoparticles: Synthesis, characterization, and reactivity. *Chemistry of Materials* **2007,** 19, (14), 3464-3471.

25. Ho, P. F.; Chi, K. M., Size-controlled synthesis of Pd nanoparticles from beta-diketonato complexes of palladium. *Nanotechnology* **2004,** 15, (8), 1059-1064.

26. Wagner, C. D.; Riggs, W. M.; Davis, L. E.; Moulder, J. F.; Muilenberg, B. E., *Handbook of XRay Photoelectron Spectroscopy*. Perkin Elmer, Physical Electronics Division: Eden Prairie, 1979.

27. Piao, Y. Z.; Jang, Y. J.; Shokouhimehr, M.; Lee, I. S.; Hyeon, T., Facile aqueous-phase synthesis of uniform palladium nanoparticles of various shapes and sizes. *Small* **2007,** 3, (2), 255-260.

28. Semagina, N.; Renken, A.; Laub, D.; Kiwi-Minsker, L., Synthesis of monodispersed palladium nanoparticles to study structure sensitivity of solvent-free selective hydrogenation of 2-methyl-3-butyn-2-ol. *Journal of Catalysis* **2007,** 246, (2), 308-314.

29. Zamborini, F. P.; Gross, S. M.; Murray, R. W., Synthesis, characterization, reactivity, and electrochemistry of palladium monolayer protected clusters. *Langmuir* **2001,** 17, (2), 481-488.

30. Chen, S. W.; Huang, K.; Stearns, J. A., Alkanethiolate-protected palladium nanoparticles. *Chemistry of Materials* **2000,** 12, (2), 540-547.

31. Gu, Y. L.; Xie, H.; Gao, J. X.; Liu, D. X.; Williams, C. T.; Murphy, C. J.; Ploehn, H. J., AFM characterization of dendrimer-stabilized platinum nanoparticles. *Langmuir* **2005,** 21, (7), 3122-3131.

32. Kim, Y. G.; Garcia-Martinez, J. C.; Crooks, R. M., Electrochemical properties of monolayer-protected Au and Pd nanoparticles extracted from within dendrimer templates. *Langmuir* **2005,** 21, (12), 5485-5491.

33. Tu, W. X.; Liu, H. F., Rapid synthesis of nanoscale colloidal metal clusters by microwave irradiation. *Journal of Materials Chemistry* **2000,** 10, (9), 2207-2211.

34. McClune, W. F., *Powder Diffraction File Alphabetical Index Inorganic Phase.* Joint Committee on Powder Diffraction Standards (JCPDS): Swarthmore, PA, 1980.

35. Chen, W.; Davies, J. R.; Ghosh, D.; Tong, M. C.; Konopelski, J. P.; Chen, S. W., Carbene-functionalized ruthenium nanoparticles. *Chemistry of Materials* **2006,** 18, (22), 5253-5259.

36. Hendrickson, D. N.; Kinnaird, M. G.; Suslick, K. S., Photochemistry of (5,10,15,20-tetraphenylporphyrinato) iron (III) halide - complexes, Fe(TTP) (X). *Journal of the American Chemical Society* **1987,** 109, (4), 1243-1244.

CHAPTER III

SYNTHESIS, CHARACTERIZATION AND ELECTROCHEMISTRY OF PALLADIUM-RUTHENIUM BIMETALLIC NANOPARTICLES

1. Introduction

The ability to control the morphology of metallic and bimetallic nanoparticles continues to be a challenging and significant area of research in nanoscale science. Developing systematic synthetic approaches that provide uniform particles allows the investigation of size-dependent chemical and physical properties. Straightforward synthetic procedures that produce catalytic bimetallic nanoparticles in high yield and with narrow size distributions are in much demand for both fundamental studies as well as practical applications. Bimetallic nanoparticles have shown several advantages and unique properties relative to their single metal counterparts[1-9]. Palladium and ruthenium are both excellent catalysts for several organic transformations. Alloys containing palladium or ruthenium have shown catalytic activity toward hydrogenation[10, 11], dehydrogenation[12], carbon-carbon coupling reactions[13-15], fuel cells[16, 17], and oxygen reduction reactions[18]. But the effect of each metal relative to the other on the overall properties of the alloy is still not completely understood.

There are a few reports that describe the synthesis of bimetallic Pd-Ru nanoparticles with well-defined morphology ("Well defined" means size distribution having standard deviations of ±0.3 nm and particle-to-particle elemental compositional variations of ±7%)[19, 20]. These methods include the core metal galvanic exchange reaction[21], thermal decomposition[22], laser-induced melting, ultrasonic synthesis, extracellular biosynthesis, photochemical reduction, dendrimer template synthesis[10, 12], etc. Bimetallic nanoparticles adopt either an alloy morphology or they could be layered or core-shell in structure. The resulting morphology depends on the synthesis procedure used and the control over the nucleation and growth processes.

Developing synthetic strategies that allow easy access to monodisperse bimetallic nanoparticles is therefore in high demand. Our laboratory has shown that thioether-based ligands are excellent stabilizers and result in monodisperse nanoparticles with controllable size[23]. Here, we report a new one-step approach for the synthesis of bimetallic palladium-ruthenium (Pd-Ru) alloy nanoparticles. Pd-Ru nanoparticles with a narrow size distribution were synthesized by the simultaneous reduction of two metal salts in an organic solution and stabilized by thioether ligands. The synthesis of these nanoparticles was accomplished by careful control of the reaction temperature, time and reactant concentrations. Characterization and the unique electrochemical properties of Pd-Ru bimetallic alloy nanoparticles were investigated.

2. Experimental details

Materials. Palladium acetate [$Pd_3(OAc)_6$], triruthenium dodecacarbonyl [$Ru_3(CO)_{12}$] and ruthenium (III) acetylacetonate $Ru[(CH_3CO)_2CH_3]_3$ were obtained from Strem Chemicals. TiO_2 nanopowder was purchased from VWR. Methyl viologen was purchased from Frontier Scientific Inc. *n*-Dodecyl sulfide (93%) and all solvents including dry toluene, nitrobenzene, hexane, dichloromethane (DCM) and ethanol were procured from Sigma Aldrich Chemicals. A custom-designed quartz cuvette with a 1 cm path length was used for optical spectrometry. All glassware and teflon coated stir bars were cleaned with aqua regia, thoroughly washed with DI water and acetone, and dried in an oven before use.

2.1 Synthesis of Pd-Ru bimetallic nanoparticles

Synthesis of Pd-Ru bimetallic nanoparticles. Triruthenium dodecacarbonyl (0.08 g, 1.25×10^{-4} mol) was mildly heated in 30 mL of toluene. Next, palladium (II) acetate (0.084 g, 1.25×10^{-4} mol) and *n*-dodecyl sulfide ($[CH_3(CH_2)_{11}]_2S$) (1.38 g, 37.5×10^{-4} mol) [mole ratio of Ru^{3+}:Pd^{2+}:ligand is 1:1:10] were added to the solution. The solution was degassed for 15 minutes, followed by the introduction of nitrogen gas. The solution was stirred and heated from room temperature to 110°C for designated periods of time during which the solution gradually changed color from bright red to dark brown. After the prescribed period of time, the dark colloid was removed from the heating source and allowed to cool under nitrogen for 24 hours with continued stirring. The particles were then precipitated using an equivolume quantity of dry methanol, followed by centrifugation at 15K rpm for 2 minutes. The black pellet was then washed with methanol and redispersed in a solution of dichloromethane to give a brown colloidal solution.

An alternative method for making bimetallic Pd-Ru nanoparticles was achieved by adding 0.084 g (1.25×10^{-4} mol) of palladium (II) acetate, 0.124 g (3.75×10^{-4} mol) of ruthenium (III) acetylacetonate and 1.38 g (37.5×10^{-4} mol) of *n*-

dodecyl sulfide [mole ratio of Ru^{3+}:Pd^{2+}:ligand is 1:1:10], respectively to 30 mL of dry toluene in a 250 mL round bottom flask. The flask was connected to a Schlenk line which was connected to nitrogen and continuously stirred with reactions carried out at 240°C for time intervals ranging from 30 minutes to 3 hours. The final product was allowed to cool down under a nitrogen environment for 24 hours with continued stirring.

2.2 Characterization of Ru-Pd bimetallic nanoparticles

High Resolution Transmission Electron Microscopy (HRTEM) and Selective Area Electron Diffraction (SAED). HRTEM imaging was carried out at the Center for Advanced Microscopy at Michigan State University. A JEM-2200FS with a field emission gun was used and operated at 200 kV. The microscope was fitted with an ultra-high-resolution (UHR) pole piece with the point resolution of 0.19 nm and high angle dark field STEM resolution of 0.13 nm. The analytical work was done with the attached Oxford INCA system with energy resolution of 140 eV. The images were collected with a Gatan Multiscan camera which has a 1024 × 1024 resolution.

Powder X-ray Diffraction (XRD). The crystalline structure of Pd-Ru nanoparticles were determined by powder X-ray analysis. X-ray diffraction patterns were collected on a PANalytical X'Pert Pro MPD in the Bragg-Brentano geometry. The instrument was calibrated with a packed LaB6 powder in a 0.3 mm diameter X-ray capillary tube before sample runs. The sample was scanned in a symmetric mode with a step size of 0.05° at 300 s/step. The scan range at 2θ was 30-90°. The x-ray radiation was a Cu $K\alpha_1$, $\lambda = 1.5406$ Å. Phase analysis was performed using the X'Pert

High Score Plus with MDI JADE software and the ICDD PDF-2 release 2006 database.

To prepare samples for X-ray diffraction, the as-prepared Pd-Ru nanoparticles were suspended in methanol to help precipitate the nanoparticles during centrifugation. The collected nanoparticles were washed with methanol several times before drying in a vacuum oven overnight. The dried powders were packed in a thin-walled glass capillary tube for analysis.

X-ray Photoelectron Spectroscopy (XPS). XPS measurements were acquired using a Perkin Elmer Phi 5400 ESCA system with a magnesium Kα x-ray source. Samples were analyzed at pressures between 10^{-9} and 10^{-8} torr with a pass-energy of 29.35 eV and a take-off angle of 45°. The spot size was approximately 250 μm^2. Atomic concentrations were determined using previously determined sensitivity factors. All peaks were referenced to the signature C 1*s* peak for carbon at 284.6 eV.

Ultra-high vacuum XPS of the samples were recorded on a VG Microtech-ESCA 3000 spectrometer, in vacuum at a pressure of 10^{-10} torr, pass energy of 50 eV and using un-monochromatized Mg–K as the radiation source (photon energy of 1253.6 eV). Surface analyses by XPS spectra was carried out quantitatively in terms of the binding energy (B. E.) values of various elements present on the catalyst support after necessary C 1*s* correction, especially taking into consideration the Pd and Ru $3d_{5/2}$ and $3d_{3/2}$ B. E. values.

2.3 Differential Pulse Voltammetry (DPV) measurements of Pd-Ru bimetallic nanoparticles

Electrochemical measurements were acquired using a BASi Epsilon potentiostat. To a deareated 1:1 (v/v) toluene/CH_2Cl_2 solution, 0.1 M of the electrolyte tetra-*n*-butylammonium hexafluorophosphate ($TBAPF_6$) was added. DPV measurements were carried out using two Pt wires (0.4 mm in diameter, area of 0.001 cm^2) as the working and counter electrodes, respectively, and using Ag wire (0.5 mm in diameter) as a quasi-reference electrode. Prior to use, the working electrode was polished with 0.05 μm Al_2O_3 slurries and rinsed thoroughly with copious acetone. Then, it was dried using a steam of N_2 gas or compressed air. The cell was purged with N_2 gas for at least 20 minutes before measurements were taken.

The scan rate was set at 20 mV/sec, the pulse amplitude was 50 mV, the sample width was 17 ms, the pulse width was 50 ms, and the pulse period was 200 ms. The scan range was -1500 mV to 1500 mV. A background scan was conducted in 1:1 (v/v) CH_2Cl_2/diphenyl ether (or toluene).

2.4 Charging and discharging study of Pd-Ru bimetallic nanoparticles

Irradiation of TiO_2 colloidal. The TiO_2 nanopowder (size range from 10 nm to 100 nm) was suspended in methanol solution in a quartz cuvette by sonication for at least 10 minutes, forming a stable milky white solution. The cuvette was sealed with a rubber septum and then purged with N_2 gas for at least 20 minutes before irradiation. A Model 6271 ozone-free Xenon lamp (Newport) was used as the irradiation source. The quartz cuvette containing TiO_2-suspended methanol was irradiated for 5 minutes and resulted in a blue suspension.

Charge transfer from TiO_2 to Pd-Ru nanoparticles. Pd-Ru alloy nanoparticles were injected to the cuvette containing TiO_2 in methanol solution. Injection was carried out using an air-tight syringe.

Discharging of Pd-Ru alloy nanoparticles to methyl viologen. A deaerated methyl viologen (1,1'-dimethyl-4,4'-bipyridinium) methanol solution was added to the above cuvette (charged nanoparticles solution) using an air-tight syringe.

3. Results and discussion

3.1 Characterization of Pd-Ru bimetallic nanoparticles

The formation of nanoscale particles from metallic precursors includes reduction/nucleation and growth/stabilization processes, which provides means for controlling the nanoparticle size. Particle growth dynamics are due to the combined consequence of two competing processes, nucleation of zero-valent metal atoms forming particle cores (cluster cores) and passivation of the clusters by surface-protecting ligands (Scheme 3.1)[24]. At activation temperature (240°C for both Pd and Ru precursor), Obare has reported the profound influence of concentration, temperature and reaction time to particles size as well as size distribution[23]. We demonstrated that at 240°C, particle size increased with increasing reaction time (Figure 3.1). The data reveals that particle growth is dominant during the first 90 minutes. This is consistent with Ostwald Ripening[25], where energetic factors cause large particles to grow by drawing atoms from smaller particles because surface molecules are energetically less stable. The particles size levels off after 90 minutes due to the depletion of smaller particles as well as any free metal atoms that may be present in solution.

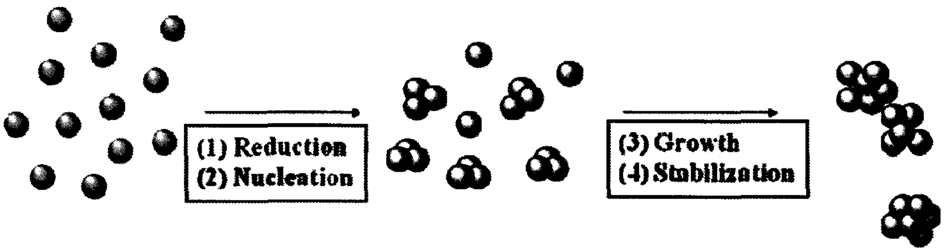

Scheme 3.1 Particle growth dynamics of metallic nanoparticles. The reduction of Pd and Ru precursors by thioether prepared metal atoms for nuclei formation. The particles grow bigger as large particles draw atoms from smaller particles or small particles coagulate to form bigger particles. Ligands stabilize particles from aggregation to form big particles at the end of reaction.

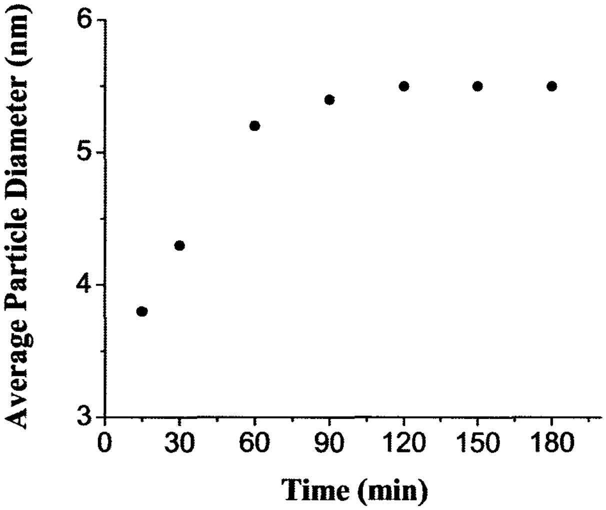

Figure 3.1 Reaction kinetics of Pd-Ru bimetallic nanoparticles. Particle sizes were plotted with respect to the reaction time at 240°C. Particles continue to grow up to 2 hours, but after 2 hours no further growth occurs.

The transmission electron microscopy (TEM) image in Figure 3.2 shows that the particles produced had a narrow size distribution with an average of 4.3 ± 0.5 nm in diameter when the reaction was carried out at 240°C for 30 min. The high-resolution TEM image shown in Figure 3.3a reveals that the bimetallic nanoparticles have crystal fringes with two lattice spacings of 2.68Å and 2.59Å. The angle is 130°. Under a high beam of energy, during TEM analysis, the particles would melt and form irregular shapes. Combined cubic close-packed Pd and hexagonal close-packed Ru characteristics are reflected in the selected area electron diffraction (SAED) rings (Figure 3.3b) and x-ray diffraction (XRD) pattern (Figure 3.4). Lattice fringes of (111), (200), (220), (311), (222) correspond to Pd and (100), (101), (102) to Ru. Table 3.1 gives the four main peak parameters, i.e., the peak position in degrees (°), the *d*-spacing in Å, the peak heights, the peak area, the relative peak area, the peak resolution (FWHM), and the crystalline size (in nm) calculated using the Scherrer formula.

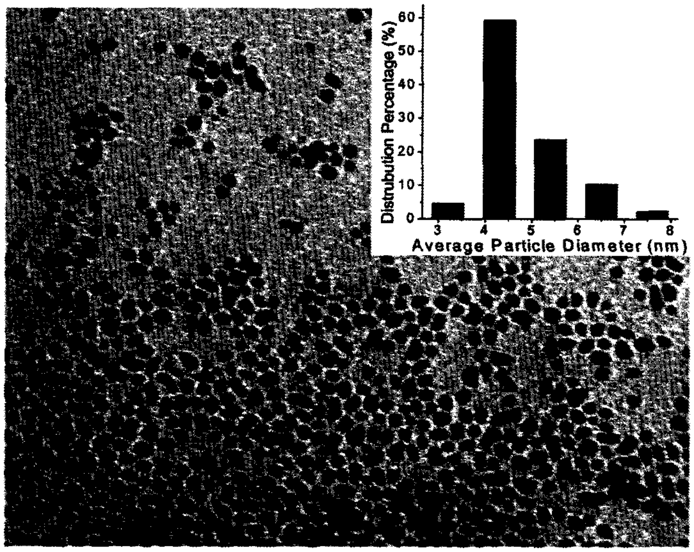

Figure 3.2 TEM image of 4.3 nm Pd-Ru alloy bimetallic nanoparticles. The inset is a histogram of the particles counted vs. the average particle diameters.

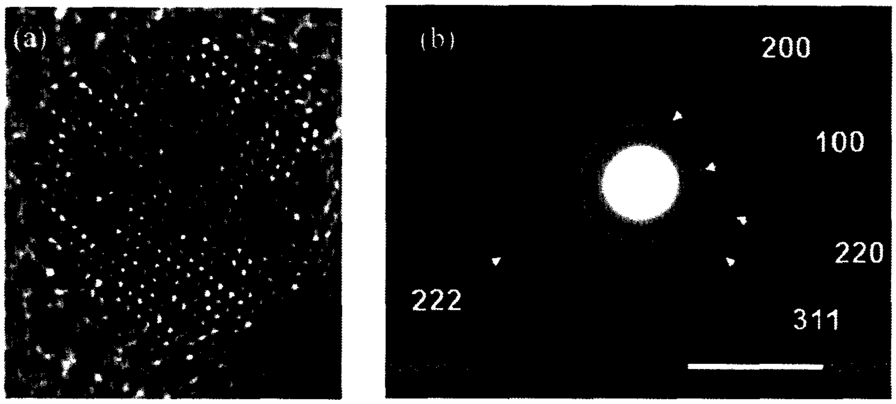

Figure 3.3 (a) HR -TEM image and (b) SAED pattern of 4.3 nm Pd-Ru alloy bimetallic nanoparticles.

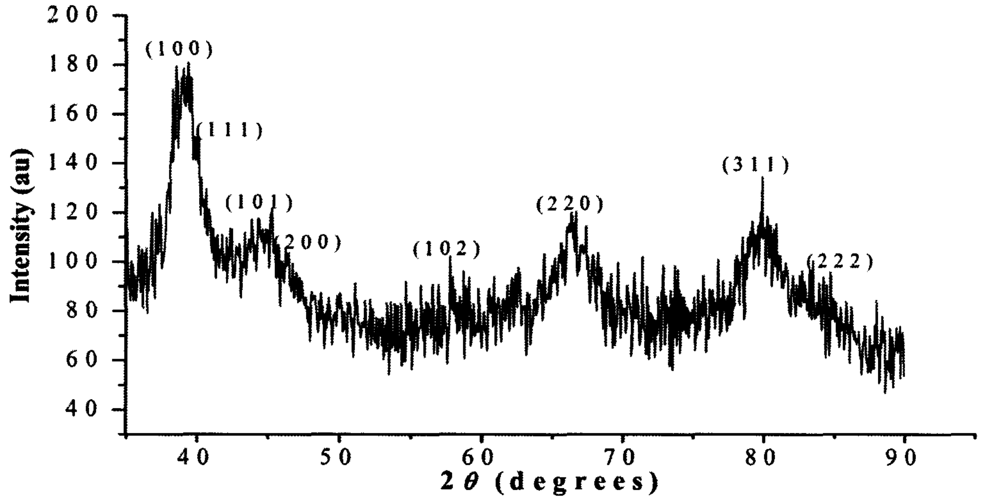

Figure 3.4 Powder XRD pattern of 4.3 nm Pd-Ru alloy bimetallic nanoparticles.

Table 3.1 Parameters of the four main peaks in Figure 3.4 XRD spectrum.

2-Theta	**d(Å)**	**Height**	**Area**	**Area%**	**FWHM**	**XS(nm)**
38.967 (0.077)	2.3095 (0.0088)	86 (6)	4754 (376)	100.0	2.286 (0.144)	3 (1)
44.778 (0.331)	2.0223 (0.0284)	31 (3)	3146 (423)	66.2	4.220 (0.575)	2 (1)
66.509 (0.230)	1.4047 (0.0086)	35 (2)	2450 (270)	51.5	3.336 (0.318)	2 (1)
79.545 (0.189)	1.2041 (0.0048)	36 (2)	2850 (386)	59.9	3.303 (0.483)	3 (2)

*Values in parentheses correspond to the estimated standard deviation (esd).

Both Pd and Ru transition metals are highly vulnerable to oxidation and therefore it is important to fully characterize their oxidation states. Surface techniques such as XPS provide information on atomic composition and the binding energies of inner shell electrons of both the metal and the ligand on the surface of the bimetallic nanoparticles. Tabuani and co-workers conducted an experiment in which they monitored the reduction of Pd^{2+} to Pd^0 by XPS, and observed a progressive transition of Pd^{2+} (337.5 and 342.8 eV) to Pd^0 (338.0 and 341.3 eV)[26]. The ligand surrounding the Pd nanostructures influences the Pd oxidation state. For example, Lu *et al.* revealed that the main component of Pd in thiol-stabilized Pd nanoparticles (either crystalline or amorphous phase) was Pd^0, which they were able to determine based on the Pd *3d* signal of 337.3 eV and S 2*p* signal of 162.3 eV[27].

In the acquired XPS spectra (Figure 3.5) for our Pd-Ru bimetallic nanoparticles, the Ru(3*d*) peaks overlap with the C(1*s*) signal, therefore additional scanning was performed in the 277 eV to 292 eV region (Figure 3.5b). Deconvolution revealed that the signal within this region was the superimposition of C, RuO_3, and Ru^0. The main portion of the signal was contributed by C1*s* arising from the stabilizing ligand. Peaks of 282.84 eV and 287.01 eV indicate Ru^{6+} (3*d*), and peaks of 280.69 eV and 284.86 eV indicated Ru^0. The area ratio of these two groups indicates the ratio of the compositions which was found to be 1:3 of Ru^{6+}:Ru^0. Similarly, the Pd (3*d*) region (from 333 eV to 347 eV) was repeatedly scanned and magnified (Figure 3.5c) to determine the Pd composition. Pd^0 peaks located at 335.79 eV and 341.01 eV, and PdO_2 peaks located at 337.76 eV and 343.03 eV were observed. The content of Pd^0 was found to be 10 times more than that of Pd^{4+}. Therefore, it could be concluded that Pd-Ru nanoparticle synthesized by the simultaneous reduction of Pd and Ru precursors contains both metals as an alloy in mostly the zerovalent state. Oxidized state Pd^{4+} and Ru^{6+} formed small portion of the surface atoms. Both XPS and energy dispersive x-ray analysis (EDX) data (Figure 3.6) indicated that the two metals exist at nearly 1:1 stoichiometric. A XPS peak found at 154 eV suggests the presence of oxidized sulfur species (e.g., disulfides, sulfinates, and sulfonates) on Pd-Ru nanoparticles, which is due to the stabilizer and its byproducts[21].

3.2 Electrochemistry of bimetallic nanoparticles

DPV is a sensitive electrochemical measurement for low concentrated ligand stabilized nanoparticles solution, providing information not only the single electron transfer from the metal core to ligands, but also size and disperity of nanoparticles. Consecutive charging steps should occur at regular spacing

$$\Delta V = \frac{e}{C}$$

where C is the capacitance of particle, e is the electronic charge. Quantized electron transfer in single nanoparticles has been intensively studied by R.W. Murray and S.W. Chen, [28] but that of bimetallic alloy nanoparticles has not been reported.

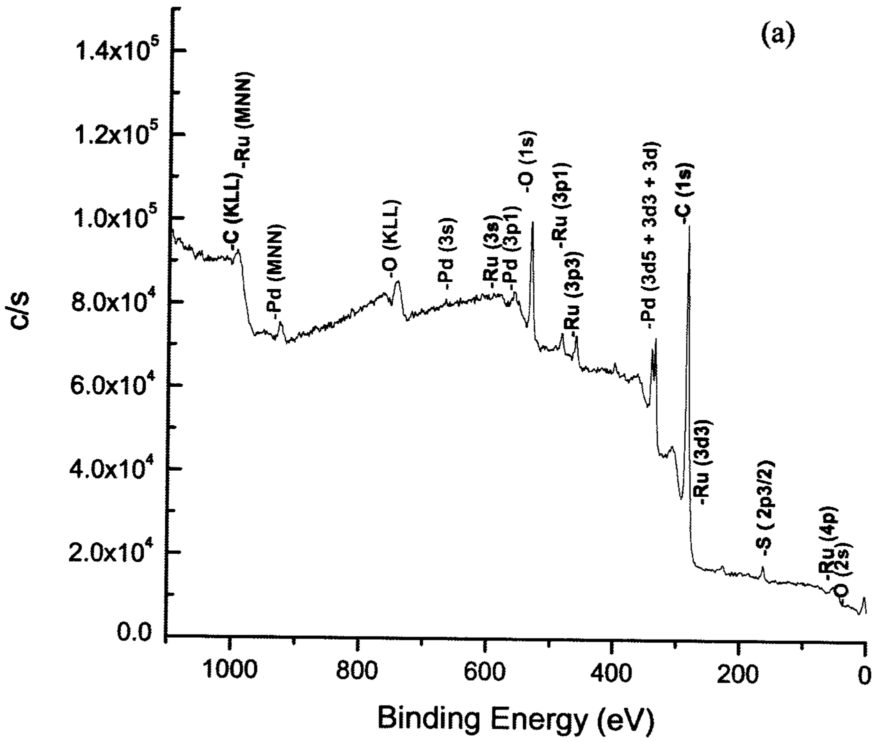
(a)
1.4x10^5
1.2x10^5
1.0x10^5
8.0x10^4
6.0x10^4
4.0x10^4
2.0x10^4
0.0
c/s
1000
800
600
400
200
0
Binding Energy (eV)
-C (KLL)
-Ru (MNN)
-Pd (MNN)
-O (KLL)
-Pd (3s)
-Ru (3s)
-Pd (3p1)
-O (1s)
-Ru (3p1)
-Ru (3p3)
-Pd (3d5 + 3d3 + 3d)
-C (1s)
-Ru (3d3)
-S (2p3/2)
-Ru (4p)
-O (2s)

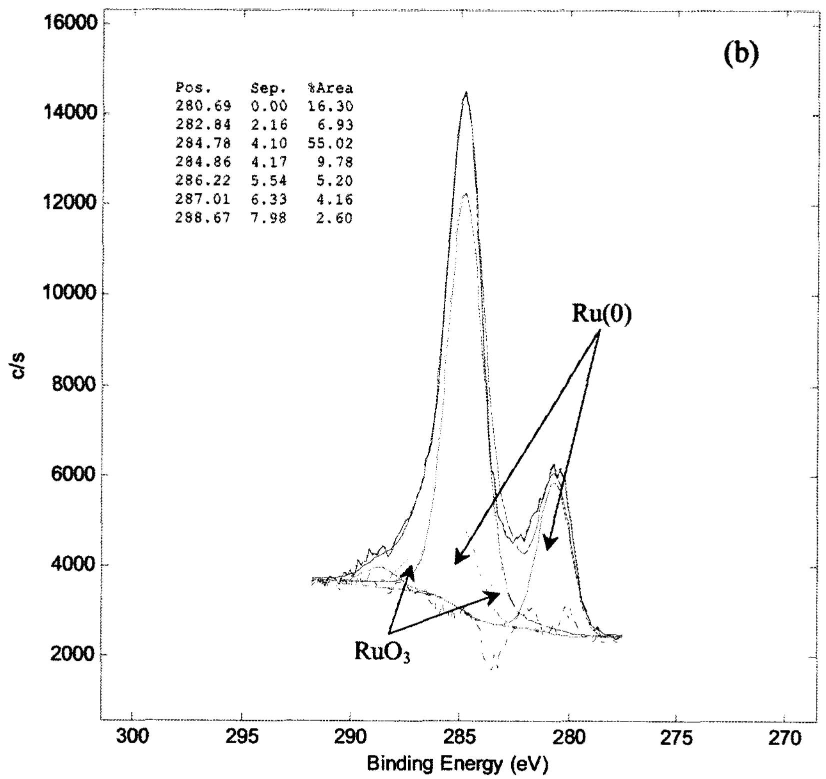

Pos.	Sep.	%Area
280.69	0.00	16.30
282.84	2.16	6.93
284.78	4.10	55.02
284.86	4.17	9.78
286.22	5.54	5.20
287.01	6.33	4.16
288.67	7.98	2.60

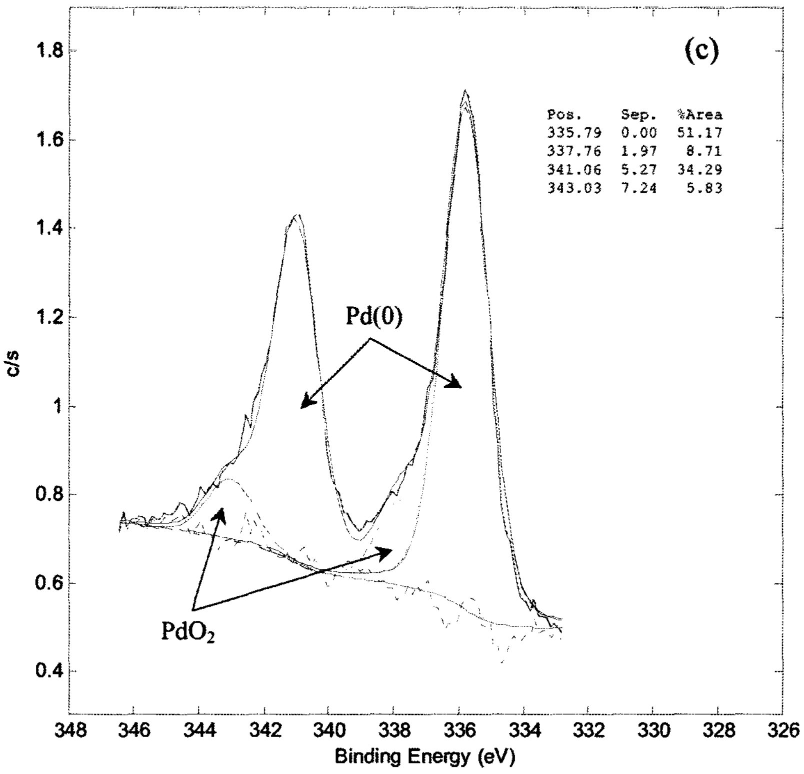

Figure 3.5 XPS pattern of Pd-Ru bimetallic nanoparticle in (a) full scale, (b) C1*s* region, and (c) Pd3*d* region. To fit the Ru 3d line which is covered by C1*s*, Ru(0) and RuO_3 peaks were applied. To fit the Pd 3*d* line, Pd(0) and PdO_2 peaks were applied.

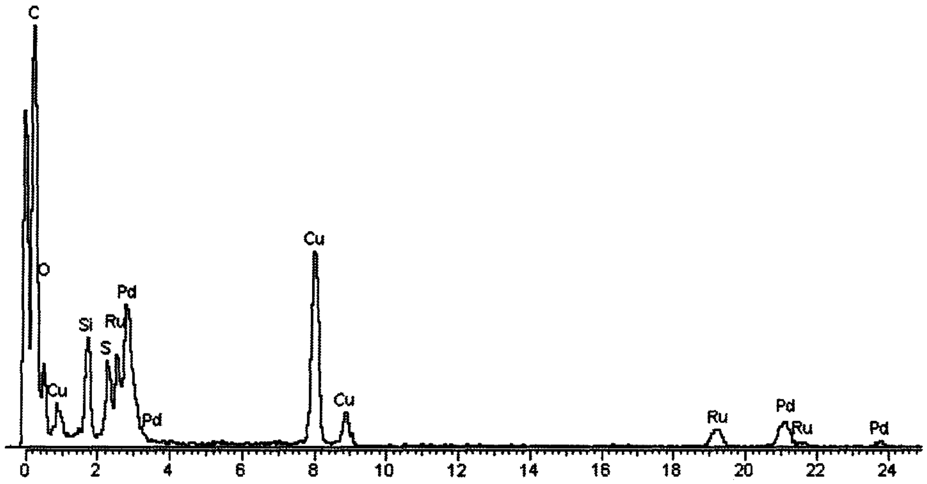

Figure 3.6 EDX spectrum of Pd-Ru alloy bimetallic nanoparticles.

The ability to control the size of these nanoparticles with diameters less than 5 nm further provided the ability to study their electrochemical properties. Notable work[29] done by R.W. Murray showed that metallic nanoclusters consisting of a few hundred atoms or less exhibited molecule-like quantized double-layer (QDL) charging capacitance. The concentric sphere capacitance model was found to correlate well with diameters less than 3 nm. Nanoparticles with diameters larger than 4 nm did not show distinct redox peaks and did not exhibit molecule-like behavior for metallic nanoparticles (Figure 3.7).

Surprisingly, for Pd-Ru alloy nanoparticles, QDL charge transfer was observed in nanoparticles with diameters as large as 4.3 nm (Figure 3.8). Furthermore, the size of the Pd-Ru bimetallic nanoparticles calculated using the concentric sphere capacitance model was found to be 1.8 nm, whereas TEM imaging showed that the particles were 4.3 nm in diameter. Thus, the calculated size obtained from the measured ΔV value of 370 mV is much smaller than the measurement obtained by TEM imaging. The discrepancy in the two values is 55%. Previous studies on Au nanoparticles reported by others showed that the particles size calculated by TEM measurements was in close proximity to the value obtained using the concentric sphere capacitance model[30-33]. In one specific case, reported by Crooks, an 11% discrepancy in the TEM measurement relative to the concentric sphere capacitance model measurement for Pd nanoparticles was attributed the poor imaging contrast by TEM for small particles[34]. It is not applicable in our case since our Pd-Ru bimetallic nanoparticles have large diameters of 4.3 nm. Their unordinary QDL charging behavior can be attributed to the interaction of the two metals in close proximity to each other that lead to quantized double-layer charging. Such an observation opens new opportunities for exploring the novel properties of bimetallic materials with nanoscale dimensions.

Figure 3.9 shows the DPV spectra of five nanoparticle samples with different sizes. The size was controlled through controlling the reaction time as illustrated in Figure 3.1. Their sizes were measured using their TEM images. The DPV of 5.3 nm particles (produced during a one hour reaction) displayed one reduction and one oxidation peak both centered at -1.0V. Polydispersity in the early stage of particle growth may contribute to this result. Longer reaction times (1.5 hours to 3 hours) resulted in nanoparticles of 5.4 nm and 5.5 nm which show additional DPV peaks, indicating the particles had narrow size distributions. The positions (reduction potentials) of the peaks are listed in Table 3.2.

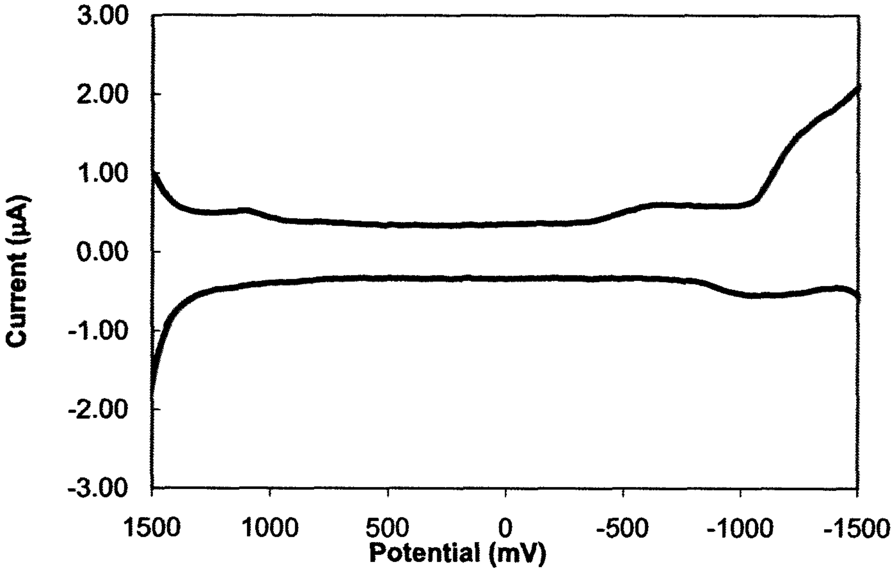

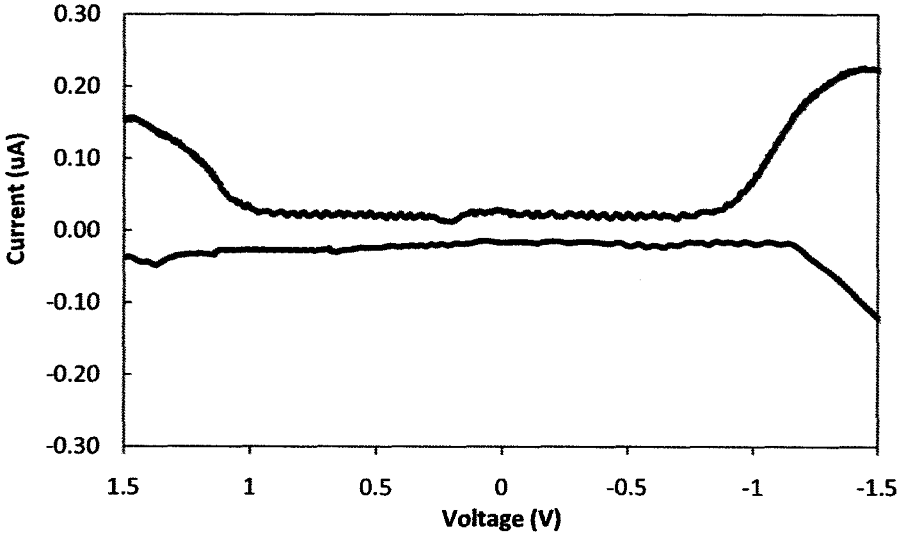

Figure 3.7 DPV spectra of (a) Pd nanoparticles of 4 nm and (b) Ru nanoparticles of 4 nm.

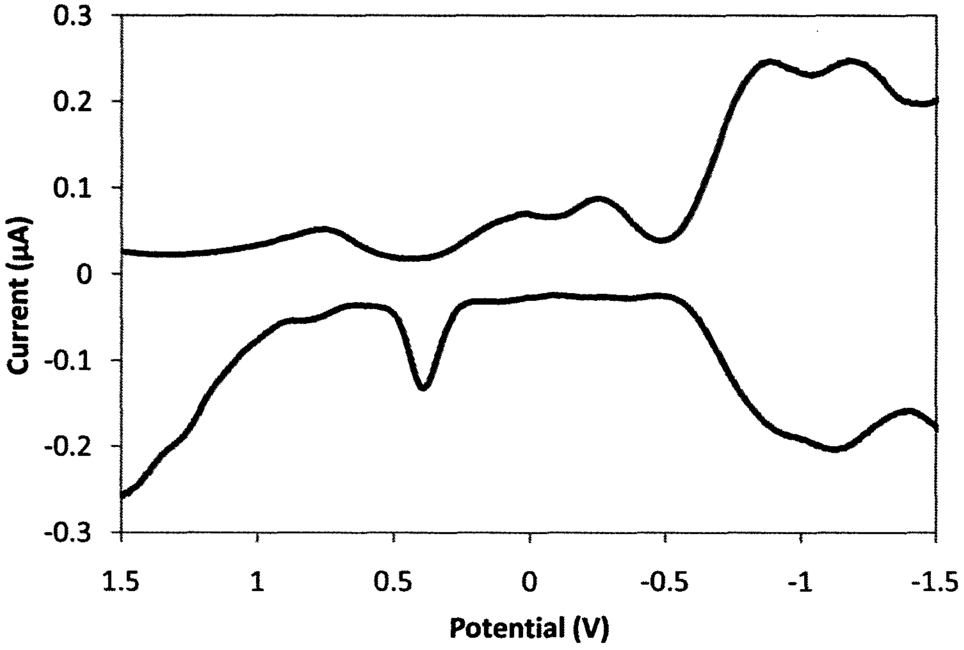

Figure 3.8 Differential Pulse Voltammograms of Pd-Ru bimetallic nanoparticles with diameter of 4.3 nm.

The voltammetric waves are quasi-symmetric in the range -0.5V to -2.0V, where three pairs of peaks represent three formal potentials for successive electron transfer (only one pair for particles of 5.3 nm). Since each of the redox potentials are very close for each sample, it suggests that the energy state configurations for the nanoparticle samples that are produced in reaction time range of 1.5h to 3h are similar to each other. Therefore, the DPV spectra agree with the size growth trend in the time frame, namely, the growth of particles was hindered by the depletion of small particles and free molecules. The results further support the Ostwald Ripening growth mechanism for the nanoparticles.

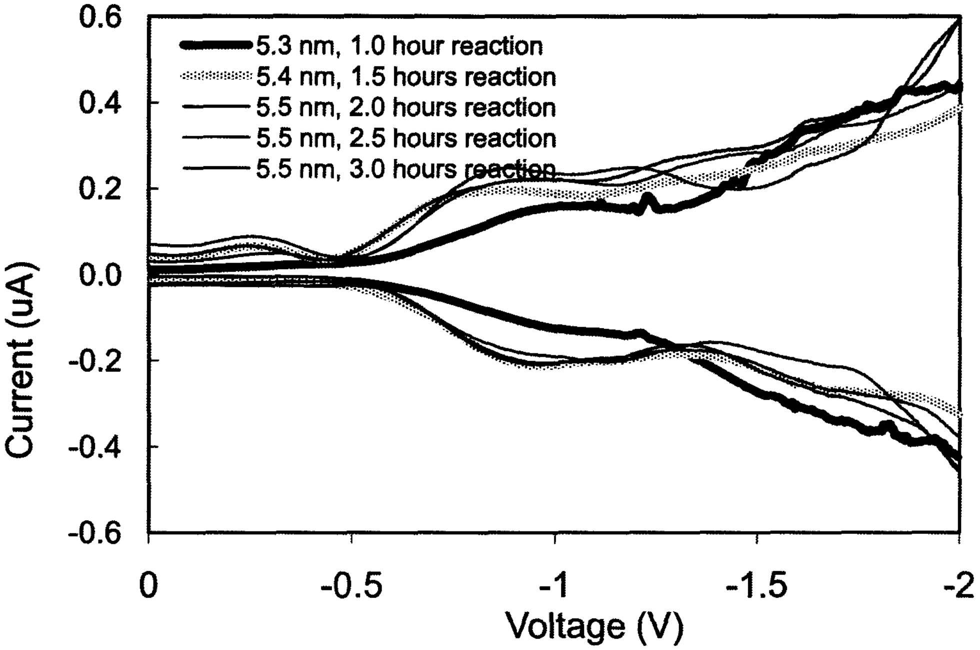

Figure 3.9 Differential pulse voltammograms of five Pd-Ru bimetallic nanoparticles samples produced at varied reaction times at 240°C. Each sample was prepared and quenched in varied reaction time.

Table 3.2 Formal potential and peak spacing for successive electron transfer.

Reaction time (hours)	Size measured in TEM (nm)	Formal potential (V), 1st, 2nd, 3rd, 4th	Peak spacing (ΔV)
1.0	5.3	-1.00	
1.5	5.4	-0.26, -0.89, -1.23, -1.65	0.63, 0.34, 0.40
2.0	5.5	-0.26, -0.93, -1.24, -1.65	0.67, 0.31, 0.41
2.5	5.5	-0.26, -0.89, -1.16, -1.62	0.63, 0.27, 0.46
3.0	5.5	-0.26, -0.93, -1.32, -1.68	0.67, 0.39, 0.36

3.3 Charging and discharging of Pd-Ru bimetallic nanoparticles

The urgent demand for renewable and sustainable energy has resulted in a surge of investigations on the use of nanoparticles, particularly in charge transfer processes. Photoexcited semiconductor nanoparticles undergo electron transfer to reach charge equilibration when they are in contact with metal nanoparticles. We showed in Chapter 2 that both Pd and Ru independently were able to accept electrons when brought in close proximity to charged TiO_2 nanoparticles. Charged Pd nanoparticles were able to discharge the electrons. However, charged Ru nanoparticles were unable to discharge to nearby redox couples. Here, we sought to determine the charging and discharging properties of Pd-Ru bimetallic alloy nanoparticles. A TiO_2 nanopowder suspension in methanol was prepared resulting in a white colored solution as shown in Figure 3.11a. The solution was placed in a cuvette, sealed with a septum and purged with nitrogen. The solution was then irradiated using a Xenon lamp. After 5 minutes of irradiation, the color of the solution changed to blue (Figure 3.11b). This blue coloration is attributed to the reduction of Ti(IV) to Ti(III), or the accumulation of electrons in the conduction band of TiO_2.

Injection of an aliquot of Pd-Ru bimetallic alloy nanoparticles to the irradiated TiO_2 (in the absence of irradiation) resulted in the blue discoloration and the appearance of a light yellow color corresponding to the alloy nanoparticles (Figure 3.11c). This color change suggests that the Pd-Ru nanoparticles could possibly trap the electrons that were initially stored in TiO_2.

Methyl viologen (MV^{2+}) was used as a redox couple to determine whether the particles stored in the Pd-Ru bimetallic nanoparticles could be discharged. A methanol solution of MV^{2+} was prepared resulting in a colorless solution. Upon addition to the charged Pd-Ru nanoparticles, a bright blue solution (Figure 3.11d) of reduced MV^{2+} in form of MV^{+} formed as illustrated in the equation below[35-37].

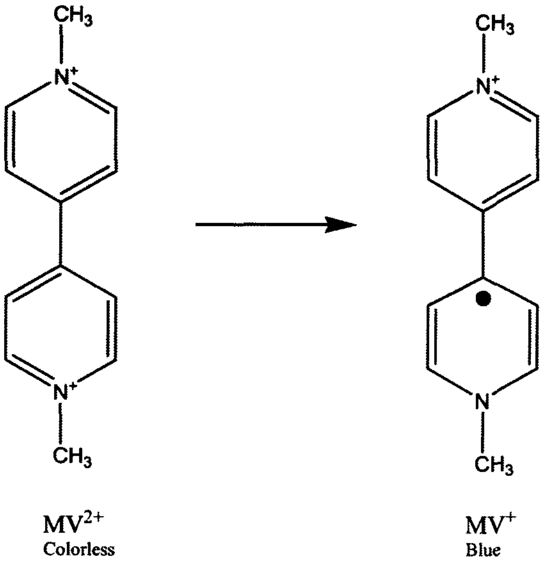

Figure 3.10 The result of the reaction of electron-rich particles with MV^{2+}.

The reduction of MV^{2+} to MV^{+} can be attributed to electron transfer through the discharge from the Pd-Ru nanoparticles to the MV^{2+}. It appeared that Pd-Ru nanoparticles behavior was similar to Pd nanoparticles alone where the electrons reside in the metal and are able to flow to the redox couple in the solution[38]. Thus, this work clearly shows the capability of Pd-Ru alloy bimetallic nanoparticles to store electrons from irradiated semiconductor and release the accumulated electrons redox couples in solution.

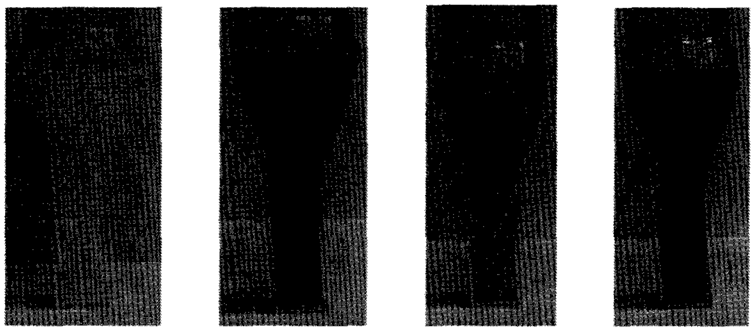

Figure 3.11 Solution color changes that occur when Pd-Ru bimetallic nanoparticles were brought in close proximity to irradiated TiO_2. (a) N_2 purged TiO_2 nanopowder suspended in methanol. (b)TiO_2 solution in methanol after 5 minute irradiation using a Xenon lamp. (c) Addition of an aliquot of deaerated Pd-Ru nanoparticles solution to the irradiated TiO_2 solution. (d) Formation of MV^+ by electron transfer from charged Pd-Ru bimetallic nanoparticles to MV^{2+}.

4. Summary

In conclusion, monodisperse Pd-Ru bimetallic alloy nanoparticles were synthesized by the simultaneous reduction of Pd and Ru precursors using *n*-dodecyl sulfide as both a stabilizing ligand and reducing agent. The electrochemical measurements obtained by differential pulse voltammetry demonstrated the single charge transfer properties for 4.3 nm bimetallic nanoparticles, which have not previously been measured nor observed in alloy nanoparticles. These particles were found to accept charge when brought in close proximity to charged semiconductor nanoparticles. Discharge of the stored electrons on the Pd-Ru nanoparticles occurred when MV^{2+} was brought in contact with the charged nanoparticles. These results demonstrated the ability of quantized nanoparticles to serve as electron carriers and discharge the electrons as needed.

5. References

1. Toshima, N.; Yonezawa, T., Bimetallic nanoparticles - novel materials for chemical and physical applications. *New Journal of Chemistry* **1998,** 22, (11), 1179-1201.

2. Toshima, N.; Kushihashi, K.; Yonezawa, T.; Hirai, H., Colloidal dispersions of palladium-platinum bimetallic clusters protected by polymers - preparation and application of catalysis. *Chemistry Letters* **1989,** (10), 1769-1772.

3. Toshima, N.; Yonezawa, T.; Kushihashi, K., Polymer-protected palladium-platinum bimetallic clusters - preparation, catalytic properties and structural considerations. *Journal of the Chemical Society-Faraday Transactions* **1993,** 89, (14), 2537-2543.

4. Toshima, N.; Harada, M.; Yamazaki, Y.; Asakura, K., Catalytic activity and structural-analysis of polymer-protected Au-Pd bimetallic clusters prepared by the simultaneous reduction of HAuCl4 and PdCl2. *Journal of Physical Chemistry* **1992,** 96, (24), 9927-9933.

5. Toshima, N.; Wang, Y., Perperation and catalysis of novel colloidal dispension of copper noble-metal bimetallic clusters. *Langmuir* **1994,** 10, (12), 4574-4580.

6. Toshima, N.; Wang, Y., Novel preparation, characterization and catalytic properties of polymer-protected Cu/Pd bimetallic colloid. *Chemistry Letters* **1993,** (9), 1611-1614.

7. Toshima, N.; Wang, Y., Polymer-protected Cu/Pd bimetallic clusters. *Advanced Materials* **1994,** 6, (3), 245-247.

8. Toshima, N.; Hirakawa, K., Polymer-protected Pt/Ru bimetallic cluster catalysts for visible-light-induced hydrogen generation from water and electron transfer dynamics. *Applied Surface Science* **1997,** 121, 534-537.

9. Yonezawa, T.; Toshima, N., Polymer-protected and micell-protected gold platinum bimetallic systems - preparation, application to catalysis for visible-light-induced hydrogen evolution, and analysis of formation process with optical methods. *Journal of Molecular Catalysis* **1993,** 83, (1-2), 167-181.

10. Scott, R. W. J.; Wilson, O. M.; Oh, S. K.; Kenik, E. A.; Crooks, R. M., Bimetallic palladium-gold dendrimer-encapsulated catalysts. *Journal of the American Chemical Society* **2004,** 126, (47), 15583-15591.

11. Sivakumar, P.; Ishak, R.; Tricoli, V., Novel Pt-Ru nanoparticles formed by vapour deposition as efficient electrocatalyst for methanol oxidation Part I. Preparation and physical characterization. *Electrochimica Acta* **2005,** 50, (16-17), 3312-3319.

12. Scott, R. W. J.; Datye, A. K.; Crooks, R. M., Bimetallic palladium-platinum dendrimer-encapsulated catalysts. *Journal of the American Chemical Society* **2003,** 125, (13), 3708-3709.

13. Ricci, A.; Lo Sterzo, C., A new frontier in the metal-catalyzed cross-coupling reaction field. The palladium-promoted metal-carbon bond formation. Scope and mechanism of a new tool in organometallic synthesis. *Journal of Organometallic Chemistry* **2002,** 653, (1-2), 177-194.

14. Astruc, D., Palladium nanoparticles as efficient green homogeneous and heterogeneous carbon-carbon coupling precatalysts: A unifying view. *Inorganic Chemistry* **2007,** 46, (6), 1884-1894.

15. Moreno-Manas, M.; Pleixats, R., Formation of carbon-carbon bonds under catalysis by transition-metal nanoparticles. *Accounts of Chemical Research* **2003,** 36, (8), 638-643.

16. Shimazaki, Y.; Kobayashi, Y.; Yamada, S.; Miwa, T.; Konno, M., Preparation and characterization of aqueous colloids of Pt-Ru nanoparticles. *Journal of Colloid and Interface Science* **2005,** 292, (1), 122-126.

17. Schmidt, T. J.; Gasteiger, H. A.; Behm, R. J., Methanol electrooxidation on a colloidal PtRu-alloy fuel-cell catalyst. *Electrochemistry Communications* **1999,** 1, (1), 1-4.

18. Kim, I. T.; Lee, H. K.; Shim, J., Synthesis and Characterization of Pt-Pd Catalysts for Methanol Oxidation and Oxygen Reduction. *Journal of Nanoscience and Nanotechnology* **2008,** 8, (10), 5302-5305.

19. Raja, R.; Sankar, G.; Hermans, S.; Shephard, D. S.; Bromley, S.; Thomas, J. M.; Johnson, B. F. G., Preparation and characterisation of a highly active bimetallic (Pd-Ru) nanoparticle heterogeneous catalyst. *Chemical Communications* **1999,** (16), 1571-1572.

20. Yu, K. M. K.; Meric, P.; Tsang, S. C. In *Micelle-hosted bimetallic Pd-Ru nanoparticle for in situ catalytic hydrogenation in supercritical CO2*, 2006; Elsevier Science Bv: 2006; pp 428-433.

21. Shon, Y. S.; Dawson, G. B.; Porter, M.; Murray, R. W., Monolayer-protected bimetal cluster synthesis by core metal galvanic exchange reaction. *Langmuir* **2002,** 18, (10), 3880-3885.

22. Son, S. U.; Jang, Y.; Park, J.; Na, H. B.; Park, H. M.; Yun, H. J.; Lee, J.; Hyeon, T., Designed synthesis of atom-economical Pd/Ni bimetallic nanoparticle-based catalysts for sonogashira coupling reactions. *Journal of the American Chemical Society* **2004,** 126, (16), 5026-5027.

23. Ganesan, M.; Freemantle, R. G.; Obare, S. O., Monodisperse thioether-stabilized palladium nanoparticles: Synthesis, characterization, and reactivity. *Chemistry of Materials* **2007,** 19, (14), 3464-3471.

24. Turkevich, J.; Stevenson, P. C.; Hillier, J., A study of the nucleation and growth processes in the synthesis of colloidal gold. *Discussions of the Faraday Society* **1951,** (11), 55-&.

25. Voorhees, P. W., The theory of Ostwald ripening. *Journal of Statistical Physics* **1985,** 38, (1-2), 231-252.

26. Tabuani, D.; Monticelli, O.; Chincarini, A.; Bianchini, C.; Vizza, F.; Moneti, S.; Russo, S., Palladium Nanoparticles Supported on Hyperbranched Aramids: Synthesis, Characterization, and Some Applications in the Hydrogenation of Unsaturated Substrates. *Macromolecules* **2003,** 36, (4294-4301).

27. Lu, W.; Wang, B.; Wang, K.; Wang, X.; Hou, J. G., Synthesis and Characterization of Crystalline and Amorphous Palladium Nanoparticles. *Langmuir* **2003,** 19, 5887-5891.

28. Chen, S. W.; Templeton, A. C.; Murray, R. W., Monolayer-protected cluster growth dynamics. *Langmuir* **2000,** 16, (7), 3543-3548.

29. Chen, S. W.; Ingram, R. S.; Hostetler, M. J.; Pietron, J. J.; Murray, R. W.; Schaaff, T. G.; Khoury, J. T.; Alvarez, M. M.; Whetten, R. L., Gold nanoelectrodes of varied size: Transition to molecule-like charging. *Science* **1998,** 280, (5372), 2098-2101.

30. Hicks, J. F.; Templeton, A. C.; Chen, S. W.; Sheran, K. M.; Jasti, R.; Murray, R. W.; Debord, J.; Schaaf, T. G.; Whetten, R. L., The monolayer thickness

dependence of quantized double-layer capacitances of monolayer-protected gold clusters. *Analytical Chemistry* **1999,** 71, (17), 3703-3711.

31. Lee, D.; Donkers, R. L.; Wang, G. L.; Harper, A. S.; Murray, R. W., Electrochemistry and optical absorbance and luminescence of molecule-like Au-38 nanoparticles. *Journal of the American Chemical Society* **2004,** 126, (19), 6193-6199.

32. Branham, M. R.; Douglas, A. D.; Mills, A. J.; Tracy, J. B.; White, P. S.; Murray, R. W., Arylthiolate-protected silver quantum dots. *Langmuir* **2006,** 22, (26), 11376-11383.

33. Kim, J.; Lema, K.; Ukaigwe, M.; Lee, D., Facile preparative route to alkanethiolate-coated Au-38 nanoparticles: Postsynthesis core size evolution. *Langmuir* **2007,** 23, (14), 7853-7858.

34. Kim, Y. G.; Garcia-Martinez, J. C.; Crooks, R. M., Electrochemical properties of monolayer-protected Au and Pd nanoparticles extracted from within dendrimer templates. *Langmuir* **2005,** 21, (12), 5485-5491.

35. Ebbesen, T. W.; Levey, G.; Patterson, L. K., Photo-reduction of methyl violgen in aqueous neutral solution without additives. *Nature* **1982,** 298, (5874), 545-548.

36. Ebbesen, T. W.; Ferraudi, G., Photochemistry of methyl viologen in aqueous and methanolic solutions. *Journal of Physical Chemistry* **1983,** 87, (19), 3717-3721.

37. Watanabe, T.; Honda, K., Measurement of the extinction coefficient of the methyl viologen cation radical and the efficiency of its formation by semiconductor photocatalysis. *Journal of Physical Chemistry* **1982,** 86, (14), 2617-2619.

38. Wood, A.; Giersig, M.; Mulvaney, P., Fermi level equilibration in quantum dot-metal nanojunctions. *Journal of Physical Chemistry B* **2001,** 105, (37), 8810-8815.

CHAPTER IV

FABRICATION AND CHARACTERIZATION OF METALLIC NANOWIRES

1. Introduction

One dimensional metallic nanostructures (such as nanowires, nanotubes and nanorods) are of great scientific and practical interest. Their unique structures offer various opportunities for advancements in materials science, biology, biomedical sciences, electronics, optics, magnetism, energy storage, and electrochemistry.

Nanoscale metal structures have interesting optical, electronic, electrochemical, and magnetic properties that are composition, size and shape dependant[1]. For example, Au and Ag metallic nanorods have displayed unique optical properties with respect to their aspect ratio[2]. Au nanocylinders have found decorative and protective applications similar to gold nanoparticles. A number of one dimensional nanostructures with high aspect ratio have been found to display electron transport properties and improved conductivities[1, 3-6]. In this regard, gold nanowires have found applications as electrodes to offer opportunities to study the kinetics of charge-transfer processes that are too fast to measure at conventional macroscopic electrodes[7]. Additionally, conductive metal nanowires have been used as an electron source of high effective field emission due to their superconducting properties[8]. Magnetic nanowires were commonly studied for clinical applications, such as cell separation, thermotherapy and drug delivery by using their high response to external magnetic field that can be easily manipulated.

While a number of methods including lithography, chemical vapor deposition, physical vapor deposition, sol-gel deposition, chemical polymerization, and vapor liquid solid growth have been used for the fabrication of nanowires, electrochemical deposition is becoming an increasingly attractive method for the synthesis of new materials and nanostructures. Traditionally, electrochemistry has been used to grow thin films on conductive substrates. Electrochemical deposition could be a convenient way of generating one dimensional nanostructures by simultaneously controlling the dimensions, properties, and morphology. The use of mild reaction conditions (low temperature and low cost) makes electrochemical deposition a competitive technique.

Most electrochemical deposition methods for nanowire synthesis are based on the use of "templates". A notable method was pioneered by Charles R. Martin for the fabrication of metallic and semiconductor nanowires and nanotubes[9-11]. In this case the templates used were nanoporous membranes having cylindrical shaped pores of controllable pore diameter and with a narrow size distribution. The metal atoms were electrochemically reduced and deposited inside the nanopores and then formed one-dimensional structures. In this chapter, the synthesis and characterization of one- and two-component metallic nanowires will be discussed. Scanning electron microscopy (SEM) was used to image the nanowires and confirm their size and shape. The elemental composition of the nanowires was determined by energy-dispersive x-ray spectroscopy (EDX) and X-ray photoelectron spectroscopy (XPS).

2. Experimental details

Materials. Anodic aluminum oxide (AAO) membranes were purchased from VWR and used as received. Au plating solution (2.5 DWT/Qt) and Ag plating solution (Technic Silver 1025) were purchased from Technic Inc. Copper sulfide ($CuSO_4$), boric acid (H_3BO_3), titanium (III) chloride ($TiCl_3$), sodium hydroxide (NaOH) and folic acid were obtained from VWR and used without further purification. Riboflavin 5'-phosphate sodium (flavin mononucleotide (FMN)) was purchased from Sigma Aldrich Company and used as received.

2.1 Synthesis of one component nanowires

One surface of AAO membranes was sputter coated with an 80 nm thick film of Au. The electrolyte used and the current applied for various metallic nanowires are listed in Table 4.1. After 1 hour deposition, the AAO membrane was dissolved in 6M NaOH for about 20 minutes, followed by sonication for about 5 minutes. The NaOH solution was centrifuged at 8K rpm for 2 minutes. The isolated solid sample was redissolved in water and sonicated in ethanol for cleaning. The sample was dried in a vacuum dessicator overnight. SEM images were obtained by attaching the dried sample to a carbon tape.

Table 4.1 Electrolyte and voltage needed for one component nanowire fabrication.

Nanowires	Electrolyte	Applied current
Ag nanowires	Technic Silver 1025 (contains KCN, K_2CO_3, $KAg(CN)_2$ and pH = 10 ~12)	2 mA (Pt gauze as counter electrode)
Au nanowires	Orotemp 24, 2.5 DWT/Qt (contains KCN, citric acid, $KAu(CN)_2$ and pH = 5~7)	2 mA (Pt gauze as counter electrode)
Cu nanowires	0.02 M $CuSO_4$ and 0.5 M H_3BO_3	4 mA (Pt gauze as counter electrode)
Au nanotubes	Orotemp 24, 2.5 DWT/Qt	26 mA (Pt gauze as counter electrode)

2.2 Synthesis of two component nanowires

Synthesis of Ni-Au two component nanowires. The procedure for making Ni/Au two-component nanowires employed a sequential electrodeposition method. Initially, a small amount of Ni was electrodeposited from a 0.2 M $NiCl_2$, 0.5 M H_3BO_3 aqueous solution at -1.5V (*vs.* Ni wire) for 30 minutes. Then the plating solution was switched to a gold plating solution (2.5 DWT/Qt, Technic Inc.). By applying constant current 3 mA (1 cm × 1.5 cm platinum gauze as reference electrode) for 1 hour, metal gold was deposited on top of the Ni nanowire segment that was initially formed.

For making Au coated Ni nanowires, the Au shell was first formed by applying 26 mA constant current in a Au plating solution for 30 minutes. Then the solution was switched to Ni plating solution and the counter electrode was switched to a Ni wire. A constant voltage of -1.5 V was applied for 20 minutes allowing the deposition of Ni to take place.

Nanowires suspended in low viscosity liquid such as water, ethanol, and 2-propanol precipitate from the solution in a time frame of a few minutes. Magnetic nanowires like Ni nanowires aggregate due to interwire magnetic forces. For better suspension and to avoid aggregation, nanowires should be kept in more viscous media such as ethylene glycol[12].

Synthesis of metallic alloy nanowires. Alloy nanowires were fabricated by modulating the potential in a solution that contains two different metal ions. Ag-Au alloy nanowires was grown in an electrolyte containing 20% Ag plating solution and 80% Au plating solution under an applied constant current of 2 mA (*vs.* Pt gauze) for 1 hour. The electrolyte for making Ni-Cu alloy nanowires was 0.2 M $NiCl_2$, 0.5 M H_3BO_3 and 0.02 $CuSO_4$ aqueous solution and the applied voltage was -1.5V (*vs.* Ni wire) for 30 minutes. Au-Cu alloy nanowires could be obtained by applying 2 mA constant current (*vs.* Pt gauze) in the presence of an electrolyte consisting of Au plating solution (Orotemp 24) and 0.04 M $CuSO_4$, for 1 hour. The electrolyte for fabrication of Ti-Ni alloy nanowires contained 0.2 M $NiCl_2$ and 0.05M $TiCl_3$ and HCl (pH = 4). Ti-Ni alloy nanowires were formed under a potential of -1.5 V (*vs.* Ni wires) for 1 hour.

2.3 Functionalization of Ni nanowires

Magnetism measurement of folic-acid coated Ni nanowires. The nanowires were washed with ultra-pure water, followed by ethanol. The dried nanowires were suspended in a folic acid aqueous solution at room temperature by stirring the solution for 24 hours to ensure the binding. Then folic acid coated nanowires were washed and dried before magnetism measurement by SQUID magnetometer (Quantum Design, MPMS7). The preweighted dry sample (bare Ni nanowires or folic acid coated nanowires) was put inside a small plastic bag and carefully sealed to avoid sample loss. The sealed bag was inserted into a plastic straw to make a sample rod which will float in the center of the magnetic field. The magnetization *vs.* strength of external magnetic field (M-H) curves at temperatures of 3K, 100K and 300K were recorded. The contribution of the plastic container was considered to correct the molar magnetic susceptibilities. The saturation magnetization (M_s), remanence magnetization M_r and coercive field (H_C) were determined[13]. The relationship between magnetic field strength (H) and magnetization (M) is not linear in magnetic materials. If the relationship between the two is plotted for increasing levels of field strength, it will follow a curve up to a point where further increases in magnetic field strength will result in no further change in magnetic moment. This condition is called magnetic saturation (Ms). After an external magnetic field is removed, the magnetization left behind in the material is remanence magnetization (M_r). The opposite magnetic field required to reduce the magnetization of the tested material to zero is coercivity (or coercive field (Hc)).

Fluorescence study of FMN coated Ni nanowires. The terminal phosphonic acid groups of flavin mononucleotide (FMN) are hard bases and bind with high affinity to hard acid like Ni[14]. The surface binding took place in 24 hours reaction of 5 mM concentration of FMN with 10^9 Ni nanowires. The solution was then centrifuged and the supernatant was decanted. The precipitated nanowires were resuspended in ethanol for washing off the excess FMN. The procedure was repeated till no FMN could be measured in the supernatant solution. The fluorescence microscope image was taken in Nikon Eclipse E600 Microscope with the filter that allows the emission wavelength of 460~500 nm.

3. Results and discussion

An electrochemical deposition method[15] was used to fabricate metallic and bimetallic nanowires of various compositions. Anodic aluminum oxide (AAO) membranes were used as templates for the nanowires. As illustrated in Scheme 4.1, the holes are equally distributed and the cylinder shapes are uniform. The thickness and pore density of AAO membranes are about 4 μm and 10^{10} cm^{-2}, respectively. Templates with pore diameters of 20 nm, 100 nm and 200 nm are commercially available and were formed by anodic oxidation of aluminum metal in a solution of sulfuric, oxalic, or phosphoric acid[16-19].

Scheme 4.1 shows a schematic representation of the electrochemical deposition process. Electrodeposition of a material within the pores of the matrix is preceded by coating one face of the template with a metal film and using this metal film as a cathode or anode for electroplating. A vacuum evaporation method using a sputter coater can form very thin and uniform monolayer of metal film. Some metal eutectic or conductive paints may be used to provide conductivity, but the efficiency is typically low relative to sputter coating. Au, Cu and Ag are the most frequently used metals for coating. Under an applied potential, ions in a plating solution are oxidized or reduced to the nanowire material. The pore volume is continuously filled up from the pore bottom. The thickness of the membrane determines the maximum length of the resulting nanowires. The amount of time applied during the deposition process was used to control the length the resulting nanowires. After the nanowires with desired length formed, the setup was disconnected, and the AAO membranes are dissolved in strong base such as 6M NaOH and resulted in free standing nanowires.

A typical experimental setup is illustrated in Scheme 4.2. Here, the AAO membranes are attached to an indium tin oxide (ITO) coated glass slide and a thin Au film serves as a contact between the AAO membrane and the indium tin oxide. The conductive ITO glass slide served as working electrode. A Pt gauze was used as both the reference and the counter electrode during the fabrication of gold, silver and titanium nanowires. For the fabrication of Ni and Cu, the Ni wire and Cu wire were used as both reference and counter electrodes, respectively.

Chronoamperometry (*I-t* characteristics) was used to study the growth of a complete pore-filling process. Four different stages of the pore-filling process could be distinguished. Scheme 4.3 shows a typical *I-t* curve that simulates the current change during the growth of metallic nanowires. Initially, a rapid increase in current is ascribed to the charge of the electrical double layer. Since the deposition current depends on the mass-transport conditions and effective surface area of the electrode, the recorded *I-t* curve during deposition reveals four different stages[20]: 1) Metal started to form on the bottom of the channel. The current drop was due to slow mass diffusion process inside the small channel. 2) Metal grew to fill the channel. The current slightly increases because of the shortened diffusion distance. 3) Metal started to grow over the top of the channel. The working electrode surface became bigger which gave rise to the increase of the current. 4) Metal connected to form a film on the top of the membrane. The current stabilized in this stage because of the constant working electrode area. When the reaction was stopped in stage 2, isolated and separated nanowires could be obtained after the membrane was dissolved.

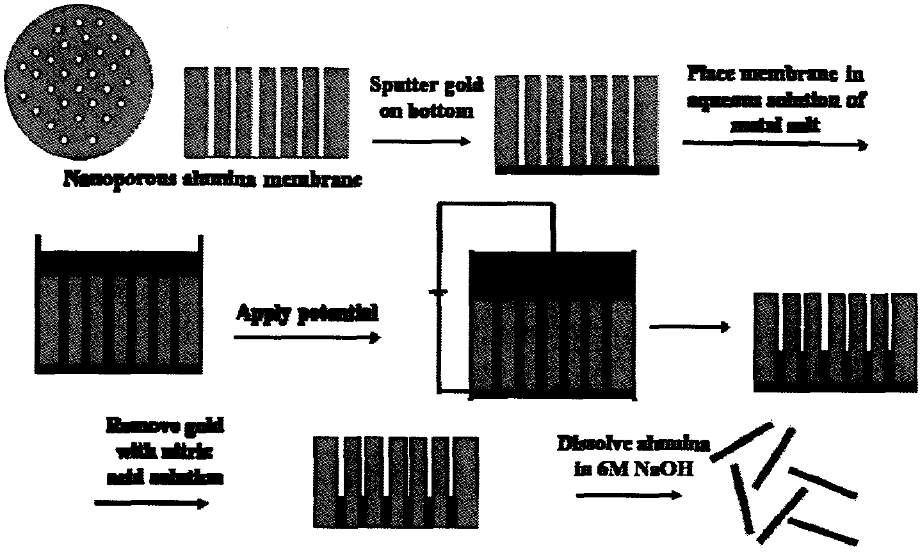

Scheme 4.1 Schematic representation for the electrochemical deposition method.

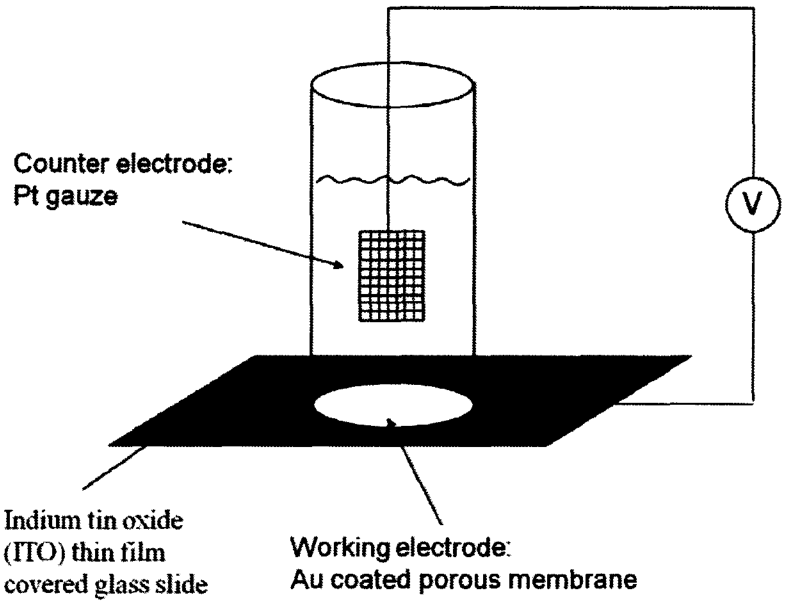

Scheme 4.2 Schematic representation of the experimental setup for making metallic nanowires.

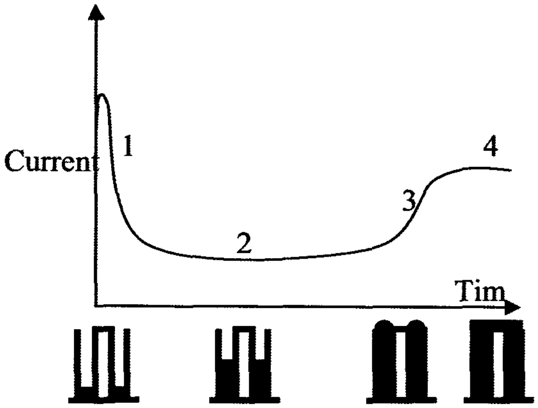

Scheme 4.3 Different stages of pore-filling process during electrochemical deposition of metallic nanowires. Electrochemical reduction current, *I*, was plotted as function of time, *t*. 1) Metals beginning to grow into the wires; 2)

metals growing to fill up the pores; 3) metals growing over the channel and 4) connecting to form a film.

3.1 Synthesis and characterization of one component nanowires

Figure 4.1-4.3 display the nanowires that are composed of Au, Ag and Cu, respectively. EDAX analysis revealed that the Au and Ag nanowires were exclusively made of Au or Ag, respectively. The morphology of Au, Ag and Cu nanowires visualized by SEM showed that they are 200 nm in diameter, and the lengths are in the range of a few micrometers. Because of the growth rate of different metal is different under their applied voltage, the same deposition time may result in various lengths for each of the metal nanowires. The Au and Ag nanowires have high mechanical strength, thus no bending or pits were observed from SEM images. While in the case of Cu nanowires the surface was not smooth as for Au or Ag, it may suggest that the Cu nanowires were fragile and easily broken during the isolation process.

The applied voltage or current determined the growth rate of the nanowires and in some cases the structures of the nanomaterials. Figure 4.4 displays the Au nanotubes with a length of 1 to 2 μm. They were synthesized when the applied current was set to 26 mA, which was much higher than that applied for the fabrication of Au nanowires. Under a high applied potential, metal ions diffused into the AAO membrane pores and were preferentially deposited on the pore wall to form nanotubes. This method only produced short metallic nanotubes. When longer deposition time was used, the metal ions would fill up the tube to form solid wires[21].

However, the overall method provides a straightforward technique to fabricate nanotubes with any electroplatable material. Nanotubes have potential applications because of their hollow structure, ranging from agents for drug delivery to solar cells.

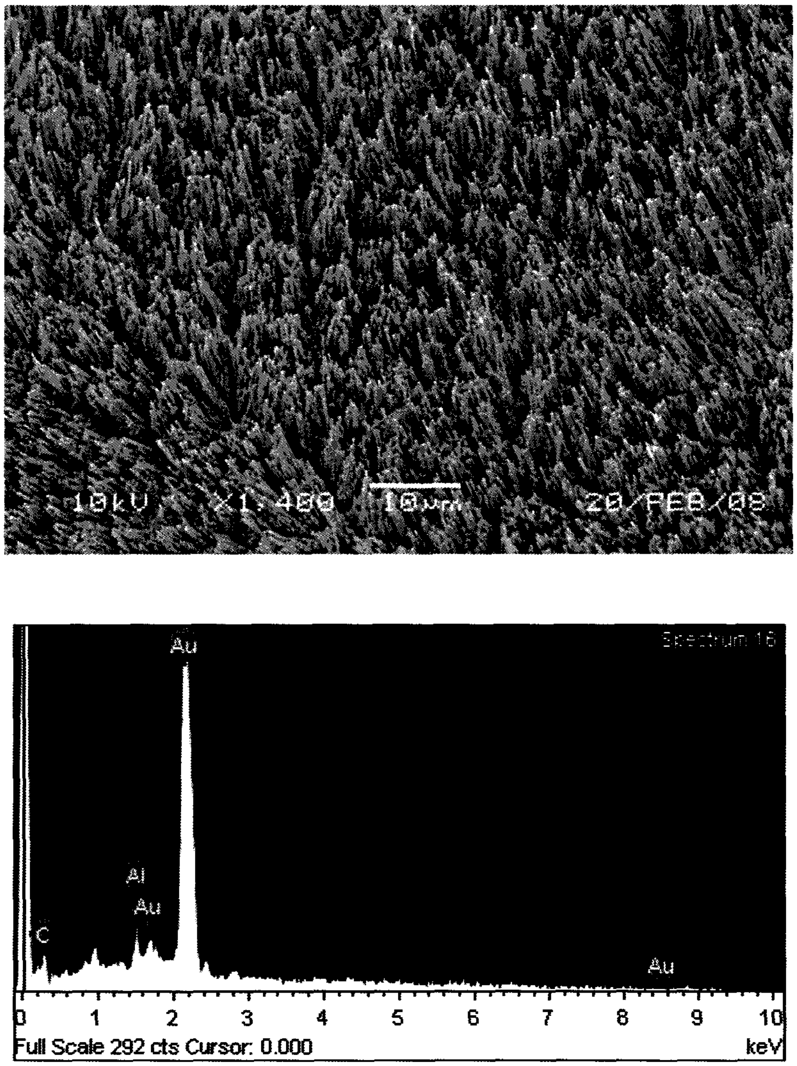

Figure 4.1 SEM image and EDAX spectrum of Au nanowires. The nanowires were held together by the undissolved Au film at the surface. The diameter of a single nanowire was 200 nm and the length was 8 μm.

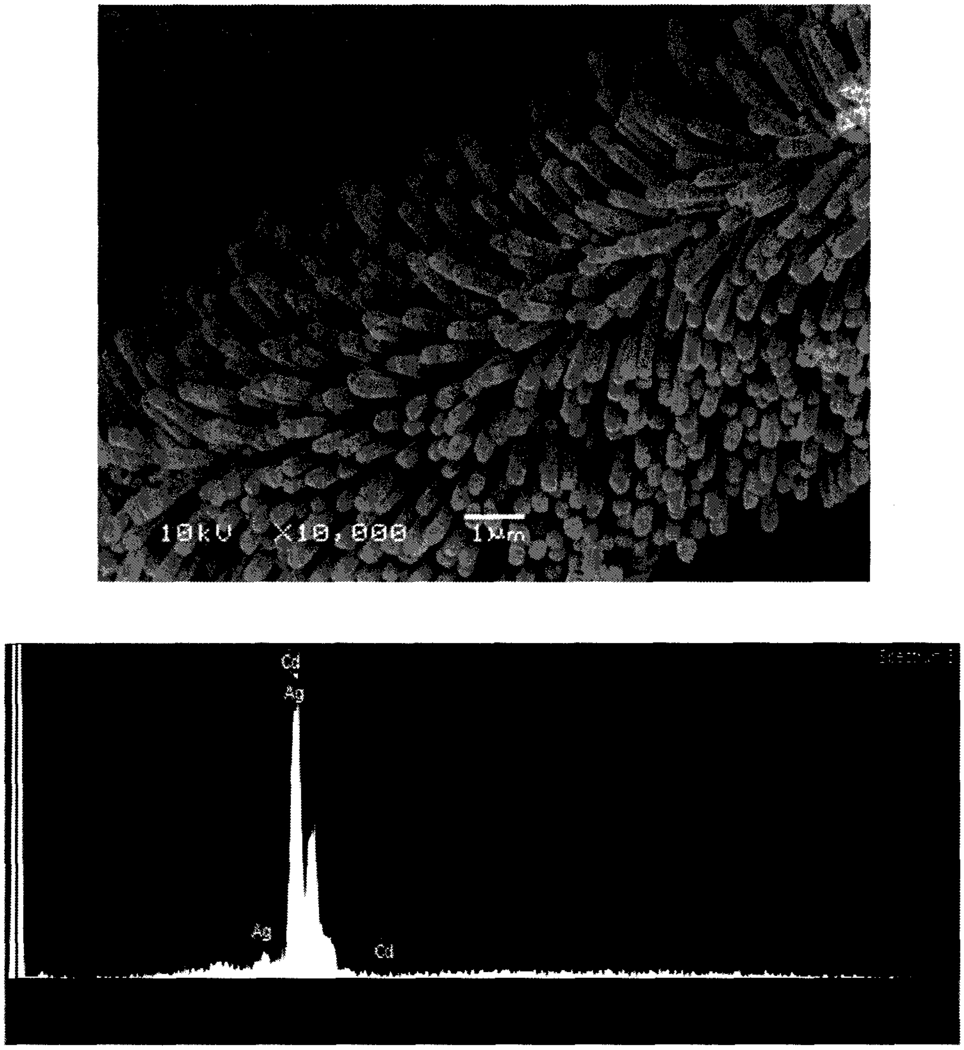

Figure 4.2 SEM image and EDAX spectrum of Ag nanowires array. Nanowires were attached on Au film which folded during the preparation. The diameter was 200 nm and the length was 3 μm.

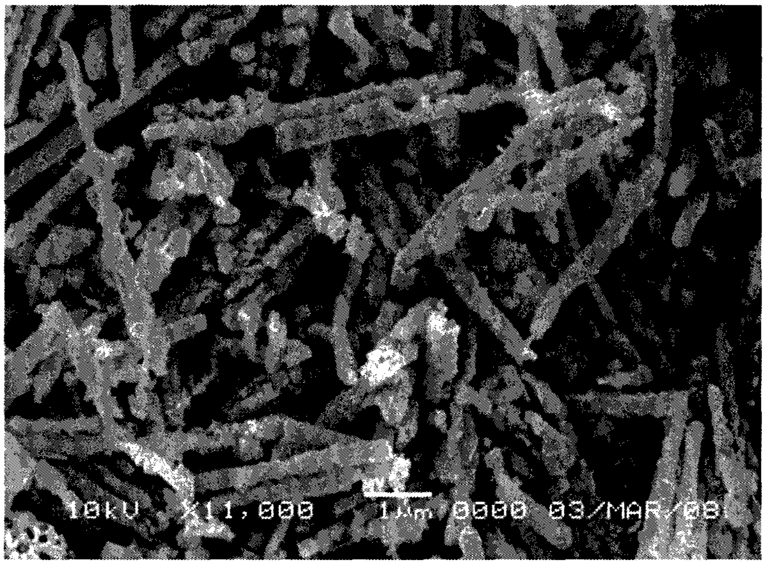

Figure 4.3 SEM image of Cu nanowires. The surface of the nanowire is rough and is attached to membrane residues. The average diameter was 200 nm and the length ranged from 4 to 5 µm.

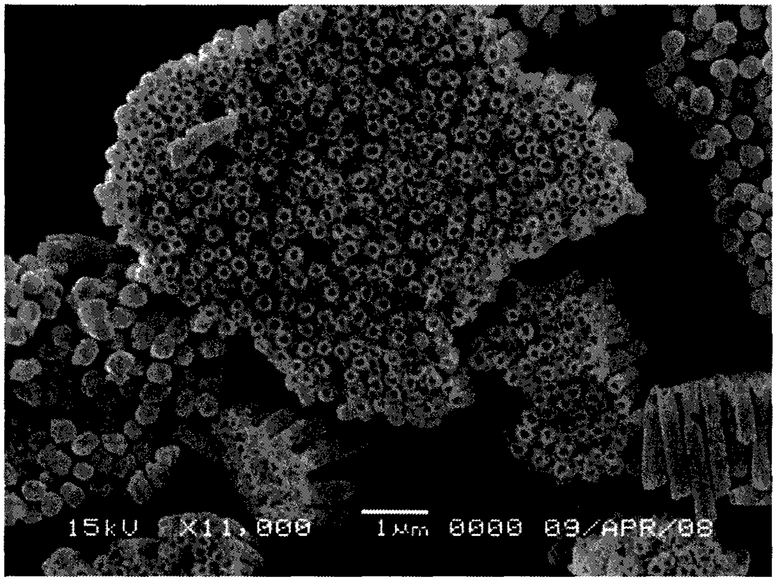

Figure 4.4 SEM images of Au nanotubes.

3.2 Synthesis and characterization of two component nanowires

Multi-component nanowires are materials with a wide range of applications. SEM images (Figure 4.5) shows the Au/Ni nanowires, where all components can be distinguished from each other by the difference in the shade which is due to the difference in electron density of the two elements. The order of each component can be manipulated as desired, such as the Ni/Au/Ni three segments nanowires in Figure 4.5b.

Carefully controlling the right deposition voltage, hollow Au nanotube structure could be achieved, leading to the formation of Au coated Ni nanowires. Figure 4.6 shows the Au coated Ni nanowires. Ni was deposited inside the as-prepared Au nanotubes. Therefore, magnetic nanowires covered with a new surface were generated.

(a)

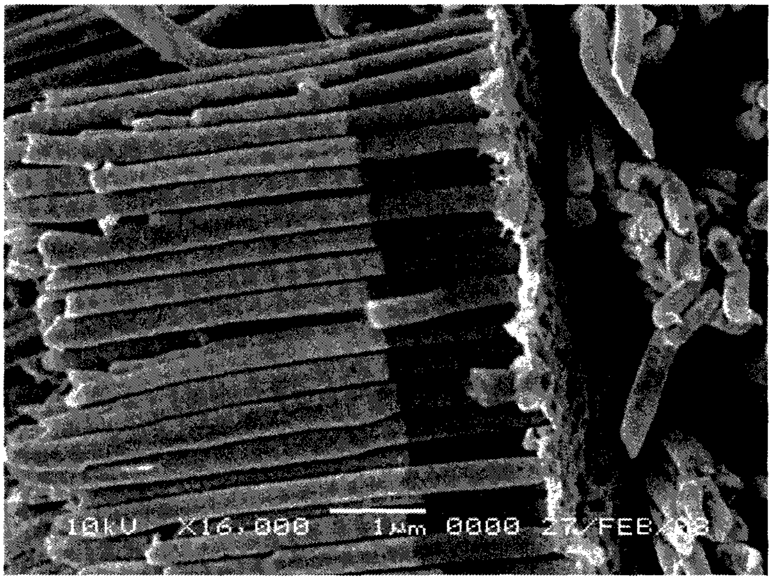

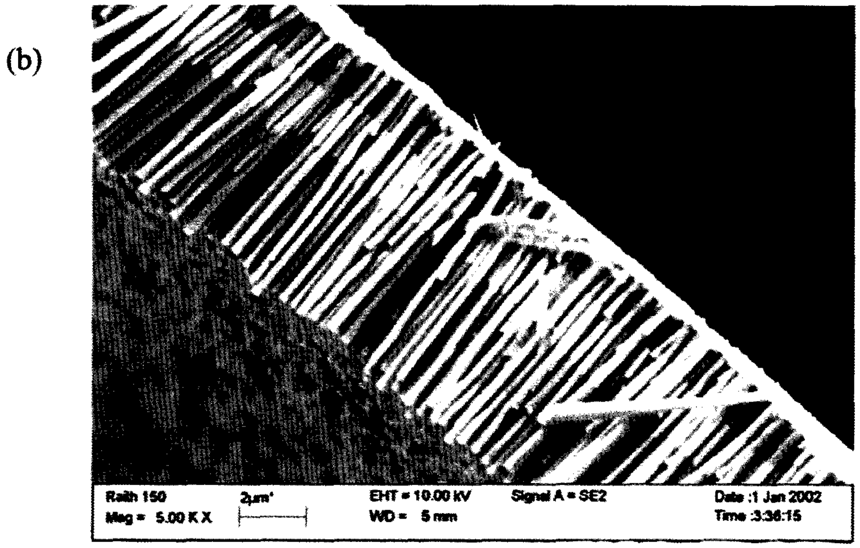

Figure 4.5 SEM images of Au/Ni two components metallic nanoparticles. The arrangement of Au and Ni component could be controlled as desired: (a) Au component was on top of Ni component, (b) one more Ni portion was grown on the Au component forming a three segment structure.

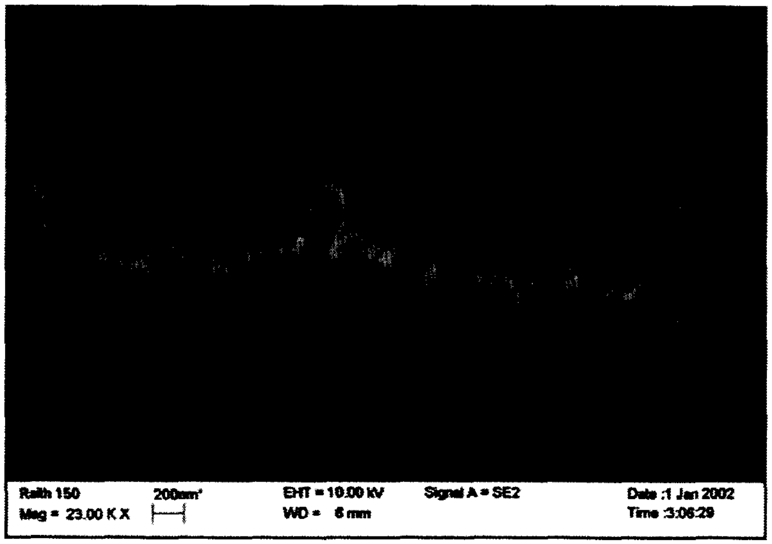

Figure 4.6 SEM of Au coated Ni nanowires. Ni was deposited inside the Au nanotubes.

3.3 Synthesis and characterization of alloy nanowires

The co-reduction of two metal ions co-existing in an electrolyte solution was used to produce metallic alloy nanowires. The composition of the two metals was controlled by adjusting the concentration ratio of both ions in the solution. Figure 4.7 shows an SEM image of Ag-Au alloy nanowires and the corresponding EDAX spectrum confirming the elemental composition of the Au and Ag. When the Au and Ag plating solution were mixed in a 4:1 ratio the resulting alloy contained 9 part Ag and 1 part Au. This was determined from the electrochemical reduction reaction rate of each metal under the applied potential and the concentrations. By adjusting either or both of the parameters, the composition ratio can be varied as desired. In this manner, Ni-Cu alloy nanowires with the composition ratio of 2:1 (Figure 4.8) and Au-Cu alloy nanowires with the composition ratio of 1:2 (Figure 4.9) were synthesized. Figure 4.10 shows the Ti-Ni alloy nanowires which are shape-memory materials. Their shape-memory properties (such as transition temperature, yield strength) are related to their composition. The 1:1 ratio of Ti:Ni was synthesized in the electrolyte that contain 1:4 ratio of Ti and Ni precursors. The resulted nanowires look soft and smooth in surface. They tended to form bundles by bending to each other.

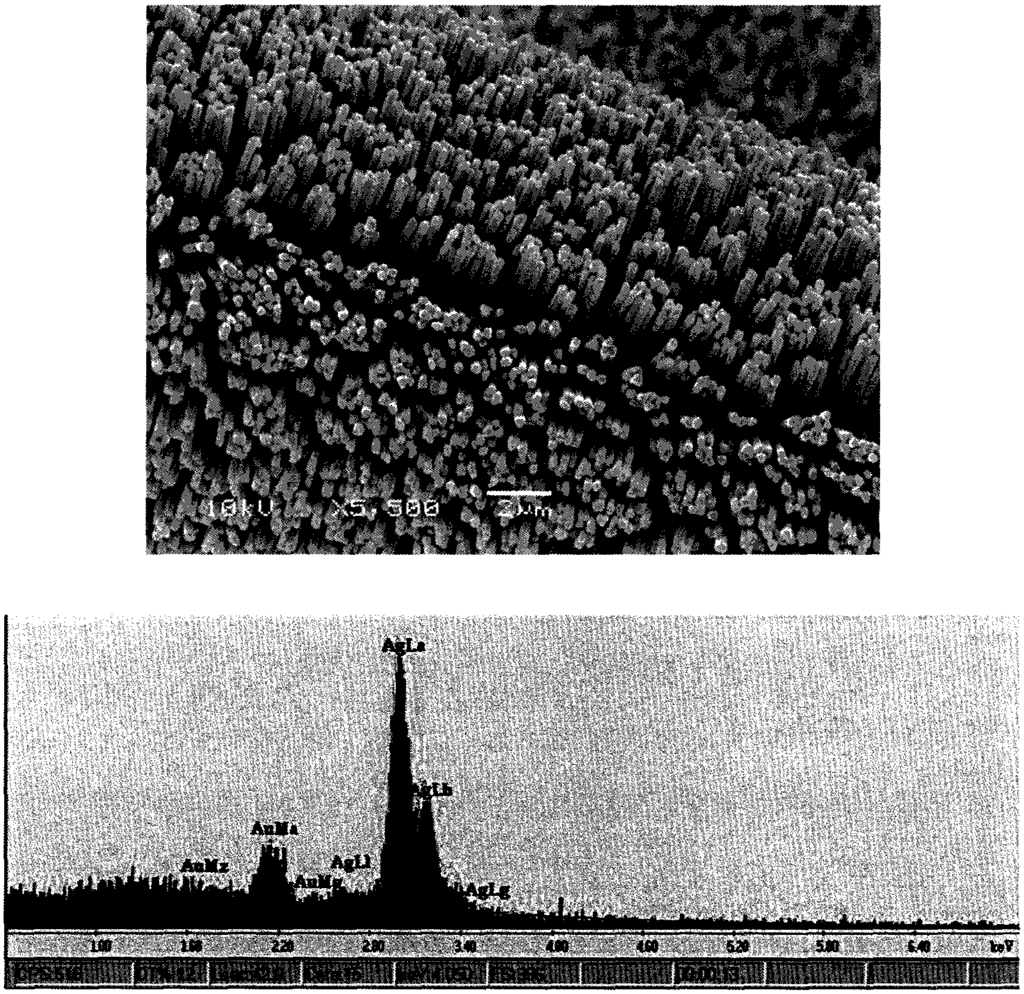

Figure 4.7 SEM image and EDAX spectrum of Ag-Au alloy nanowires array. The atomic ratio of Ag:Au was 9:1. The length was about 2 μm and the diameter was 250 nm.

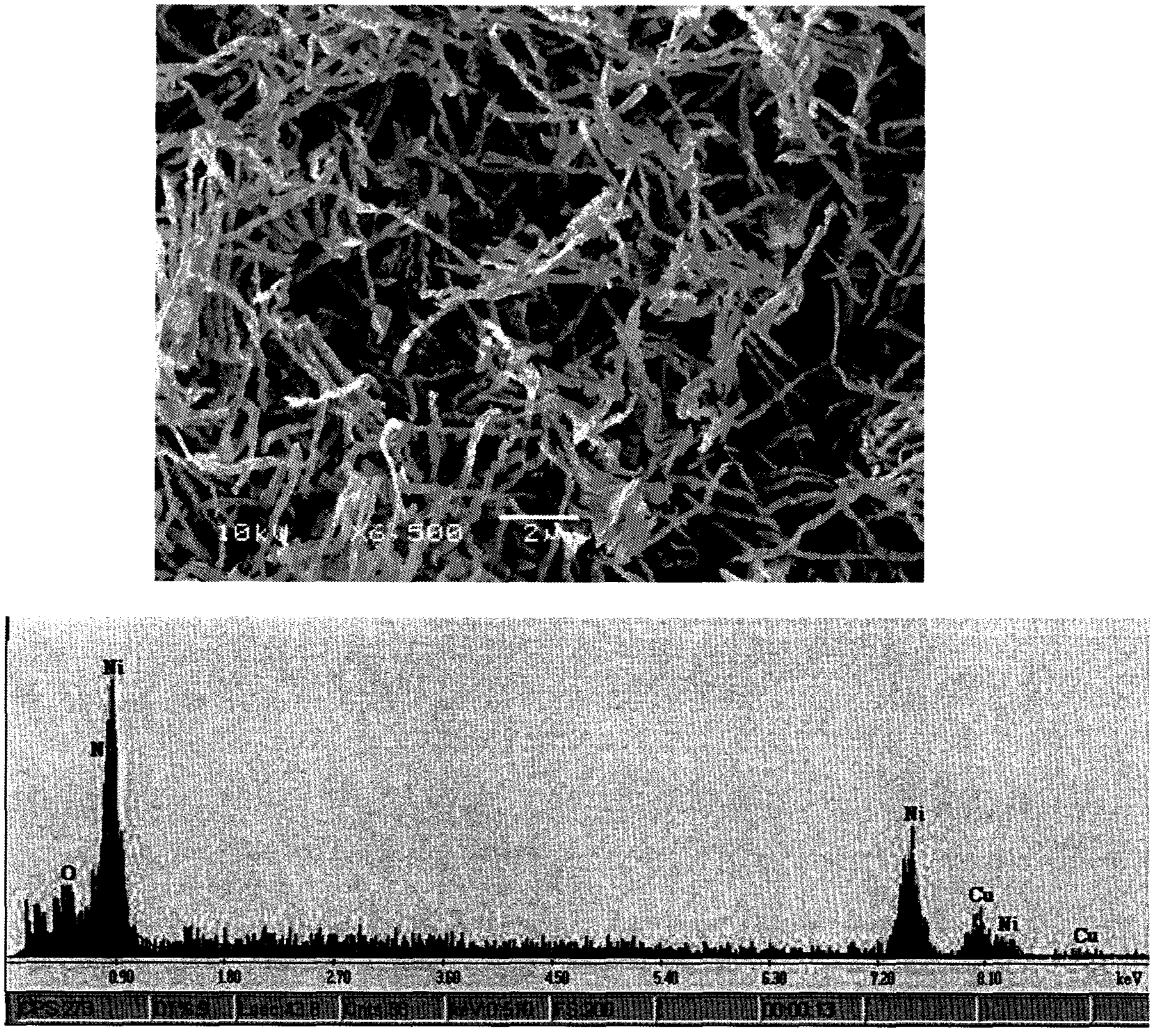

Figure 4.8 SEM images and EDAX spectrum of free standing Ni-Cu alloy nanowires. The atomic ratio of Ni:Cu was 2:1. The length was about 2 μm and the diameter was 100 nm.

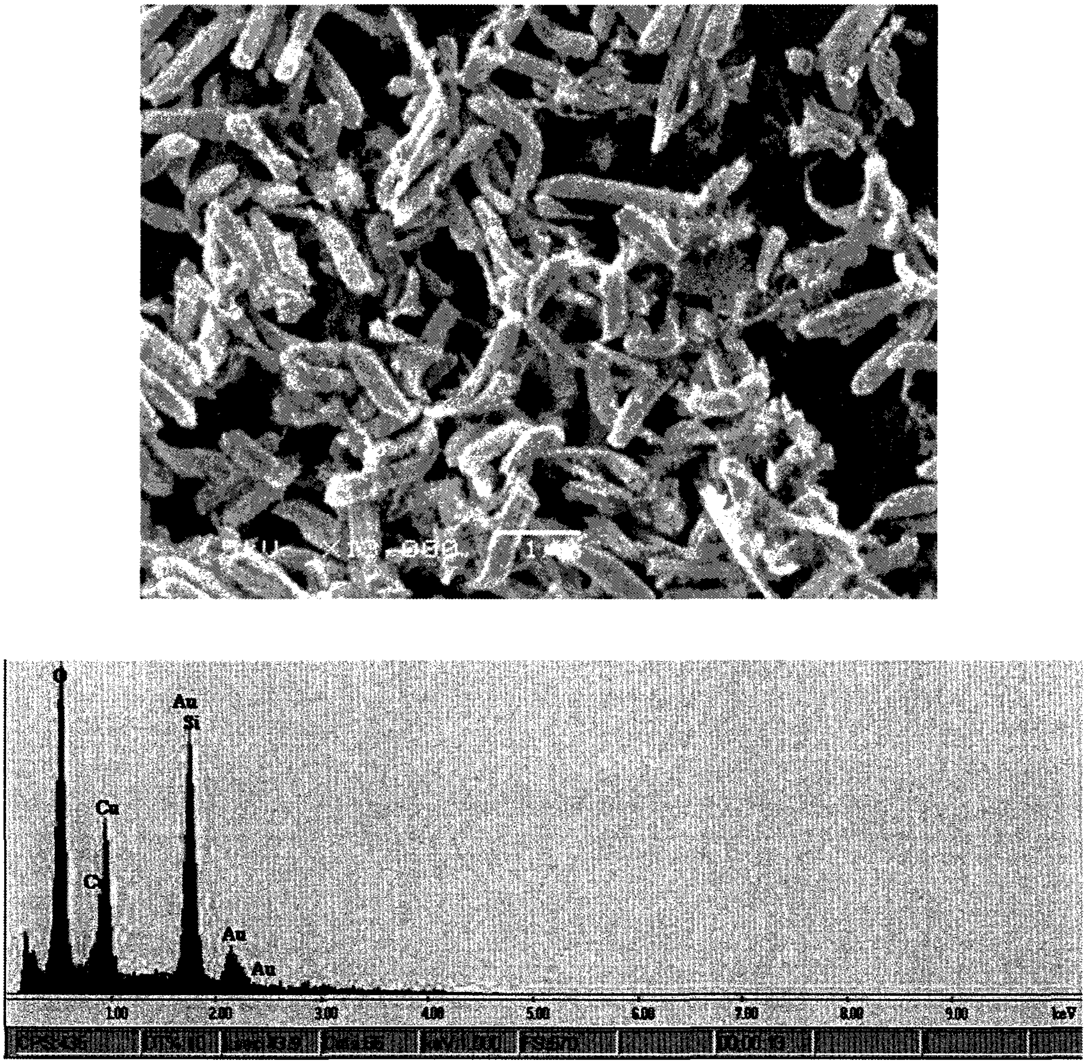

Figure 4.9 SEM images and EDAX spectrum of free standing Au-Cu alloy nanowires. The atomic ratio of Au:Cu was 1:2. The length was about 1 μm and the diameter was 250 nm.

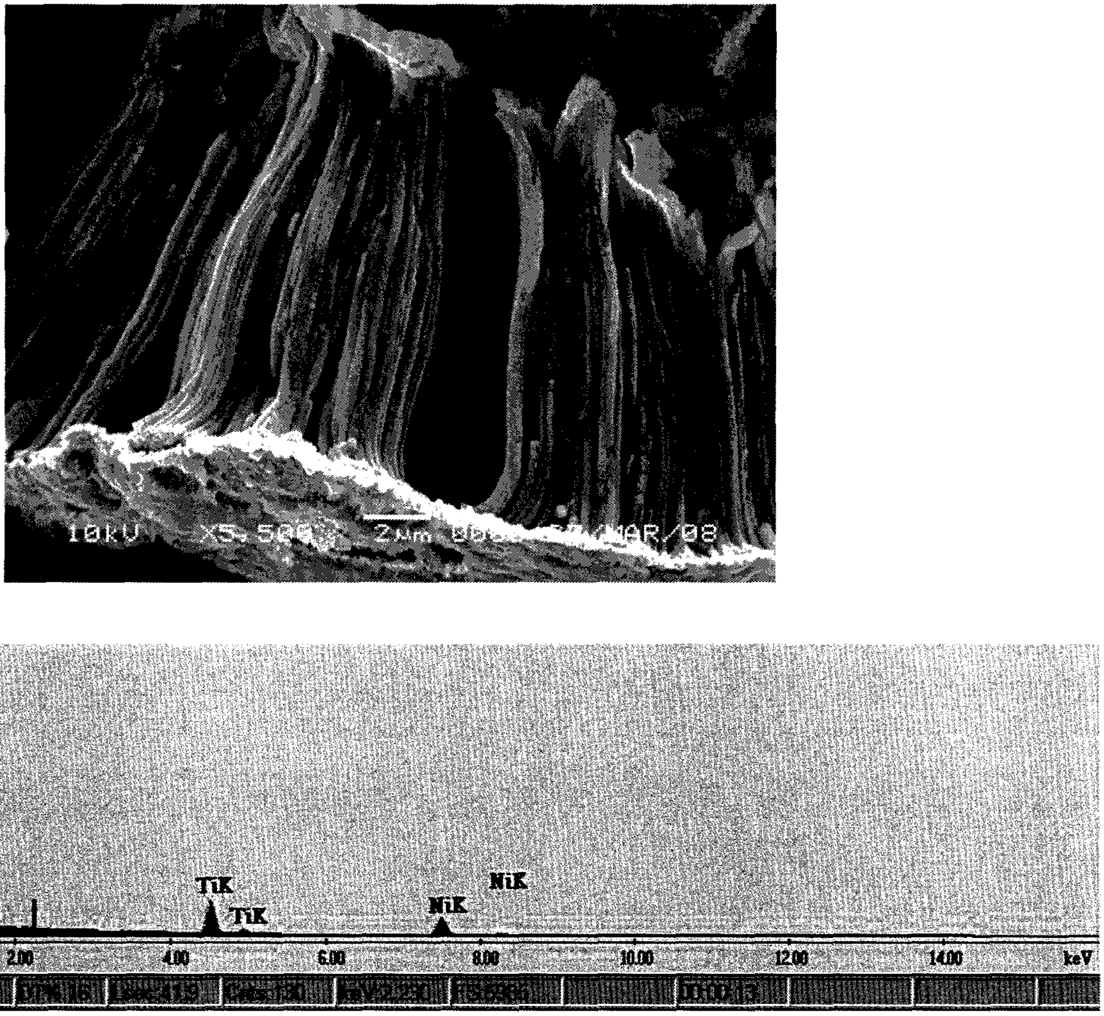

Figure 4.10 SEM image, EDAX spectrum of Ti-Ni alloy nanowires array. The atomic ratio of Ti:Ni was 1:1. The length was about 14 μm and the diameter was 200 nm.

3.4 Fluorescence on FMN coated Ni nanowires

The integration of biomolecules with nanostructured materials is significant toward advances in bionanotechnology, where it is often required to develop materials that are biocompatible and can interact selectively with biological entities. Reich[14] and Meyer[22] introduced hydrophilic and hydrophobic groups to different segments of a nanowire to produce multi-functionality. Surface functionalization of nanoparticles or nanowires has potential applications in disrupting protein-protein interactions, regulating DNA transcription, gene transfection, etc[23, 24]. Here, we demonstrate the functionalization of a fluorescent biomolecule onto magnetic Ni nanowire surface.

Flavin mononucleotide (FMN) is important in regulating biological processes such as electron transport. The phosphonic acid group in FMN is a hard Lewis base and therefore binds strongly to Ni which is a hard Lewis acid (Scheme 4.4). Figure 4.11a shows an optical microscope image of unfunctionalized Ni nanowires, while Figure 4.11b shows a fluorescence microscope image of FMN-functionalized Ni nanowires. The brightness shown in Figure 4.11b is due to the fluorescence of the FMN at the Ni surface.

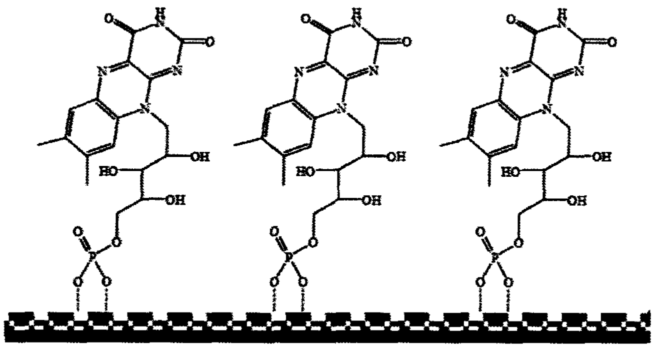

Scheme 4.4 Schematic illustration of FMN attaching to Ni surface through phosphonic acid group.

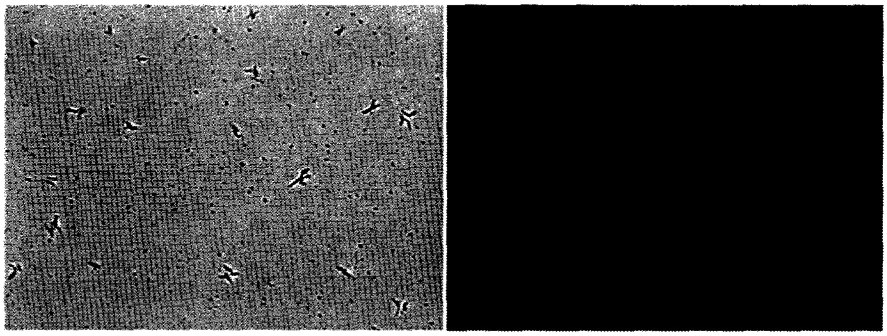

Figure 4.11 (a) Optical microscope image of Ni nanowires and (b) fluorescence microscope image of FMN functionalized Ni nanowires.

3.5 Magnetism of Ni-Au two component nanowires and biomolecule coated Ni nanowires

The Ni nanowires and the two-component nanowires containing Ni as one of the segments were found to be very sensitive to an applied magnetic field. In fact, the wires were easily attracted to a bar magnet in close proximity. Magnetic nanoparticles have potential applications as high recording density media, thermotherapy and in cell separation. The magnetic measurements for Ni nanowires 200 nm in diameter and 6 μm in length (Figure 4.12a) at different temperatures show hysteresis loops and the magnetic strength is not affected by temperature. Two component nanowires consisting of a Ni segment and a Au segment displayed comparable magnetization behavior as the nanowires consisting exclusively of Ni metal (Figure 4.12b and Table 4.2). The slight decrease in the saturation magnetization (M_s), coercivity (H_C) and remanence magnetization (M_r) may be due to Ni segment being short in length.

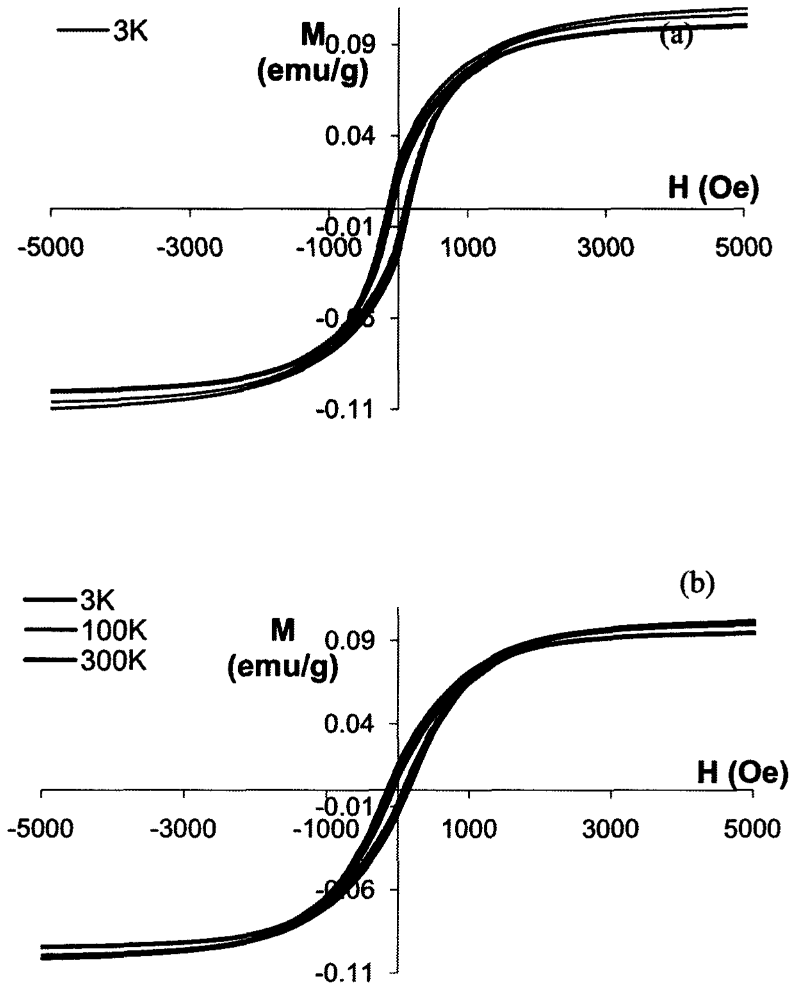

Figure 4.12 SQUID spectra of (a) Ni nanowires of 200 nm in diameter and 6 μm in length and (b) Ni-Au two component nanowires of 200 nm in diameter and 2 μm in length for Ni potion and 4 μm for Au portion. The spectra were recored at 3K, 100K and 300K.

Table 4.2 The saturated magnetization (M_s), hysteresis (H), and remanence magnetization (M_r) of Ni nanowires and Ni/Au nanowires in 3K, 100K and 300K.

	Ni nanowires			Ni/Au nanowires		
	M_s (emu/g)	H (Oe)	M_r (emu/g)	M_s (emu/g)	H (Oe)	M_r (emu/g)
3K	0.12	160	0.027	0.11	150	0.016
100K	0.11	140	0.022	0.10	110	0.011
300K	0.10	100	0.016	0.10	90	0.009

It is important to determine that the surface coverage by ligands will not decrease the magnetic strength of the nanowires, since the inherent magnetic properties are essential in biological applications, such as cell separation, bio-imaging, therapeutics and diagnosis. Therefore, in addition we examined the immobilization of folic acid, at the Ni nanowire surface. Folic acid is an important molecule with biological activity. It is highly expressed in most cancer cells by being involved in one-carbon transfer reactions that are important in DNA synthesis and replication, cell division and growth[25]. Folic acid is essential for the rapid proliferation of malignant cells[26, 27]. Folic acid has been used for receptor-targeted drug delivery[26, 28-39]. Folic acid has a terminal carboxylic acid group which is also a hard base and therefore binds to the Ni which is a hard acid[40, 41]. Figure 4.13 exhibits the SQUID hysteresis curve of Ni nanowires after surface functionalization with folic acid. Remanence magnetization (the magnetization that persists even when the field decreases to 0 Oe) is 35% of the saturated magnetization when the field was absent. We also have observed highly enhanced coercivitiy of 250 Oe, which should be compared with the value of a few tens of oersteds for bulk Ni. The coercivity agrees well with the reported magnetism of bare Ni nanowires[6], where the nanowires were aligned parallel to the external magnetic field. These results show that the magnetic properties of Ni nanowires are not affected by surface functionalization.

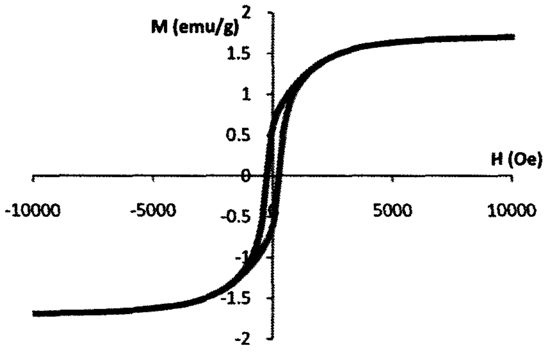

Figure 4.13 Magnetism measurement of folic acid-functionalized Ni nanowires.

4. Summary

Metallic nanowires with controlled diameter and aspect ratios were grown in AAO membranes using a facile electrochemical deposition method. The morphology and structure of the metallic nanowires could be manipulated by tuning the synthetic parameters such as deposition time, electrolyte concentration, deposition voltage or current, or the pore size of the membrane. Bi-segmented or multi-segmented nanowires were accomplished by electrodepositing one metal, then switching the electrolyte solution in order to grow another segment on top of the other. Alloy nanowires were fabricated by simultaneously reducing two electrolytes under an appropriate voltage. Binding with organic molecule through hard base and acid interaction provides surface functionalization to nanowires. The magnetic properties of Ni nanowires were unaffected by functionalizing their surface with small biomolecules.

5. References

1. Martin, C. R., Membrane-Based Synthesis of Nanomaterials. Chemistry of Materials 1996, 8, 1739-1746.

2. Murphy, C. J.; Gole, A. M.; Hunyadi, S. E.; Stone, J. W.; Sisco, P. N.; Alkilany, A.; Kinard, B. E.; Hankins, P., Chemical sensing and imaging with metallic nanorods. Chemical Communications 2008, (5), 544-557.

3. Cai, Z. H.; Martin, C. R., Electronically Conductive Polymer Fibers with Mesoscopic Diameters Show Enhanced Electronic Conductivities. Journal of the American Chemical Society 1989, 111, (11), 4138-4139.

4. Liang, L.; Liu, J.; Windisch, C. F.; Exarhos, G. J.; Lin, Y. H., Direct Assembly of Large Arrays of Oriented Conducting Polymer Nanowires. Angewandte Chemie-International Edition 2002, 114, (19), 3665-3668.

5. Wu, C. G.; Bein, T., Conduting polyaniline filaments in a mesoporous channel host. Science 1994, 264, (5166), 1757-1759.

6. Whitney, T. M.; Jiang, J. S.; Searson, P. C.; Chien, C. L., Fabrication and magnetic-properties of arrays of metallic nanowires. Science 1993, 261, (5126), 1316-1319.

7. Karpinski, Z. J.; Osteryoung, R. A., Short-time pulse voltammetric studies of fast heterogeneous electron-transfer reactions. Journal of Electroanalytical Chemistry 1993, 349, (1-2), 285-297.

8. Ishii, S.; Sadki, W. S.; Ooi, S.; Ochiai, Y.; Hirata, K., Superconducting properties of lead nanowires frabricated by electrochemical deposition. Physica C 2005, 426-431, 268-272.

9. Martin, C. R., Nanomaterials - a membrane-based synthetic approach. Science 1994, 266, (5193), 1961-1966.

10. Hulteen, J. C.; Martin, C. R., J. Mater. Chem 1997, 7, 1075.

11. Collinson, M. M., Electrochemistry: An Important Tool To Study and Create New Sol-Gel-Derived Materials. Accounts of Chemical Research 2007.

12. Tanase, M.; Bauer, L. A.; Hultgren, A.; Silevitch, D. M.; Sun, L.; Reich, D. H.; Searson, P. C.; Meyer, G. J., Magnetic alignment of fluorescent nanowires. Nano Letters 2001, 1, (3), 155-158.

13. Jain, T. K.; Moralles, M. A.; Sahoo, S. K.; Lesllie-Pellecky, D. L.; Labhasetwar, V., Iron oxide nanoparticles for sustained delivery of anticancer agents. Molecular Pharmaceutics 2005, 2, (3), 194-205.

14. Reich, D. H.; Tanase, M.; Hultgren, A., Biological Applications of Multifunctional Magnetic Nanowires (invited). Journal of Applied Physics 2002, 93, (10), 7275-7280.

15. Wirtz, M.; Martin, C. R., Template-fabricated gold nanowires and nanotubes. Advanced Materials 2003, 15, (5), 455-458.

16. Liang, W. B.; Martin, C. R., Template-synthesized polyacetylene fibrils show enhanced supermolecular order. Journal of the American Chemical Society 1990, 112, (26), 9666-9668.

17. Che, G. L.; Lakshmi, B. B.; Fisher, E. R.; Martin, C. R., Carbon nanotubule membranes for electrochemical energy storage and production. Nature 1998, 393, (6683), 346-349.

18. Marinakos, S. M.; Brousseau, L. C.; Jones, A.; Feldheim, D. L., Template synthesis of one-dimensional Au, Au-poly(pyrrole), and poly(pyrrole) nanoparticle arrays. Chemistry of Materials 1998, 10, (5), 1214-1219.

19. Routkevitchi, D.; Chan, J.; Xu, J. M.; Moskovits, M., Proc. Electrochem. Soc 1997, 97, (7), 350.

20. Valizadeh, S.; Hultman, L.; George, J. M.; Leisner, P., Template Synthesis of Au/Co Multilayered Nanowires by Electrochemical Deposition. Advanced Functional Materials 2002, 12, (11-12), 766-772.

21. Huang, C.; Hao, Y., The fabrication of short metallic nanotubes by templated electrodeposition. nanotechnology 2009, 20, 445607.

22. Bauer, L. A.; Reich, D. H.; Meyer, G. J., Selective functionalization of two-component magnetic nanowires. Langmuir 2003, 19, (17), 7043-7048.

23. You, C. C.; Chompoosor, A.; Rotello, V. M., The biomacromolecule-nanoparticle interface. Nano Today 2007, 2, (3), 34-43.

24. You, C. C.; Verma, A.; Rotello, V. M., Engineering the nanoparticle-biomacromolecule interface. Soft Matter 2006, 2, (3), 190-204.

25. Ross, J. F.; Chaudhuri, P. K.; Ratnam, M., Differential regulation of folate receptor isoforms in normal and malignant-tissues in-vivo and in established cell-lines - physiological and clinical implications. Cancer 1994, 73, (9), 2432-2443.

26. Kelemen, L. E., The role of folate receptor alpha in cancer development, progression and treatment: Cause, consequence or innocent bystander? International Journal of Cancer 2006, 119, (2), 243-250.

27. Hartmann, L. C.; Keeney, G. L.; Lingle, W. L.; Christianson, T. J. H.; Varghese, B.; Hillman, D.; Oberg, A. L.; Low, P. S., Folate receptor overexpression is associated with poor outcome in breast cancer. International Journal of Cancer 2007, 121, (5), 938-942.

28. Sudimack, J.; Lee, R. J., Targeted drug delivery via the folate receptor. Advanced Drug Delivery Reviews 2000, 41, (2), 147-162.

29. Low, P. S.; Antony, A. C., Folate receptor-targeted drugs for cancer and inflammatory diseases - Preface. Advanced Drug Delivery Reviews 2004, 56, (8), 1055-1058.

30. Lu, Y. J.; Sega, E.; Leamon, C. P.; Low, P. S., Folate receptor-targeted immunotherapy of cancer: mechanism and therapeutic potential. Advanced Drug Delivery Reviews 2004, 56, (8), 1161-1176.

31. Sonvico, F.; Mornet, S.; Vasseur, S.; Dubernet, C.; Jaillard, D.; Degrouard, J.; Hoebeke, J.; Duguet, E.; Colombo, P.; Couvreur, P., Folate-conjugated iron oxide nanoparticles for solid tumor targeting as potential specific magnetic hyperthermia mediators: Synthesis, physicochemical characterization, and in vitro experiments. Bioconjugate Chemistry 2005, 16, (5), 1181-1188.

32. Lu, Y. J.; Low, P. S., Folate-mediated delivery of macromolecular anticancer therapeutic agents. Advanced Drug Delivery Reviews 2002, 54, (5), 675-693.

33. Reddy, J. A.; Low, P. S., Folate-mediated targeting of therapeutic and imaging agents to cancers. Critical Reviews in Therapeutic Drug Carrier Systems 1998, 15, (6), 587-627.

34. Torchilin, V. P. In Drug targeting, 2000; Elsevier Science Bv: 2000; pp S81-S91.

35. Stella, B.; Arpicco, S.; Peracchia, M. T.; Desmaele, D.; Hoebeke, J.; Renoir, M.; D'Angelo, J.; Cattel, L.; Couvreur, P., Design of folic acid-conjugated nanoparticles for drug targeting. Journal of Pharmaceutical Sciences 2000, 89, (11), 1452-1464.

36. Lai, T. Y.; Lee, W. C., Killing of cancer cell line by photoexcitation of folic acid-modified titanium dioxide nanoparticles. Journal of Photochemistry and Photobiology A-Chemistry 2009, 204, (2-3), 148-153.

37. Berry, C. C.; Curtis, A. S. G., Functionalisation of magnetic nanoparticles for applications in biomedicine. Journal of Physics D-Applied Physics 2003, 36, (13), R198-R206.

38. Quintana, A.; Raczka, E.; Piehler, L.; Lee, I.; Myc, A.; Majoros, I.; Patri, A. K.; Thomas, T.; Mule, J.; Baker, J. R., Design and function of a dendrimer-based therapeutic nanodevice targeted to tumor cells through the folate receptor. Pharmaceutical Research 2002, 19, (9), 1310-1316.

39. Leamon, C. P.; Low, P. S., Delivery of macromolecules into living cells - a method that exploits folate receptor endocytosis. Proceedings of the National Academy of Sciences of the United States of America 1991, 88, (13), 5572-5576.

40. Kalyanasundaram, K.; Vlachopoulos, N.; Krishnan, V.; Monnier, A.; Graetzel, M., Sensitization of titanium dioxide in the visible light region using zinc porphyrins. The Journal of Physical Chemistry 1987, 91, (9), 2342-2347.

41. Kamat, P. V.; Fox, M. A., Photosensitization of TiO2 colloids by Erythrosin B in acetonitrile Chemical Physics Letters 1983, 102, (4), 379-384.

CHAPTER V

SYNTHESIS, CHARACTERIZATION AND MAGNETISM OF METALLIC PALLADIUM AND BIMETALLIC PALLADIUM-RUTHENIUM NANOWIRES

1. Introduction

Magnetic materials are important for a wide range of applications including data recording, magnetic resonance imaging, cell separation, drug and gene delivery, and as biosensors. One of the interesting findings we sought to study is to understand how magnetism was affected within the nanowire size regime.

Magnetism in materials is ascribed to the presence of unpaired electrons in the atomic structure of magnetic materials. Electron spinning creates a magnetic moment with 1 Bohr magneton, μ_B. Spinning in the opposite orientation in paired electrons cancel out the magnetic moments. Unpaired electrons induce magnetic moments to the *3d* elements Fe, Co, and Ni. In the bulk form, the delocalization of the atomic orbitals disperses distinct energy levels to the energy bands. But unlike *4s* orbitals, the inner *3d* orbital have a certain degree of localization (partial delocalization), which could induce a magnetic moment. A recent study showed that magnetic moments was greatly enhanced in nanoscale clusters[1]. It was found that the cluster size affected the magnetism due to the quantity of surface atoms[1]. In the center of the bulk, the electrons spin in a random direction, therefore, the disordered arrangement counteracts the overall magnetic moment. The surface atoms have reduced number of nearest neighbors, which causes the *3d* electrons to be more localized in comparison delocalization in bulk center. It was suggested that the surface atoms are atom-like and the deeper layers atoms are bulk-like.

In the bulk form, *4d* elements, like Pd and Ru do not exhibit any magnetic moment, although they have very similar electronic configurations with the 3*d* magnetic elements Ni and Fe, respectively. The Pd atom has a nearly closed shell with a $4d^{10-\xi}5s^{\xi}$ electronic configuration, where $\xi \approx 0$, while Ru has a $4d^7 5s^1$ configuration, where an open 4*d* shell has magnetic moments of 3 μ_B.[2] It is reasonable to expect Pd and Ru to show magnetic moments at the nanoscale, since previous theoretical calculations and experimental data have showed the existence of magnetism in nanoscale Ru and Pd[3-9].

Theoretical calculations on 4*d* transition metals (particularly Pd clusters) have proposed the existence of magnetism in low dimensional systems, such as clusters, nanowires or ultrathin films[2, 5, 10]. For instance, 13-atom clusters of 4*d* elements were theoretically expected to possess magnetic moments as a result of the reduced dimensionality and the enhanced electronic degeneracy due to the symmetry of the cluster[11]. Small Pd_{13} clusters were observed to exhibit ferromagnetism, while Rh_{13} and Ru_{13} clusters were partially magnetic, with an antiferromagnetic orientation of the moments on the central atoms in Ru clusters[11, 12]. The large spin-orbit coupling and their orbital moments are quenched in the solid. The ferromagnetic ordering was assumed to lie only in the top most layer of the particle surface, while the rest of the particle remains diamagnetic, as in the Pd bulk[13].

Experimental data that has been reported showed that the magnetism of Ru and Pd depends on the size of cluster. Appearance of magnetic moment in Pd clusters with diameter less than 14 nm was observed, which was ascribed to the ferromagnetism of surface atoms[6-9, 14, 15]. For example, Pd nanoparticles containing 500 atoms (2.4 nm size) inside the apoferritin cavity exhibit permanent magnetism up to room temperature[16]. Even thin films of Pd may exhibit an irregular magnetic behavior as a function of film thickness[17, 18]. For nanosized films, fruitful experimental and calculated results verify the ferromagnetism of Ru and Pd when deposited on the noble metal substrates.

Experimental studies to measure the magnetism of Pd-Ru bimetallic alloy nanowires have not been reported. In this chapter we will investigate the magnetism that arises in anisotropic nanowires made of Pd or Ru alone, and Pd-Ru alloy to study the effect of localization of large amount surface electrons on magnetism.

2. Experimental details

Materials. Anodic aluminum oxide (AAO) membranes (Whatman) were purchased from VWR. Ru plating solution (Ruthenium U concentrated @ 20 g/L) was purchased from Technic Inc. Palladium (II) chloride (5 wt. % solution in 10 wt. % HCl) was obtained from Sigma Aldrich Company. Sodium hydroxide, methanol and other solvents were procured from VWR.

2.1 Synthesis of Pd, Ru and Pd-Ru alloy nanowires

Scheme 4.2 in chapter IV shows the experimental setup for making Ru and Pd nanowires. Briefly, one surface of an AAO membrane was sputter coated with a thin film of gold, and was attached to an ITO coated glass slide to serve as the working electrode. Platinum gauze was used as both reference electrode and counter electrode. Ru plating solution was 0.04 M Ru salt aqueous solution. Pd plating solution was 0.03 M for $PdCl_3$ aqueous solution. Pd-Ru alloy plating solution consisted of an aqueous solution of 0.003 M Pd salt and 0.01 M Ru salt. For all three kinds of nanowires, 3 mA constant current was applied for the reduction of metal salts, which deposited on the bottom of the membrane channel. After deposition, the alumina was dissolved in 6M NaOH solution, releasing the nanowires from the membranes. In the water suspension, the nanowires could be collected by centrifugation, washed with milli-Q water (Millipore) five times, and twice in 70% ethanol before drying in the vacuum.

2.2 Characterization of Pd, Ru and Pd-Ru alloy nanowires

Scanning Electron Microscopy (SEM) and Energy Dispersive X-ray analysis (EDAX). The nanowires were imaged by SEM and their composition was analyzed by EDAX. 1μL of nanowires suspended in ethanol was placed on carbon tape and the tape was attached to an aluminum stub. The samples were allowed to dry before imaging. No additional conductive coating was required. The acceleration voltage was set to 3 kV and the working distance was set to 3 mm.

X-ray Diffraction measurement (XRD). XRD measurements for Pd or Ru nanowires were measured on a PANalytical X'Pert Pro Materials Research Diffractometer (MRD) in Bragg-Brentano geometry. For the incident beam path, the fixed divergence and the anti scatter slits were ¼ ° and ½ °, respectively, with a 0.04

radian Soller slit and a 10 mm beam mask. For the diffracted beam path, the RTMS (real time multi-strips) X'Celerator detector was equipped with a 0.04 radian Soller slits, a 5 mm anti scatter slit and a Ni filter. The detector active length was 2.122°. Samples were placed on a Si (111) wafer. Pd nanowires were scanned in a symmetric mode with a step size of 0.05° at 1 min/step. The scan range at 2θ was 35-60°. The x-ray radiation source was Cu $K\alpha_1$, $\lambda = 1.5406$ Å. Phase analysis was performed with the X'Pert High Score Plus and the MDI JADE+ software and with the ICDD PDF-2 release 2006 database.

Pd-Ru bimetallic alloy nanowires were scanned in a symmetric mode with a step size of 0.03° at 2 min/step. The scan range at 2θ was 33-90°. For the incident beam path, a hybrid mirror/monochromator and a capillary anti scatter attachment with a ½° divergence slit was used. The sample was placed in a capillary spinner sample stage. In the diffracted beam path, the RTMS (real time multi-strips) X'Celerator detector was equipped with an anti scatter shield (no Soller slits).

2.3 Magnetism measurement of Pd, Ru and Pd-Ru alloy nanowires

Superconducting QUantum Interference Device (SQUIDs) measurements were employed to determine the magnetism of nanowires at different temperatures. A SQUID magnetometer (Quantum Design, MPMS7) was used to record both hysteresis loops (*M-H* curves)[7]. The very small diamagnetic contribution of the plastic container had a negligible effect on the overall magnetization, which was dominated by the sample. The molar magnetic susceptibilities were corrected for the diamagnetism of the container. *M-H* curves were taken at 3K, 100K, and 300K for each sample. The saturation magnetization (*M_s)*, remanence magnetization (*M_r*) and the coercive field (*H_C*) was determined[19].

3. Results and discussion

3.1 Synthesis and characterization of Pd, Ru and Pd-Ru nanowires

Electrochemical deposition was used to fabricate Pd, Ru and Pd-Ru nanowires. The nanowires produced by this method were monodisperse and were either vertically orderly aligned on a substrate or were free standing in solution. Control of the nanowire length was accomplished by monitoring the pore-filling process (time *vs*. current) as illustrated in Scheme 4.3 in chapter IV[20]. Diameters are dependent on the selective membrane pore size. The advantage of using electrodeposition to obtain nanowires is that the nanowires are always continuous and have good crystalline structures. Figure 5.1a shows Pd nanowires with diameter and length of 200 nm and 2 ~ 4 μm, respectively. EDAX spectrum (Figure 5.1b) illustrates that the Pd nanowires consisted of Pd metal. The C signal comes from the carbon tape that holds the sample. The XRD spectrum (Figure 5.1c) reveals the crystallinity of Pd nanowires. There are five obvious peaks at 2θ = 40.14, 46.67, 67.83, 81.66, and 85.95 that represent the (111), (200), (220), (311) and (222) lattice, respectively. (111) and (200) lattice have *d* values of 2.2448 Å and 1.9449 Å. These are typical for *fcc* crystalline structure of Pd. Figure 5.2a displays Ru nanowires with diameter and length of 200 nm and 2 μm, respectively. The nanowires consist of primarily Ru metal (indicated by the EDAX spectrum in Figure 5.2b) with polymorphous microstructure (indicated from XRD spectrum in Figure 5.2c).

Pd-Ru alloy nanowires were made by the simultaneous reduction of two metal salts in an electrochemical deposition process. A one hour deposition process resulted in Pd-Ru bimetallic alloy nanowires with a diameter of 200 nm and a length of 3μm (Figure 5.3a). The careful control of the concentration ratio of two metal salts resulted in 1:1 ratio of Pd:Ru, which could be confirmed by the EDAX spectrum (the Si and O signals arise from the silicon wafer that serves as the sample holder) shown in Figure 5.3b. As indicated in the XRD spectrum (Figure 5.3c), the signals are dominated by the *fcc* structural feature of Pd nanowires rather than the hexagonal packed crystal structure that is typical of Ru.

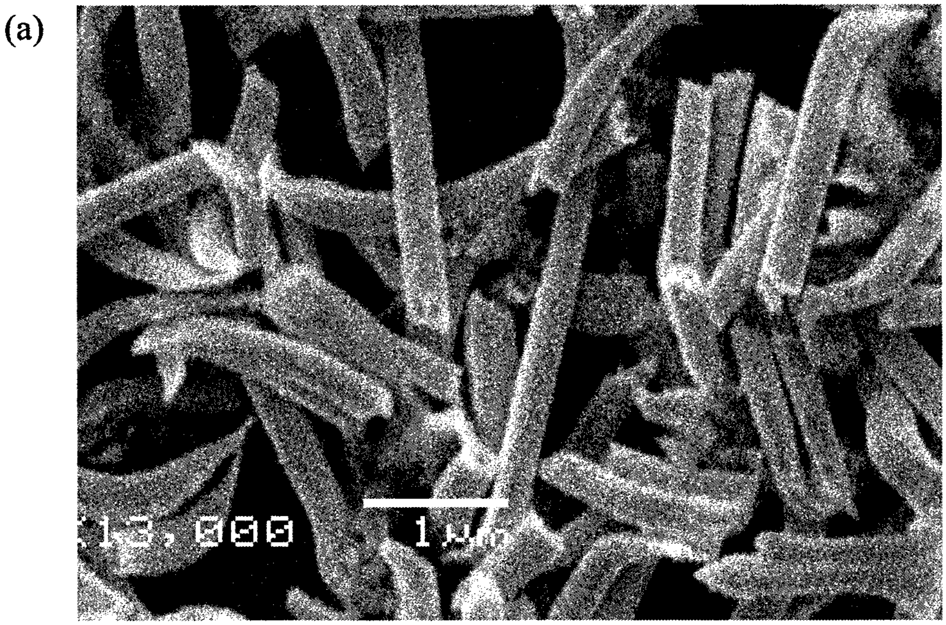

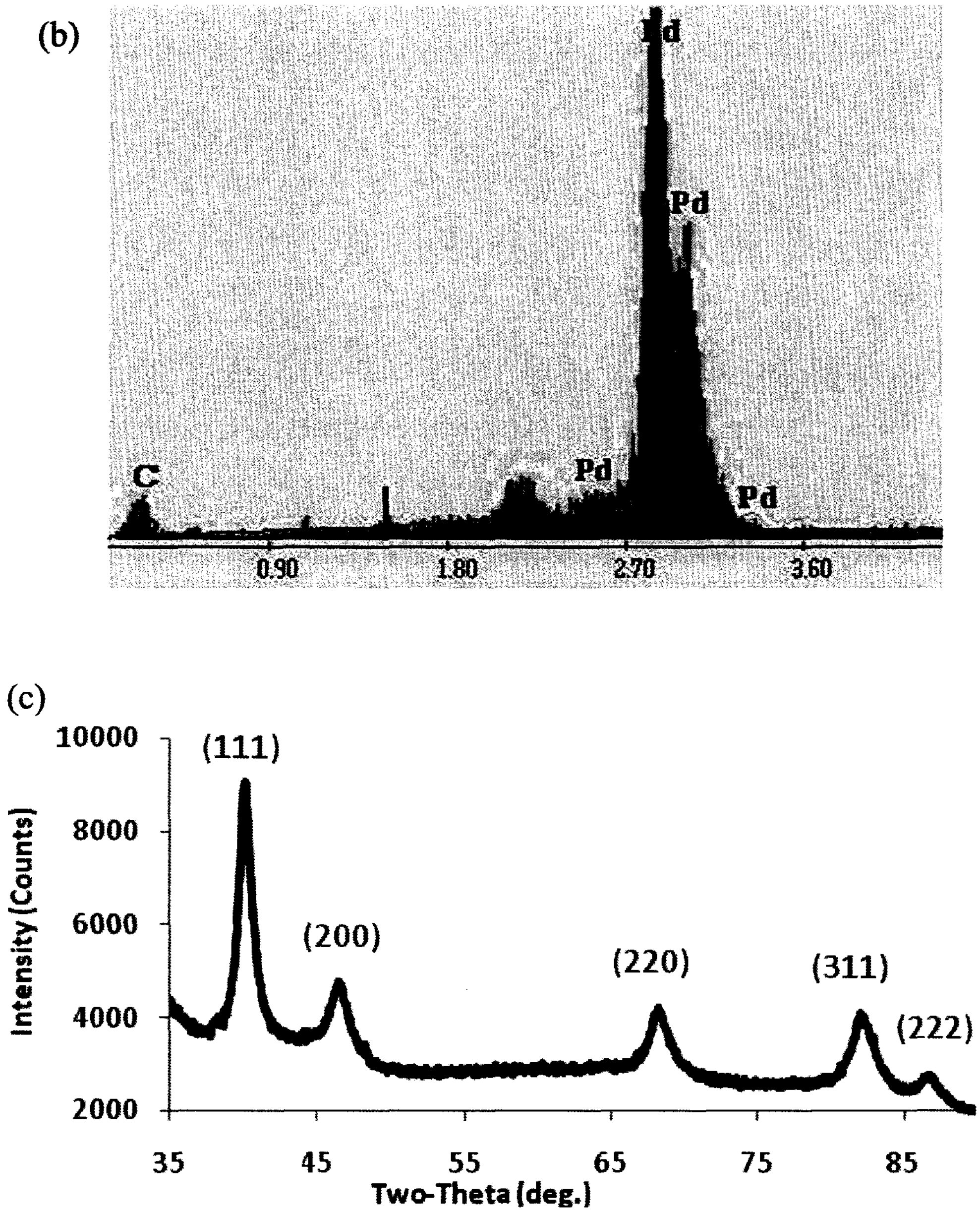

Figure 5.1 SEM image (a), EDAX spectrum (b), and XRD spectrum (c) of Pd nanowires. The nanowires were made in plating solution containing 0.03 M $PdCl_2$. The applied current was 3 mA for 1 hour.

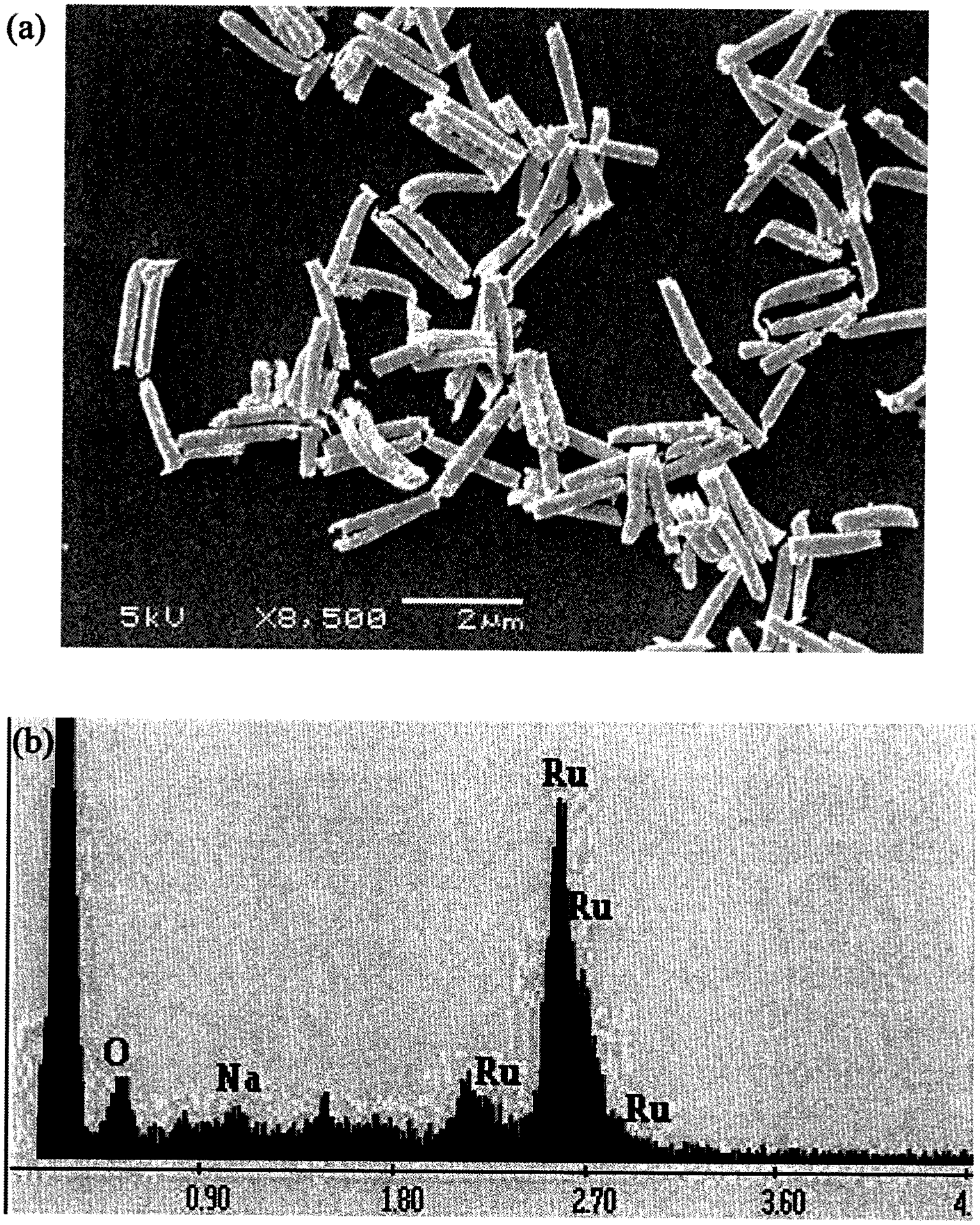
(a)
5kV
X8,500
2 μm
(b)
Ru
Ru
O
Na
Ru
Ru
0.90
1.80
2.70
3.60
4.

(c)

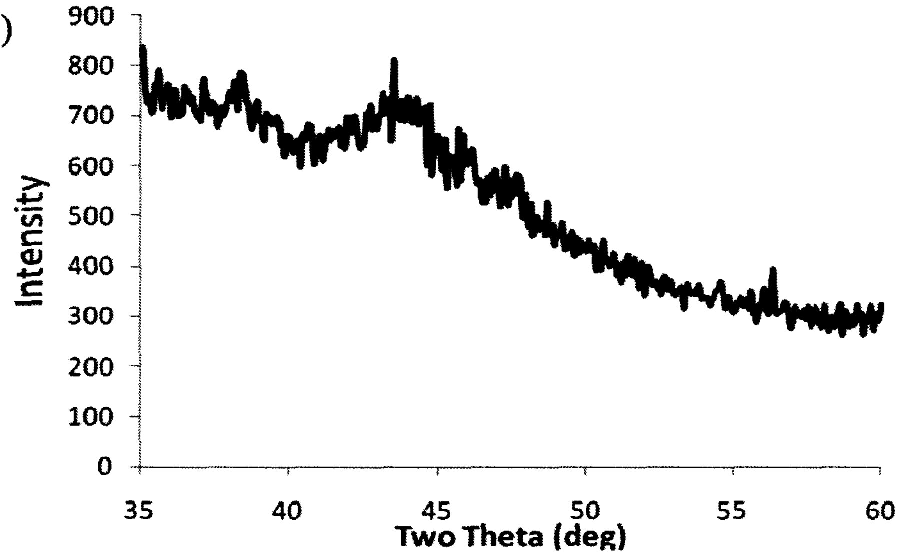

Figure 5.2 SEM image (a), EDAX spectrum (b), and XRD spectrum (c) of Ru nanowires. The nanowires were made in plating solution containing 0.04 M ruthenium ions. The applied current was 3 mA for 1 hour. In XRD, (101) diffraction at $2\theta = 43.3°$ is weak.

(a)

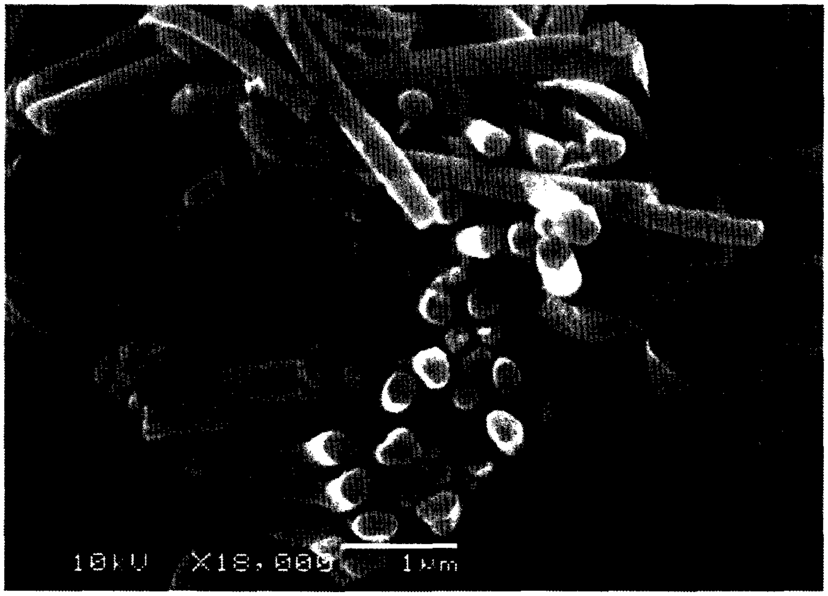

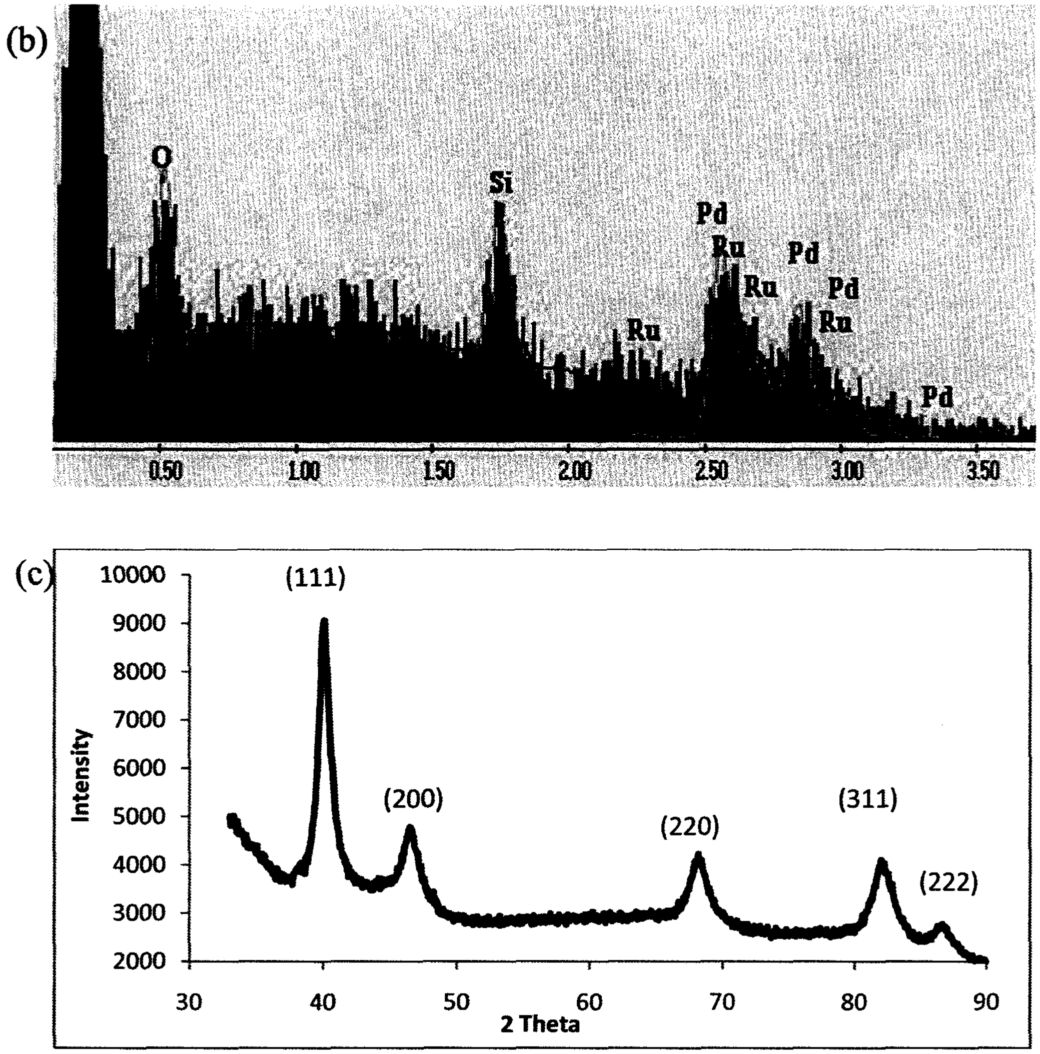

Figure 5.3 SEM images (a), EDAX spectrum (b), and XRD spectrum (c) of Pd-Ru alloy nanowires. The alloy nanowires were made in plating solution containing 0.003 M $PdCl_2$ and 0.02 M Ruthenium ions. The applied current was 3 mA for 1 hour.

3.2 Magnetic characterization

In nanoparticles, magnetization increases rapidly with decreasing particle size. Reports have suggested that only the surface monolayers of Pd nanoparticles are magnetic[6, 8]. However, it is not expected that Pd nanowires with diameters as large as 200 nm would exhibit magnetism. Figure 5.4a shows the magnetic hysteresis for Pd nanowires at low temperature of 3K. At temperatures of 100K or 300K, the Pd nanowires exhibit paramagnetic properties due to the thermal disorder of the alignment of local atomic magnetic moments which are induced by temperature dependant phenomena (Scheme 5.1a). Although local magnetic moments are insensitive to temperature, loss of alignment of local magnetic moments caused by thermal disorder may induce the disappearance in the magnetic moment when the external magnetic field is absent. While at low temperature, as illustrated in Scheme 5.1b, the high aspect ratio of Pd nanowire favors the local magnetic moment to be arranged in one direction relative to the other, resulting in a dipole moment in axial direction[21].

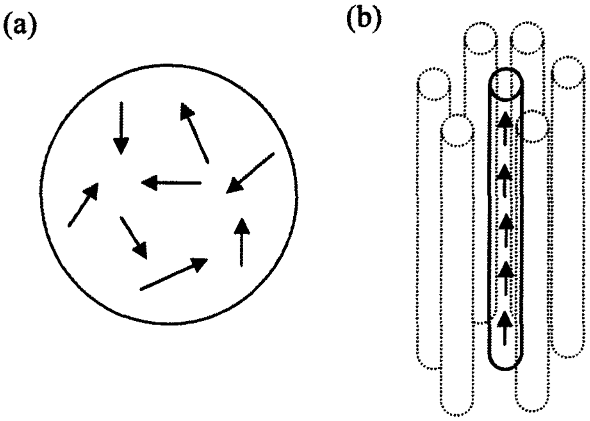

Scheme 5.1 (a) Overall magnetic moment is temperature dependent due to the thermal disorder of magnetic moment arrangement. (b) The anisotropic geometry of nanowire facilities the spinning of electron in parallel direction.

According to experimental and theoretical calculations, magnetism can occur in *hcp* (hexagonal close-packed) Pd films, *fcc* twinned Pd nanoparticles, and Pd atomic strands. Free-standing nanowires made by Pd exhibits *fcc* crystallinity, and display coercivity (H_c), saturation magnetization (M_s) and remnant magnetization (M_r) (Figure 5.4a). The value of H_c, M_s and M_r are extracted and provided in Table 5.1. Non-zero magnetic moments observed in the *M-T* curve support a ferromagnetic spin ordering in Pd nanowires.

Both lattice structure and the local chemical environment are factors that affect magnetism (either induce or quench the magnetism)[9, 22]. Surface electronic structure plays a dominant role in tuning the magnetic properties, especially for very small particles with diameters below 5 nm. This is due to the very high percentage of atoms located at the particle surface. The electronic structure of surface atoms is characterized by disorder, because of the missing bonds and local variation in the number of atomic neighbors, and a reduction of lattice symmetry with respect to the core of the particle. Their attributions are crucial to the magnitude of magnetization, which could also explain the enhanced or emerged magnetism of nanomagnets.

It was reported that Ru clusters (such as Ru_{13}) were partially magnetic[12], with an antiferromagnetic orientation of the moment on the central atom in Ru cluster. In materials that exhibit antiferromagnetism, the spin of the electrons points in opposite directions relative to neighboring electrons (Scheme 5.2). The ordered allignment gives zero magnetic moment overall. The magnetization curve of Ru nanowires (Figure 5.4b) did not show any hysteresis loop, but instead showed a linear relationship with the magnetic field. The magnetic behavior of 3*d* electrons is known to be sensitive to the lattice structure and to the local environment[22, 23]. Therefore, the polymorphous structure observed in the Ru nanowires could be responsible for the zero magnetic moment.

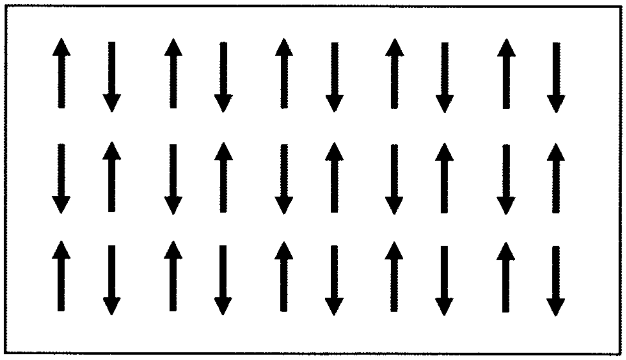

Scheme 5.2 The local magnetic moment arrangement in the center of antiferromagnetic materials.

The magnetism of Pd-Ru bimetallic alloy nanowires was measured under the same external magnetic field strength range. It was found that the induced magnetic moment of the sample was much smaller than that of Pd nanowires alone (Figure 5.4c and Table 5.1). This observation may due to the antiferromagnetic property of the Ru metal, which causes Ru to exhibit no magnetism. Therefore, the employment of non-magnetic metal weakens the magnetic properties of the Pd-Ru nanowires, which can be observed from the *M-H* curves at T = 3K. As listed in Table 5.1, the saturated magnetization (M_s) is estimated to be 0.00016 emu/g for Pd nanowires (at H = 1500 Oe), while M_s is 0.00014 emu/g for Pd-Ru nanowires at (H = 2000 Oe). The coercivity (H_C) value is 200 Oe for Pd nanowires, while H_C is 150 Oe for Pd-Ru bimetallic alloy nanowires. The remanence magnetization (M_r) for Pd-Ru alloy nanowires is lower than Pd nanowires as well.

We compared the magnetic properties of Pd-Ru bimetallic alloy nanowires to Pd-Ru bimetallic alloy nanoparticles. Surprisingly, the Pd-Ru bimetallic alloy nanoparticles showed no hysteresis features (Figure 5.5). The presence of thioether ligands at the surface of the Pd-Ru bimetallic alloy nanoparticles could have affected the *d* band structure, which may induce or quench the ferromagnetic character[24], while the clean surface of alloy nanowires is not affected due to the lack of surface ligands.

(a)

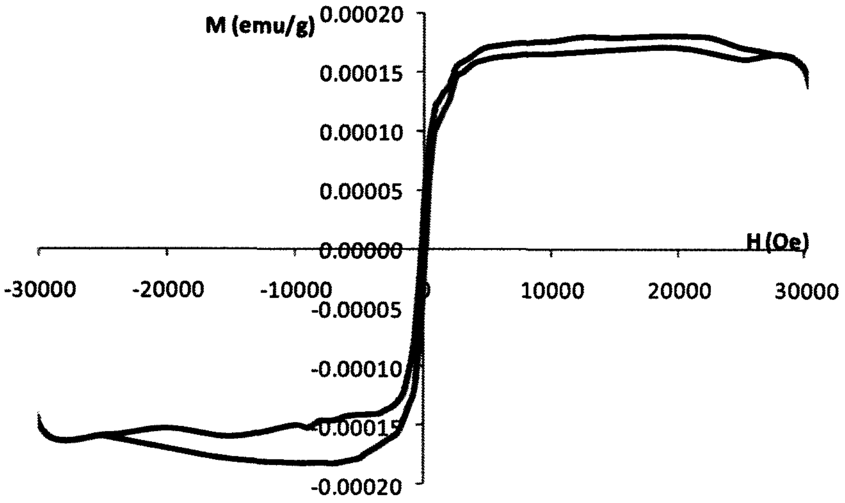
M (emu/g)
0.00020
0.00015
0.00010
0.00005
0.00000
-0.00005
-0.00010
-0.00015
-0.00020
H (Oe)
-30000
-20000
-10000
0
10000
20000
30000

(b)

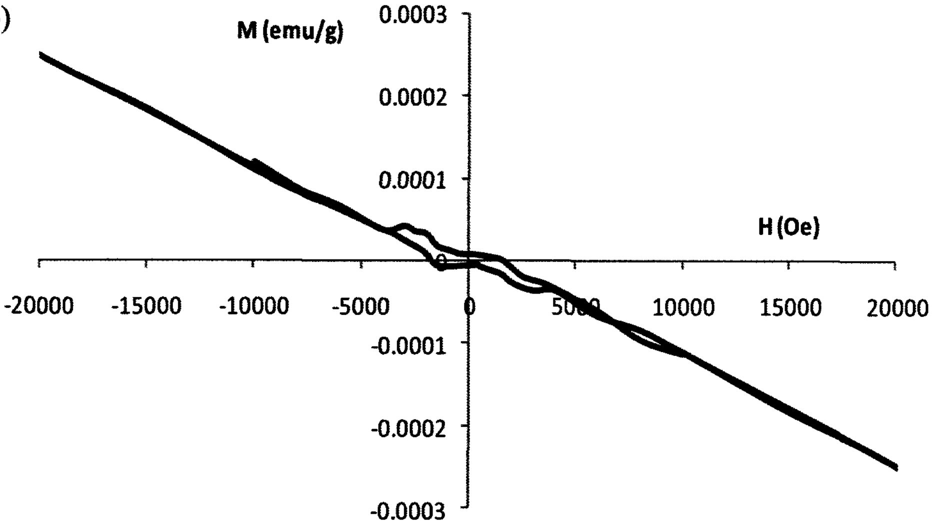
M (emu/g)
0.0003
0.0002
0.0001
0
-0.0001
-0.0002
-0.0003
H (Oe)
-20000
-15000
-10000
-5000
0
5000
10000
15000
20000

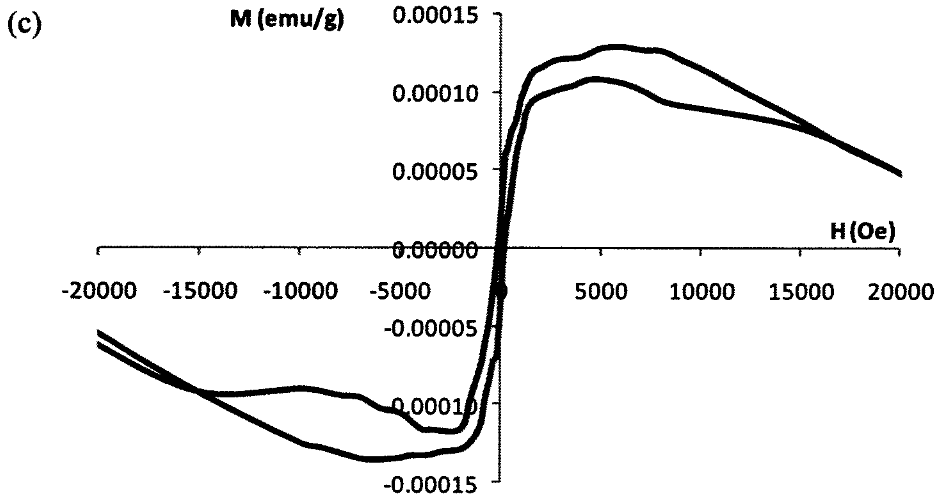

Figure 5.4 Magnetism measurements of (a) Pd, (b) Ru, and (c) Pd-Ru nanowires. Magnetization curves were recorded at low temperatures 3K. The x axis *H* is the magnetic field amplitude. The y axis *M* is the magnetization of the material.

Table 5.1 The coercivity (H_C), saturated magnetization (M_s) and the remanence magnetization (M_r) of the *fcc* Pd and Ru-Pd nanowires

Nanoparticles	T(K)	Coercivity (Oe)	Saturated magnetization (emu/g)	Remanence magnetization (emu/g)
Pd	3	200	0.00016	0.00004
Ru-Pd	3	150	0.00014	0.00003

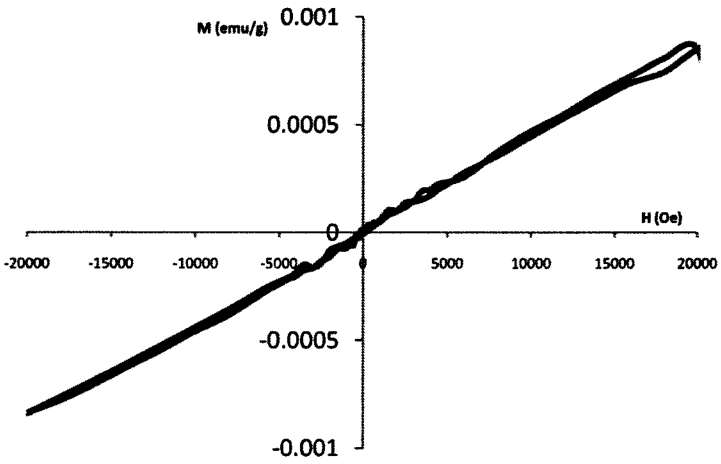

Figure 5.5 Paramagnetism of thioether Stabilized Pd-Ru alloy nanoparticles. Nanoparticles were coated with ligand *n*-dodecyl sulfide, Oe = Oersted.

4. Summary

Metal nanowires composed of Pd, Ru and Pd-Ru bimetallic alloy nanowires were synthesized by a template-based electrochemical deposition method. The electron rearrangements or redistribution determined by sizes, structural features, or composition are responsible for the nature of magnetic behavior of metal nanostructures[25]. The reduced coordination number of surface atoms gives rise to the localization of electrons opposing to the delocalization effect in the central atoms.[26] The presence of magnetism in Pd, Pd-Ru nanowires (or nanoparticles) may be attributed to the confinement effects associated with reduced coordination number of atoms in the surface.

5. References

1. Billas, I. M. L.; Chatelain, A.; Deheer, W. A., Magnetism from the atom to the bulk in iron, cobalt, and nickel clusters. *Science* **1994,** 265, (5179), 1682-1684.

2. Kumar, V.; Kawazoe, Y., Magnetism in clusters of non-magnetic elements: Pd, Rh, and Ru - Magnetism in clusters of non-magnetic elements. *The European Physical Journal D* **2003,** 24, 81-84.

3. Delin, A.; Tosatti, E.; Weht, R., Magnetism in atomic-size palladium contacts and nanowires. *Physical Review Letters* **2004,** 92, (5).

4. Kumar, V.; Kawazoe, Y. In *Magnetism in clusters of non-magnetic elements: Pd, Rh, and Ru - Magnetism in clusters of non-magnetic elements*, 2003; Springer-Verlag: 2003; pp 81-84.

5. Nawate, M.; Nishimura, N.; Honda, S.; Tanaka, H. In *Ab initio calculation for magnetism of Pd nanoparticles*, 2005; Ieee-Inst Electrical Electronics Engineers Inc: 2005; pp 3424-3427.

6. Taniyama, T.; Ohta, E.; Sato, T., Observation of 4d ferromagnetism in free-standing Pd fine particles. *Europhysics Letters* **1997,** 38, (3), 195-200.

7. Jeon, Y. T.; Lee, G. H., Magnetism of the *fcc* Rh and Pd nanoparticles. *Journal of Applied Physics* **2008,** 103, (9), 5.

8. Sampedro, B.; Crespo, P.; Hernando, A.; Litran, R.; Lopez, J. C. S.; Cartes, C. L.; Fernandez, A.; Ramirez, J.; Calbet, J. G.; Vallet, M., Ferromagnetism in fcc twinned 2.4 nm size Pd nanoparticles. *Physical Review Letters* **2003,** 91, (23), 4.

9. Shinohara, T.; Sato, T.; Taniyama, T., Surface ferromagnetism of Pd fine particles. *Physical Review Letters* **2003,** 91, (19), 4.

10. Delin, A.; Tosatti, E.; Weht, R., Magnetism in atomic-size palladium contacts and nanowires. *Physical Review Letters* **2004,** 92, (5), 4.

11. Reddy, B. V.; Khanna, S. N.; Dunlap, B. I., GIANT MAGNETIC-MOMENTS IN 4D CLUSTERS. *Physical Review Letters* **1993,** 70, (21), 3323-3326.

12. Piveteau, B.; Desjonqueres, M. C.; Oles, A. M.; Spanjaard, D., Magnetic properties of 4d transition-metal clusters. *Physical Review B* **1996,** 53, (14), 9251-9266.

13. Hellwig, O.; Berger, A.; Fullerton, E. E., Domain walls in antiferromagnetically coupled multilayer films. *Physical Review Letters* **2003,** 91, (19), 4.

14. Fernandez, A.; Sampedro, B.; Litran, R.; Rojas, T. C.; Sanchez-Lopez, J. C.; Fernandez, A., Room temperature permanent magnetism in thiol-capped Pd-rich nanoparticles. *Nanotechnology* **2006,** 17, (5), 1449-1453.

15. Wang, W. C.; Kong, Y.; He, X.; Liu, B. X., Observation of magnetism in the nanoscale amorphous ruthenium clusters prepared by ion beam mixing. *Applied Physics Letters* **2006,** 89, (26), 3.

16. Clemente-Leon, M.; Coronado, E.; Soriano-Portillo, A.; Galvez, N.; Dominguez-Vera, J. M., Permanent magnetism in apoferritin-encapsulated Pd nanoparticles. *Journal of Materials Chemistry* **2007,** 17, (1), 49-51.

17. Niklasson, A. M. N.; Mirbt, S.; Skriver, H. L.; Johansson, B., Quantum-well-induced ferromagnetism in thin films. *Physical Review B* **1997,** 56, (6), 3276-3280.

18. Bouarab, S.; Demangeat, C.; Mokrani, A.; Dreysse, H., ONSET OF MAGNETISM IN PALLADIUM SLABS. *Physics Letters A* **1990,** 151, (1-2), 103-105.

19. Jain, T. K.; Moralles, M. A.; Sahoo, S. K.; Lesllie-Pellecky, D. L.; Labhasetwar, V., Iron oxide nanoparticles for sustained delivery of anticancer agents. *Molecular Pharmaceutics* **2005,** 2, (3), 194-205.

20. Whitney, T. M.; Jiang, J. S.; Searon, P. C.; Chien, C. L., *Science* **1993,** 261, 1316.

21. Sellmyer, D. J.; Zheng, M.; Skomski, R., Magnetism of Fe, Co and Ni nanowires in self-assembled arrays. *Journal of Physics-Condensed Matter* **2001,** 13, (25), R433-R460.

22. Guirado-Lopez, R.; Spanjaard, D.; Desjonqueres, M. C.; Aguilera-Granja, F., Electronic and geometrical effects on the magnetism of small Ru-N clusters. *Journal of Magnetism and Magnetic Materials* **1998,** 186, (1-2), 214-222.

23. Guirado-Lopez, R.; Spanjaard, D.; Desjonqueres, M. C., Magnetic-nonmagnetic transition in fcc 4d-transition-metal clusters. *Physical Review B* **1998,** 57, (11), 6305-6308.

24. Fernandez, A.; Sampedro, B.; Litran, R.; Rojas, T. C.; Sanchez-Lopez, J. C., Room temperature permanent magnetism in thiol-capped Pd-rich nanoparticles. *Nanotechnology* **2006,** 17, (5), 1449-1453.

25. Litran, R.; Sampedro, B.; Rojas, T. C.; Multigner, M.; Sanchez-Lopez, J. C.; Crespo, P.; Lopez-Cartes, C.; Garcia, M. A.; Hernando, A.; Fernandez, A., Magnetic and microstructural analysis of palladium nanoparticles with different capping systems. *Physical Review B* **2006,** 73, (5), 7.

26. Tartaj, P., Nanomagnets-from fundamental physics to biomedicine. *Current Nanoscience* **2006,** 2, (1), 43-53.

CHAPTER VI

IMPROVING INTERACTIONS BETWEEN METALLIC NANOWIRES AND BIOLOGICAL CELLS

1. Introduction

Nanomaterials often serve as media or vehicles for delivery, or as sensors for disease diagnosis[1]. The development of ligand-conjugated nanomaterials enables binding of various molecules at nanoparticle surfaces for improved interactions with biological entities. Cell surfaces are covered with carbohydrates, many of which are in the form of glycans. Carbohydrate-carbohydrate interactions between biological entities are important and are involved in processes like cell recognition, cell propagation, etc. For instance, the cellulose microfibriles where H-bonds crosslink and stabilize individual polyglucose chains with one another[2]. Researchers have utilized carbohydrate-carbohydrate interactions to provide adhesion forces and specificity for cell sorting and positioning[3-5]. In addition, Bertozzi's group has shown that synthesized glycans can be conjugated to nanomaterials to provide biocompatibility[3]. The altered terminal structures of carbohydrates are often associated with malignancy of cells[6]. Cancer related epitopes (determinates in terminal glycan) tend to be overexpressed in tumor cells. Tetrasaccharide Lewis Y is one of the most commonly found epitopes on transformed cells, and it has been observed in prostate tumor cells[7-9]. Because cancer glycans differ from those on their healthy counterparts, it may be possible to develop a system to target cancer cells based on exclusive binding to altered glycans.

In the process of cell-cell recognition, the cells can recognize their own kind and aggregate. Studies have shown that live cells bound to glycan-coated beads further reveal that glycan-glycan interactions have strong adhesion forces[10]. This provides an opportunity of employing the same glycan as receptor to specifically target the altered glycan that is over-expressed on the malignant cell surface.

Polyvalent interactions are prevalent and ubiquitous in biology and are involved in interactions between cells, proteins, DNA etc[11]. These interactions are characterized by the simultaneous binding of multiple ligands on one biological entity (a molecule, a surface) to multiple receptors on another. Viral infection, growth, differentiation, clearance, death, transportation, and migration occur via the attachments of virus to cells, bacterium to cells, cells to cells, and cells to antibodies through polyvalent interactions between ligands and receptors. One example is the influenza virus which attaches to the surface of a cell by interactions between the trimer of hemagglutin subunits and multiple moieties of sialic acid.

Polyvalent interactions are advantageous and collectively are much stronger than their corresponding monovalent interactions. In comparison to monovalent interactions, polyvalent interactions have increased free energy and stronger binding constants[10, 12]. Carbohydrate – carbohydrate (glycan - glycan) interactions are electrostatic in nature. However, the abundance of glycans on the cell surface and the large amount of corresponding glycans that could attached to a single nanostructure provide multivalent binding which could greatly increase the strength of the interactions and improve specificity.

There have been intensive studies on nanomaterials with magnetic properties for biological and medicinal applications[13-17]. As media of data storage, contrast agents for magnetic resonance imaging (MRI)[18], colloidal mediators for cancer magnetic hyperthermia[13, 19-23], active constituents for drug-delivery platforms[15, 24, 25] etc. magnetic nanomaterials exhibit unusual behaviors due to their quantum confinement, dielectric confinement, superparamagnetism. For instance, magnetic media bound to chemotherapeutic agents facilitate targeting on the malignant cells, tissues, or organs, as Jurgons[26] reported in his study of drug loaded iron oxide nanoparticles for cancer therapy.

Compared to magnetic nanoparticles which have found widespread use in biological applications, magnetic nanowires are much less advanced. The advantages over the use of nanowires instead of nanoparticles are related to the favorable geometrical anisotropy. The high aspect ratio creates different dipole magnetic moments in two directions with much larger permanent magnetic moment in the direction of the axis. Another reason that nanowires are good candidates for biological applications is their comparable length to cells, which is about a few microns. Their diameters can vary from 10 to 200 nm, which is comparable to the size of sub-cellular organisms. Ni nanowires have been of great interest for modern biology and medicine because they are relatively easy to fabricate and they have strong ferromagnetic moments. For example, the Prina-Mello[27] and Reich[28-30] groups independently reported studies on cell separation and manipulation through Ni nanowires that were internalized by living cells. Ni nanowires or multiple component magnetic nanowires with size of one order of magnitude smaller than cells (~50 – ~250 nanometer) are promising therapeutic nanostructures that are specially designed as delivery vehicles. In this chapter we will discuss a strategy to selectively bind Ni nanowires to malignant cells.

2. Experimental Details

2.1 Fabrication and characterization of nanowires

Materials. Anodic aluminum oxide (AAO) membranes (Whatman) were purchased from VWR. $NiCl_2$, H_3BO_3, Ni wire, Lewis Y tetrasaccaride and 3-(4,5-Dimethylthiazol-2-yl)-2,5-diphenyltetrazolium bromide (MTT) were procured from Sigma Aldrich Company. All culture flasks used were purchased from Corning Corporation.

Synthesis of Ni nanowires. Ni Nanowires were fabricated using the electrochemical deposition method[31]. Anodic aluminum oxide (AAO) membranes were used as templates. The plating solution consisted of 0.2 M $NiCl_2$ and 0.5 M H_3BO_3. Electrodeposition within the pores of the matrix was preceded by sputter coating of one face of the template with a metal film and using this metal film as a cathode or anode for electroplating. A constant voltage of -1.5V (*vs.* Ni wire) and 1 hour deposition time was employed for making Ni nanowires. The membrane was dissolved in 6M NaOH solution for more than 20 minutes. Sonication expedited the dissolution of the membrane and led to better separation of nanowires. After dissolving the membranes the Ni nanowires were isolated by centrifugation. The Ni nanowires were re-suspended in water or ethanol for cleaning. The nanowires were then characterized by scanning electron microscopy (SEM) and energy dispersive X-ray spectroscopy (EDAX).

2.2 Prostate tumor cell culture and normal prostate cell culture

The cells used in this study were provided by Dr. Kenneth V. Honn at the

Wayne State University School of Medicine. Normal prostate cell line RWPE- 2 cells were cultured in Keratinocyte-serum free medium (GIBCO 10724) prepared with 1% antibiotic-antimycotic (Gibco, Invitrogen), 10% FBS (Fetal Bovine Serum), and 1% L-Glutamine. Malignant prostate cell line PC3M cells were cultured in RPMI (-L-Glutamine) medium (Roswell Park Memorial Institute medium, Gibco, Invitrogen, or HyClone) prepared with 1% antibiotic-antimycotic, 10% FBS, and 1% L-Glutamine. All cells were incubated at 37°C with 5% CO_2. Subculture was routinely performed at approximately 90% confluence. Subculture was prepared with a Versene (GIBCO, 15040) wash and trypsin EDTA. 25 cm^2 cell culture flasks and T35 cm^2 cell culture flasks were used for all the cell cultures.

All the cells were incubated for 48 h to reach 90% confluence before any experiments were carried out.

2.3 Cell viability test

MTT assay was performed to determine the survival of the prostate normal cells after they had been left to incubate in the presence of bare Ni nanowires. MTT solution was prepared by dissolving 5 mg/mL 3-(4,5-Dimethylthiazol-2-yl)-2,5-diphenyltetrazolium bromide in phosphate buffered saline (PBS). The fresh solution was stirred and stored at 4°C for 24 hours. The MTT solution was added to the cell media and incubated for 4 hours. Then 0.5 mL of isopropyl with 0.04 M HCl was added to the media. After 10 minutes, the spectrophotometer measurement was performed to record the absorbance readings.

Control samples were prepared that consisted of the cells alone incubated under the same conditions but without any nanowires present. The short-term toxic effects were observed by monitoring the cell proliferation rate of the samples both with and without nanowires. The density of the cell populations was measured over the course of 7 days on a daily basis.

2.4 Saccharide conjugated Ni nanowires

Ni nanowires suspended in methanol solution were sonicated 10 times (50 seconds each time at 20 kHz) in order to separate the nanowires. After sonication, the nanowires were sterilized by washing with ethanol. Furthermore, the nanowires were washed with DPBS (Dulbecco's Phosphate Buffered Saline, GIBCO, 14190) and then resuspended in RPMI media. About 1 mg Lewis Y tetrasaccaride was added to the Ni nanowire culture media suspension. The mixture was spun overnight using an overhead stirrer. The stirrer consisted of a plastic rod rather than a magnetic stirrer since the Ni nanowires themselves are magnetic.

2.5 Interaction of Lewis Y tetrasaccharide conjugated Ni nanowires with normal or malignant prostate cells

The tetrasaccharide conjugated nanowires were added to media solution that contained RWPE- 2 normal prostate cells or PC3M malignant prostate cells for attachment tests. The mixture was incubated for 24 h before imaging using an optical microscope. Most pictures were taken in Nikon DIAPHOT 200 microscope with magnification of 20 or 40. The results were compared to controlled samples, where the bare Ni nanowires were introduced to the normal or malignant prostate cells.

3. Results

3.1 Fabrications and characterization of Ni nanowires

Nickel nanowires were successfully prepared using the electrochemical deposition method. The SEM images (Figure 6.1) show the fabricated Ni nanowires. The diameter of the Ni nanowires was 200 nm and the length was 10 μm. The electrodeposition method allows control of the length of the nanowires by adjusting the deposition time. Following the electrodeposition step, the Ni nanowires are released from the template but rather than being free standing nanowires, they tend to form bundles that easily precipitate in aqueous solution. One method to break up the bundles is by sonication of the sample. Thereafter, ligands could be used to functionalize the surface or as barriers to separate the nanowires. EDAX analysis (Figure 5.2) of the Ni nanowires showed an O:Ni ratio of 3:10 on the surface, indicating that the nickel atoms on surface of the Ni nanowires were oxidized. This oxide layer was a few nanometers thick.

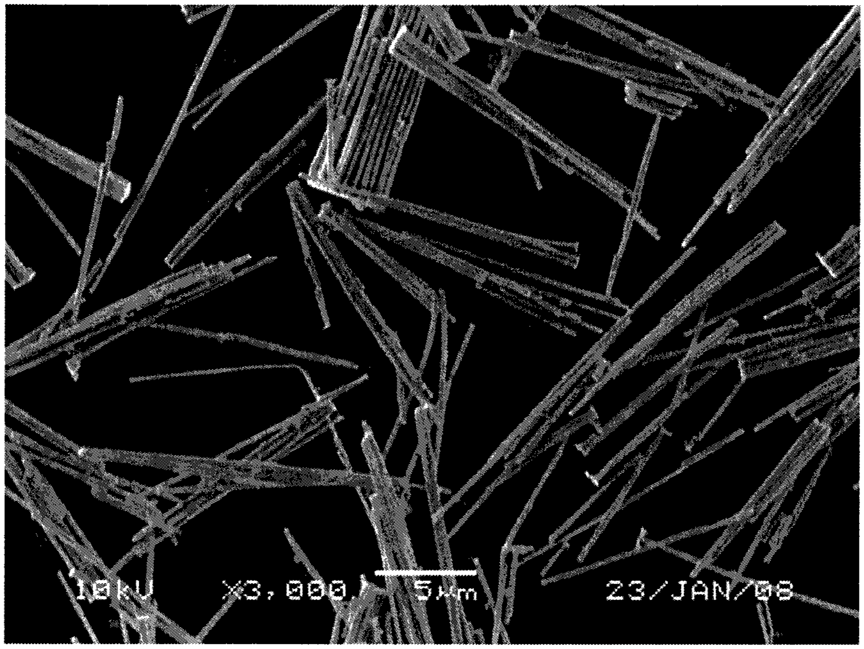

Figure 6.1 SEM images of Ni nanowires. The nanowires are 200 nm in diameter and 10 μm in length.

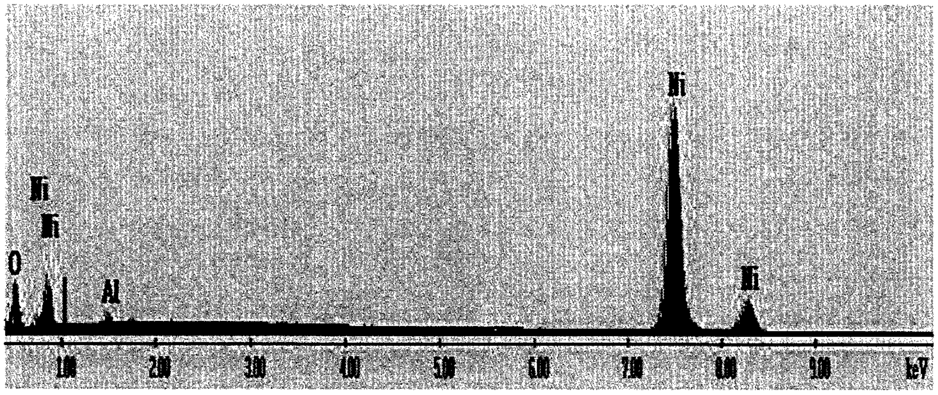

Figure 6.2 Elemental EDAX analyses of nickel nanowires. The peaks are labeled with the emission line of the corresponding element.

3.2 Viability of prostate normal cells in the present of nanowires

The increased interest in using nanoscale materials for biological applications necessitates the need to investigate the cytotoxicity of these materials. Yang[32] demonstrated that silicon nanowires penetrated tumor cells but did not cause cell death after several days. Literature reports have demonstrated that Au nanostructures do not cause cytotoxicity to human cells or stop cell proliferation[33, 34]. Magnetic Ni nanowires have been demonstrated to be non-harmful to cells[27, 35]. Related studies have assessed the toxicity of metal nanomaterials at low levels. In addition, when these studies are carried out any ligand at the surface of the nanomaterial should also be tested as it may be responsible for the overall toxicity[36]. Lewis Y tetrasaccharide which is a glycan is not expected to be toxic to most cells in moderate concentrations. Furthermore, the attachment of Lewis Y tetrasaccharide on the Ni nanowire surface enhances biocompatibility with the cells. The cytotoxicity of nickel discussed in previous studies[27, 30] has showed that cells survived up to 5 days with a survival rate of 95% after internalizing the Ni nanowires. We assessed the cytotoxicity of Ni nanowires on RWPE-2 normal prostate cells by testing cell viability using an MTT assay. The assay was performed to compare the amount of proliferating cells in a sample with and without nanowires. Living cells metabolized MTT inducing the color change from yellow to purple. The depth of the purple color (absorption in photometer) is in direct proportion to the amount of living cells in the solution. Figure 6.3 displays a comparative image of 24 wells containing controlled samples (normal cells only) and tested samples (nanowires included). There was no obvious difference in depth of the purple color between controlled samples and tested samples. Nearly

100% survival rate within seven days (Figure 6.4) of normal cells was observed after Ni nanowires were introduced. These results show that with nanowires in the media, the cells were able to continue growing through cell division at the same rate as cells without nanowires in their culture. The high viability suggests that the nanowires do not affect cell function at these time scales.

3.3 Interaction between bare Ni nanowires and normal or malignant prostate cells

The nanowires have high aspect ratio and are sufficiently rigid to be mechanically manipulated. For instance, the diameters of nanowires (1-200 nm) are few orders smaller than the size of biological cells (in the order of 10 μm). Magnetism facilitates the control of nanowires by applying forces. Reich et al oriented the internalized nickel nanowires to achieve cell separation and manipulation[28, 30]. However, they did not study the selectivity of nanowire to specific cells which requires specific receptors to differentiate the targeting cells from others.

Bare Ni nanowires (unfunctionalized) were suspended in media that contained normal prostate cells RWPE-2 or cancerous prostate cells PC3M. In both solutions, the nanowires did not display any specific binding or any notable interaction with cells after 24 hours of exposure (Figure 6.5). The images display random positioning of the nanowires relative to both types of cells.

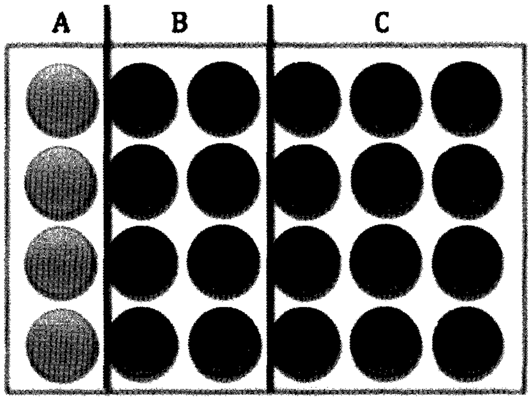

Figure 6.3 MTT assay on RWPE-2 normal prostate cells. Column A contained appropriate media. Column B contained cell culture in media. Column C contained cell culture in media containing nanowires.

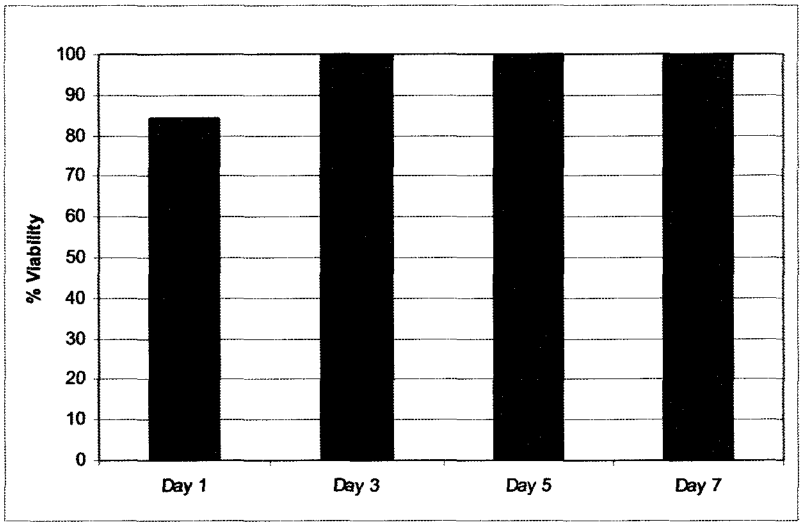

Figure 6.4 Survival rate of RWPE-2 normal prostate cells after Ni nanowires were introduced to the media

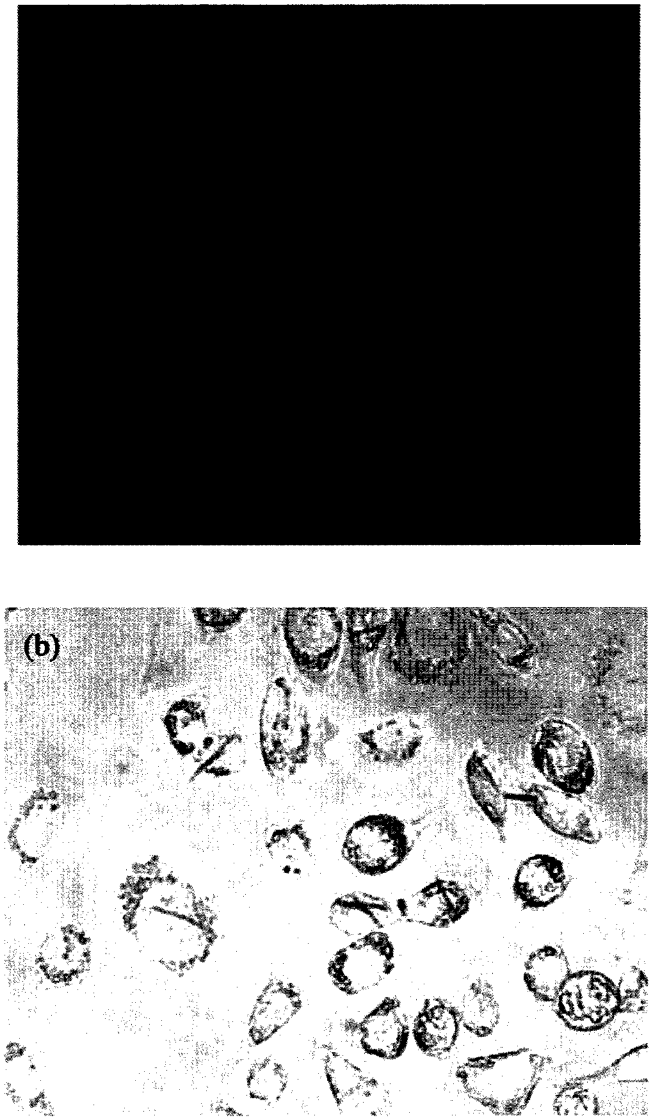

Figure 6.5 (a) RWPE-2 normal prostate cells, and (b) PC3M prostate cancer cells exposed to Ni nanowires.

3.4 Selectivity of surface functionalized nanowire on prostate cancer cells

Nickel nanowires putatively functionalized with Lewis Y glycans were incubated with PC3M and RPWE-2 cell lines. The RPWE-2 was shown to have similar results as when RPWE-2 was incubated with bare Ni nanowires (Figure 6.6a), the cells and nanowires were isolated from each other. However, in PC3M cell solution, it showed that nearly all surface functionalized nanowires were attached to the cells in ways either on the surface or were internalized by the cells (Figure 6.6b).

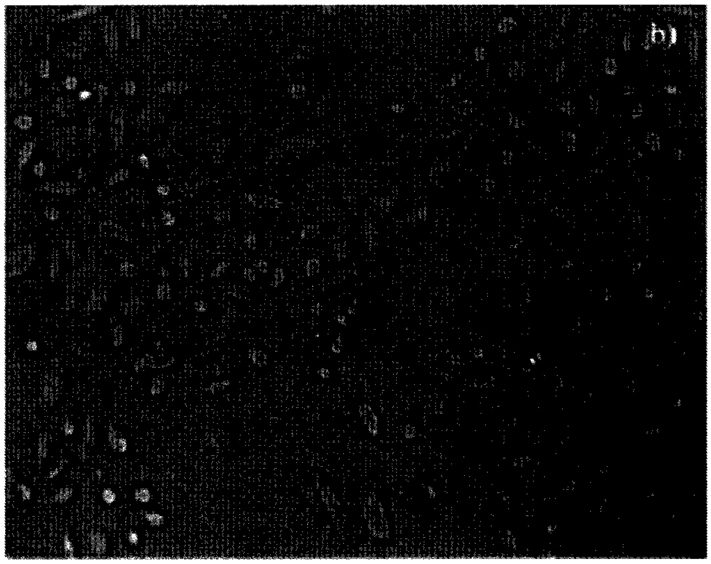

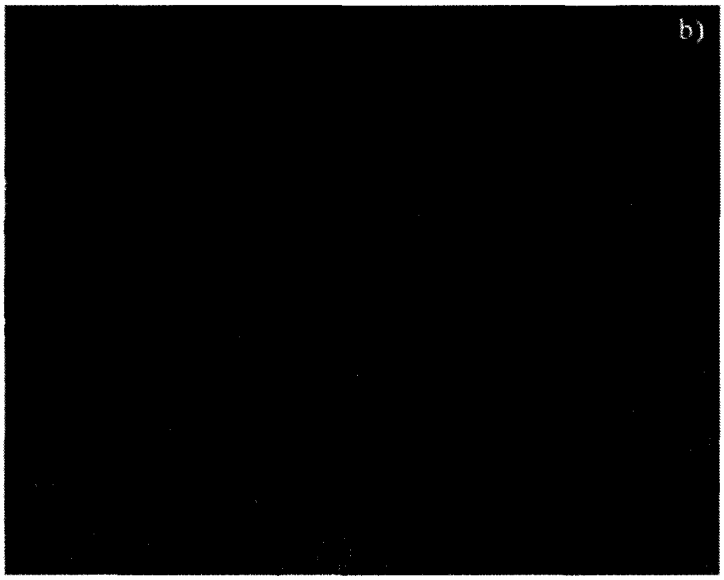

Figure 6.6 Ni nanowires were functionalized with a saccharide and allowed to interact with (a) normal prostate cells RWPE-2 and (b) prostate cancer cells PC3M.

The graph in Figure 6.7 shows the overall results of the interactions between Ni nanowires with either normal prostate cells or prostate cancer cells. Bare nanowires show low specificity to both normal cells and cancer cells. However the Lewis Y tetrasaccharide functionalized nanowires had high selectivity toward the cancer cells relative to the normal cells. By applying external magnetic force, the cancer cell could be separated from normal cell.

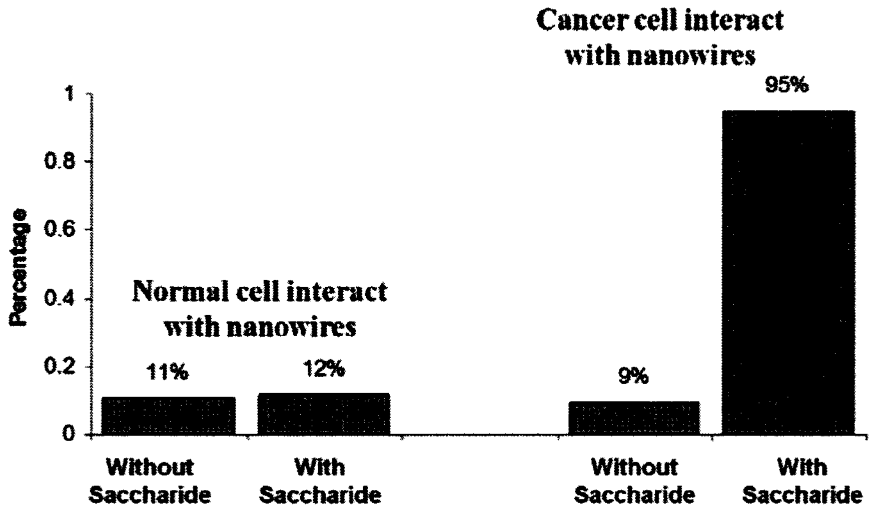

Figure 6.7 Selectivity of Lewis Y tetrasaccharide functionalized Ni nanowires

4. Discussion

Bioconjugation has become an important field as it allows an understanding of how to best link functional nanomaterials with biological cells. The use of Lewis Y tetrasaccharide or other glycans has several potential advantages over other targeting molecules such as antibodies, DNA, or peptides for their small size. The hydroxide groups on the glygan can easily bind to metal oxide surfaces, and bind to cells through carbohydrate-carbohydrate interaction. The nanowires serve as substrates for multi-valent interaction.

When nanowires were functionalized with Lewis Y tetrasaccharide, there was reduced affinity of the nanowires to normal cells, but almost all the tumor cells were bound to the nanowires. Therefore from the results of this work we can conclude that we have successfully achieved a way to target prostate cancer cells using magnetic nickel nanowires functionalized with the altered glygans.

5. Summary

The recognition of cancer cells depends on the specificity of the agents that are bound on the nanomaterials. This investigation is crucial toward developing a fundamental level of understanding of the effects of nanomaterials on biological entities. Lewis Y tetrasaccharide is an altered determinant of glycans that are typically over-expressed on prostate cancer cell surfaces. The attraction between the same kinds of glycans makes it possible for using Lewis Y tetrasaccharide as a ligand to target receptors on the cancer cell surface. The most important observation is that its functionalization on the nickel nanowire surface did not alter or affect its binding to the normal cells.

6. References

1. Siwy, Z.; Trofin, L.; Kohli, P.; Baker, L. A.; Trautmann, C.; Martin, C. R., Protein biosensors based on biofunctionalized conical gold nanotubes. *Journal of the American Chemical Society* **2005,** 127, (14), 5000-5001.

2. Prescher, J. A.; Bertozzi, C. R., Chemistry in living systems. *Nature Chemical Biology* **2005,** 1, (1), 13-21.

3. Chen, X.; Wu, P.; Rousseas, M.; Okawa, D.; Gartner, Z.; Zettl, A.; Bertozzi, C. R., Boron Nitride Nanotubes Are Noncytotoxic and Can Be Functionalized for Interaction with Proteins and Cells. *Journal of the American Chemical Society* **2009,** 131, (3), 890.

4. Chen, X.; Tam, U. C.; Czlapinski, J. L.; Lee, G. S.; Rabuka, D.; Zettl, A.; Bertozzi, C. R., Interfacing carbon nanotubes with living cells. *Journal of the American Chemical Society* **2006,** 128, (19), 6292-6293.

5. Chen, X.; Lee, G. S.; Zettl, A.; Bertozzi, C. R., Biomimetic engineering of carbon nanotubes by using cell surface mucin mimics. *Angewandte Chemie-International Edition* **2004,** 43, (45), 6111-6116.

6. Dube, D. H.; Bertozzi, C. R., Glycans in cancer and inflammation. Potential for therapeutics and diagnostics. *Nature Reviews Drug Discovery* **2005,** 4, (6), 477-488.

7. Orntoft, T. F.; Vestergaard, E. M., Clinical aspects of altered glycosylation of glycoproteins in cancer. *Electrophoresis* **1999,** 20, (2), 362-371.

8. Zhang, S. L.; CordonCardo, C.; Zhang, H. S.; Reuter, V. E.; Adluri, S.; Hamilton, W. B.; Lloyd, K. O.; Livingston, P. O., Selection of tumor antigens as targets for immune attack using immunohistochemistry .1. Focus on gangliosides. *International Journal of Cancer* **1997,** 73, (1), 42-49.

9. Zhang, S. L.; Zhang, H. S.; CordonCardo, C.; Reuter, V. E.; Singhal, A. K.; Lloyd, K. O.; Livingston, P. O., Selection of tumor antigens as targets for immune attack using immunohistochemistry .2. Blood group-related antigens. *International Journal of Cancer* **1997,** 73, (1), 50-56.

10. Bucior, I.; Scheuring, S.; Engel, A.; Burger, M. M., Carbohydrate-carbohydrate interaction provides adhesion force and specificity for cellular recognition. *Journal of Cell Biology* **2004,** 165, (4), 529-537.

11. Mammen, M.; Choi, S. K.; Whitesides, G. M., Polyvalent interactions in biological systems: Implications for design and use of multivalent ligands and inhibitors. *Angewandte Chemie-International Edition* **1998,** 37, (20), 2755-2794.

12. Rojo, J.; Morales, J. C.; Penades, S., Carbohydrate-carbohydrate interactions in biological and model systems. In *Host-Guest Chemistry*, Springer-Verlag Berlin: Berlin, 2002; Vol. 218, pp 45-92.

13. Berry, C. C.; Curtis, A. S. G., Functionalisation of magnetic nanoparticles for applications in biomedicine. *Journal of Physics D-Applied Physics* **2003,** 36, (13), R198-R206.

14. O'Grady, K., Progress in applications of magnetic nanoparticles in biomedicine. *Journal of Physics D-Applied Physics* **2009,** 42, (22), 1.

15. Pankhurst, Q. A.; Connolly, J.; Jones, S. K.; Dobson, J., Applications of magnetic nanoparticles in biomedicine. *Journal of Physics D-Applied Physics* **2003,** 36, (13), R167-R181.

16. Tartaj, P.; Morales, M. D.; Veintemillas-Verdaguer, S.; Gonzalez-Carreno, T.; Serna, C. J., The preparation of magnetic nanoparticles for applications in biomedicine. *Journal of Physics D-Applied Physics* **2003,** 36, (13), R182-R197.

17. Tartaj, P.; Morales, M. P.; Gonzalez-Carreno, T.; Veintemillas-Verdaguer, S.; Serna, C. J., Advances in magnetic nanoparticles for biotechnology applications. *Journal of Magnetism and Magnetic Materials* **2005,** 290, 28-34.

18. Bulte, J. W. M., Magnetic nanoparticles as markers for cellular MR imaging. *Journal of Magnetism and Magnetic Materials* **2005,** 289, 423-427.

19. Kalambur, V. S.; Han, B.; Hammer, B. E.; Shield, T. W.; Bischof, J. C., In vitro characterization of movement, heating and visualization of magnetic nanoparticles for biomedical applications. *Nanotechnology* **2005,** 16, (8), 1221-1233.

20. Dutz, S.; Hergt, R.; Murbe, J.; Topfer, J.; Muller, R.; Zeisberger, M.; Andra, W.; Bellemann, M. E., Magnetic nanoparticles for biomedical heating

applications. *Zeitschrift Fur Physikalische Chemie-International Journal of Research in Physical Chemistry & Chemical Physics* **2006,** 220, (2), 145-151.

21. Jain, T. K.; Moralles, M. A.; Sahoo, S. K.; Lesllie-Pellecky, D. L.; Labhasetwar, V., Iron oxide nanoparticles for sustained delivery of anticancer agents. *Molecular Pharmaceutics* **2005,** 2, (3), 194-205.

22. Mornet, S.; Vasseur, S.; Grasset, F.; Duguet, E., Magnetic nanoparticle design for medical diagnosis and therapy. *Journal of Materials Chemistry* **2004,** 14, (14), 2161-2175.

23. Hergt, R.; Andra, W.; d'Ambly, C. G.; Hilger, I.; Kaiser, W. A.; Richter, U.; Schmidt, H. G., Physical limits of hyperthermia using magnetite fine particles. *Ieee Transactions on Magnetics* **1998,** 34, (5), 3745-3754.

24. Lubbe, A. S.; Alexiou, C.; Bergemann, C., Clinical applications of magnetic drug targeting. *Journal of Surgical Research* **2001,** 95, (2), 200-206.

25. Lubbe, A. S.; Bergemann, C.; Brock, J.; McClure, D. G. In *Physiological aspects in magnetic drug-targeting*, 1999; Elsevier Science Bv: 1999; pp 149-155.

26. Jurgons, R.; Seliger, C.; Hilpert, A.; Trahms, L.; Odenbach, S.; Alexiou, C., Drug loaded magnetic nanoparticles for cancer therapy. *Journal of Physics-Condensed Matter* **2006,** 18, (38), S2893-S2902.

27. Prina-Mello, A.; Diao, Z.; Coey, J. M. D., Internalization of ferromagnetic nanowires by different living cells. *Journal of Nanobiotechnology* **2006,** 4, (9).

28. Hultgren, A.; Tanase, M.; Felton, E. J.; Bhadriraju, K.; Salem, A. K.; Chen, C. S.; Reich, D. H., Optimization of yield in magnetic cell separations using nickel nanowires of different lengths. *Biotechnology Progress* **2005,** 21, (2), 509-515.

29. Tanase, M.; Felton, E. J.; Gray, D. S.; Hultgren, A.; Chen, C. S.; Reich, D. H., Assembly of multicellular constructs and microarrays of cells using magnetic nanowires. *Lab on a Chip* **2005,** 5, (6), 598-605.

30. Hultgren, A.; Tanase, M.; Chen, C. S.; Meyer, G. J.; Reich, D. H., Cell manipulation using magnetic nanowires. *Journal of Applied Physics* **2003,** 93, (10), 7554-7556.

31. Wirtz, M.; Martin, C. R., Template-fabricated gold nanowires and nanotubes. *Advanced Materials* **2003,** 15, (5), 455-458.

32. Kim, W.; Ng, J. K.; Kunitake, M. E.; Conklin, B. R.; Yang, P. D., Interfacing silicon nanowires with mammalian cells. *Journal of the American Chemical Society* **2007,** 129, (23), 7228.

33. Connor, E. E.; Mwamuka, J.; Gole, A.; Murphy, C. J.; Wyatt, M. D., Gold nanoparticles are taken up by human cells but do not cause acute cytotoxicity. *Small* **2005,** 1, (3), 325-327.

34. Chen, Y. S.; Hung, Y. C.; Liau, I.; Huang, G. S., Assessment of the In Vivo Toxicity of Gold Nanoparticles. *Nanoscale Research Letters* **2009,** 4, (8), 858-864.

35. Hultgren, A.; Tanase, M.; Chen, C. S.; Reich, D. H. In *High-yield cell separations using magnetic nanowires*, 2004; Ieee-Inst Electrical Electronics Engineers Inc: 2004; pp 2988-2990.

36. Wang, S. G.; Lu, W. T.; Tovmachenko, O.; Rai, U. S.; Yu, H. T.; Ray, P. C., Challenge in understanding size and shape dependent toxicity of gold nanomaterials in human skin keratinocytes. *Chemical Physics Letters* **2008,** 463, (1-3), 145-149.